Single Cell Decisions in Endothelial Population in the Context of Inflammatory Angiogenesis

by

Tharathorn Rimchala

Submitted to the Department of Biological Engineering
in partial fulfillment of the requirements for the degree of

Doctor of Philosophy in Biological Engineering

at the

MASSACHUSETTS INSTITUTE OF TECHNOLOGY

February 2012

Author .....
Department of Biological Engineering
January 9, 2012

Certified by .....
Douglas A. Lauffenburger
Ford Professor of Bioengineering
Thesis Supervisor

Accepted by .....
Forest M. White
Chairman, Course XX Graduate Program Committee

This thesis is examined by the following Thesis Committee:

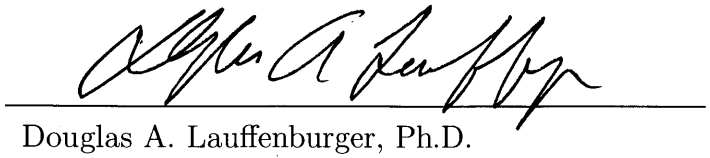

Douglas A. Lauffenburger, Ph.D.
Ford Professor of Biological Engineering,
Chemical Engineering and Biology
Massachusetts Institute of Technology

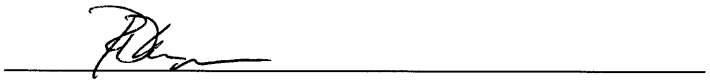

Roger D. Kamm, Ph.D.
Singapore Research Professor of Biological
and Mechanical Engineering
Massachusetts Institute of Technology

Matthew A. Nugent, Ph.D.
Professor, Biomedical Engineering, Biochemistry
and, Ophthalmology,
Boston University, School of Medicine

Single Cell Decisions in Endothelial Population in the Context of Inflammatory Angiogenesis

by

Tharathorn Rimchala

Submitted to the Department of Biological Engineering
on January 9, 2012, in partial fulfillment of the
requirements for the degree of
Doctor of Philosophy in Biological Engineering

Abstract

Normalizing angiogenesis is a promising strategy for treatments of cancer and several disorders plaqued by misregulated blood supplies. To address the daunting complexity of angiogenesis arising from multiple phenotypic behaviors governed by multiple stimuli, computational approaches have been developed to predict sprouting angiogenic outcomes. In recent years, the agent based model, in which individual cells are modeled as autonomous decision making entities, has become an important tool for simulating complex phenomena including angiogenesis. The reliability of these models depends on model validation by quantitative experimental characterization of the cellular (agent) behaviors which so far has been lacking.

To this end, I develop an experimental and computational method to semi-automatically estimate parameters describing the single-cell decision in the agent based model based on flow cytometry aggregate headcount data and single cell microscopy which yields full panel single cell trajectories of individual endothelial cells. Applying thees method to the single cell decision data, I propose two conceptual models to account for the different state transition patterns and how they are modulated in the presence of opposing inflammatory cytokines. The observed unique state transition patterns in the angiogenic endothelial cell population are consistent with one of these descriptions, the diverse population model (DPM). The DPM interpretation offers an alternative view from the traditional paradigm of cell population heterogeneity. This understanding is important in designing appropriate therapeutic agents that take effect at the cellular level to meet a tissue level therapeutic goal.

Thesis Supervisor: Douglas A. Lauffenburger
Title: Ford Professor of Bioengineering

Acknowledgments

This thesis project would not have been possible without the support of many people. First and foremost, I would like to express my deeptest gratitude to my advisors Professor Douglas Lauffenburger and Professor Roger Kamm for their tireless support and consistent encouragement throughout my PhD. Doug has been an inspiration and a role model for me scientifically since I joined the Biological Engineering Department. Doug is not only an exceptional and visionary scientist, leading our group to be able to excel in both modeling and experimental realms, but also an extremely caring advisor. Roger contributes significantly to my wonderful experience at MIT. Roger gives me exceptional level of independence in exploring my thesis topic and conducting experiments, while at the same time provides specific guidance when needed. Roger's effort in creating a collaborative research program enables me to expand my research expertise by learning from members of collaborating labs. Having both Doug and Roger as advisors is a privilege and I cannot justly express my appreciation for their support and all they have done.

I also would like to acknowledge Professor Matthew Nugent for serving as an important addition to my thesis committee. Matt brings in an expertise in biochemistry of extracellular matrix that proves crucial in understanding the physiological context of my thesis work. In addition, I would like to thank Professor Scott Manalis and Professor Jong-yoon Han for the opportunity to serve as a teaching assistant in their class.

Every person who has achieved his or her dreams in certain area of his or her life has at least one mentor. An endeavor like a PhD cannot be accomplished without one. For me, my research project would have not gotten off the ground without the attentive mentorship of Professor Seok (Sid) Chung and Professor Ryo Sudo who were post doctoral scholars in the Kamm lab during my first few years in the Kamm. Sid, the microfluidic expert in the lab, taught me all the experimental tricks on device fabrication from the very beginning. Ryo, the tissue engineering expert with magical

hands, walked me through how to keep the cells *'happy and healthy'* in the lab. To this day, Sid and Ryo still work closely as a team and together they become my role model of a true collaboration. On the Lauffenburger lab side, I have been fortunate to know and befriend Dr. Shannon Alford. Shannon greatly enriched my knowledge and experience at MIT with her exceptional insights into molecular and cell biology experiments, her mentorship, and friendship.

In addition to having great advisors and mentors, I am fortunate to be part of the a collaborative emerging frontiers in research initiative (EFRI) project; and this is perhaps the most unique aspect of my experience at MIT. Those days in the Kamm lab conference room we were frustrating trying to better-define the projects and tasks and those evenings we spent putting together EFRI reports and presentations will be remembered. To this I would like to acknowledge all of the EFRI team members including Anusuya Das, Ta Hang, Waleed Farahat, Alisha Schor, Levi Wood, Ioannis Zervantonakis.

All of the past and current members of the Lauffenburger, the Kamm lab, the EFRI grant and the CDP center have been my teachers, collaborators and friends. Through their kind help, encouragement, and advice both inside and outside of the labs, they have all contributed to the completion of this thesis. Hyung-Do Kim introduced me to the Lauffenburger lab, taught me his cell migration experiments and checked in on me to make sure I did not sleep in the lab. Ulrike Phillipar and Michael Balsalmo taught me how to do molecular biology experiments. Shannon Alford, Juliana Chan Drum, Levi Wood, Hyung-suk Lee, Tae Yoon Kim, and Pat Sampattavanich provided great advice regarding opportunities for the next stage of my scientific career. Ta Hang, Shannon Alford, Yannis Zervantonakis, Bill Polacheck, Sebastian Uzel, Cherry Wan, Nathan Hammond have all given me valuable feedback on my experimental designs and procedures and have been willing to participate in extensive discussion with my work. I am also deeply indebted to my past and present office-mates, including Cherry Wan, Tae Yoon Kim, Jessie Jeon, Bill Hess, and Pro-

fessor Kenichi Funamoto who have helped navigate the everyday happening in life and research. I am also grateful to Cherry Wan, Ran Li and Jordan Whisler whose vigilance helps shape the organization of the lab; and to Vivek Sivathanu and Bill Polacheck who make sure that we never run out of lab supplies. Lastly, I would like to thank Le Thanh Tu Nguyen for sharing much fun time doing *experiments-we've-never-done* in the lab.

I have also been fortunate to receive extensive scientific supports from other labs and centers at MIT. Glenn Paradis of the Koch Institute, Erika Noonan of the Samsan lab, and Gerald Ostheimer of the Yaffe lab were incredibly generous at sharing reagents and helping me design my first flow cytometry experiment. Anna Bershtyn of the Irvine lab walked me through the use of the Irvine lab's line scanning microscope and were incredibly flexible and approachable when I have problem with imaging. Aprotim Muzumdar of the Bathe lab was incredible kind and generous with time to help me with the Cellomics microscope. An integral part of making my graduate research possible are the multiple fellowships and grants that were used to support my research assistantship. I would like to thank Dr. Andrew J. Viterbi and the Viterbi Family Foundation, the Merck-MIT CSBi fellowship, the National Science Foundation, and the Cell Decision Consortium at MIT for their generous support.

During my time at MIT, I have forged some true friendships that support me throughout my PhD. Apart from those I already mentioned, I have shared memorable moments with Alice Lo, Miaoqing Fang, Yuri Matsumoto, Akila Jayaraman, Andrew Koo, Adrienne Li, Lily Jeng, Trina Kok, Jing Wang, Dirk Neumann, and Mint Wongviriyawong; and to this I would like to thank them for making my time at MIT much more than about research.

I would like to express my appreciation to the special people in my life who make me believe in what I do. First and foremost, I would like to thank Arthur Lue for standing beside me for the last three years of my PhD and throughout the process

of writing this thesis. Apart from being my only family in Cambridge, Arthur has been my motivation for continuing to improve my knowledge and moving my research career forward. This thesis would not have been completed as well as it does without his constructive criticism, constant encouragement, and unparallel patience. Most of all, I would like to thank my parents Prasert Rimchala and Vilaipan Rimchala for allowing me to follow my ambitions throughout my childhood and being supportive in every way they can.

Thank you.

Contents

List of Figures

Chapter 1

Introduction

Sprouting angiogenesis - formation of new branch from existing blood vessel - is a normal and vital process in growth, development, and tissue repair. It is however involves in tumor progression, supporting tumor growth beyond the diffusion-limited length scale and enabling progression beyond tissue/organ of origin and colonization of new sites in the body. From a perspective of endothelial cell behavior, angiogenesis has been described as a multi-cue, multi-response process. Initially a few endothelial cells lose contact with their neighbors, then acquire the ability to actively divide and to migrate into the surrounding tissue. While cells in an angiogenic population are exposed to different levels of various angiogenic factors, initiating diverse signalings and exhibiting responses, their proliferation, and survival must be coordinated to produce appropriate vascular structures [4, 42]. In the past decade, sprouting angiogenesis has become an important target for combating diseases characterized by insufficient blood supplies, or excessive/abnormal vascularization [21, 38, 85]. While the general understandings of angiogenesis at the tissue level has been established, the cellular and molecular understandings that will enable control of the process remain inadequate [22].

To address the daunting complexity of angiogenesis arising from multiple phenotypic behaviors governed by multiple stimuli, mathematical and computational approaches have been developed to predict sprouting angiogenic outcomes; an ex-

cellent review of the current state of these approach is discussed in [83]. In recent years, the agent based modeling approach, in which individual cells are modeled as autonomous decision making entities called agents, has become an important tool for simulating complex phenomena including angiogenesis. The reliability of these models depends on model validation by quantitative experimental characterization of the cellular (agent) behaviors which so far has been lacking. To address the model validation rigorously, I designed and implemented an experimental and computational method to quantify cellular behaviors and quantify the parameters describing the single-cell decision making by direct observations of individual angiogenic endothelial cells. In this thesis, I conceptualized an implemented an experimental and computational method to estimate the parameters describing single cell decision consistent with an agent-based model developed in the Kamm lab. By applying this method to study the cell decision in angiogenic population subjected to inflammatory cytokine stimulation, I observed interesting emerging patterns of single cell decision dynamics within the endothelial population that led me to purpose an alternative conceptual model of how angiogenic and angiostatic cytokines may modulate the tissue level responses by altering single cell decision dynamics.

The central premise of this thesis is that the complex cell behavior leading to sprouting is a consequence of cell-level decisions. Here, the decision making process is represented by the transitions among four key phenotypic behaviors involved in angiogenesis: proliferative, migratory, apoptosis, and sessile (i.e. non-proliferative, non-migratory, and non-apoptotic). In this work, I discovered from flow cytometry and live imaging experiments that the phenotypic state transitions are appropriately described by a continuous Markov chain (CTMC), a class of stochastic framework widely used in agent based approach. As such, we used CTMC formulation to estimate the single-cell decision parameter. Together these findings support the validity of the agent based modeling approach and offer quantitative parameters required for modeling cellular behavior in angiogenesis.

The contents of this thesis are arranged as followed. In the first chapter, I describe the importance of sprouting angiogenesis as therapeutic targets and briefly review evolution of experimental platforms for angiogenesis. Then I review the current state-of-the-art mathematical and computational approaches in the past decade to simulate and predict the tissue level outcomes of sprouting angiogenesis. Then I argue that for the current-state-of-the-art methodologies in angiogenesis modeling, the quantitative understanding of the single cell decision derived from experimentation is essential in generating reliable model predictions.

In the second chapter, I describe the experimental results that led me to purpose inflammatory angiogenesis as a physiological context in which to study the single cell decision. To this end, I explain the role of vascular endothelial growth factor and platelet factors as key relevant cytokines and describe the effect of these cytokines on the tissue level angiogenic responses on angiogenic endothelial cells.

In chapter three, I explain the rationale and expected outcome of studying single cell decision in sprouting angiogenesis. I described two types of experimentally obtainable single cell decision data: aggregate and full panel data sets. In this chapter, I present the derivation of the parameter inference formulation consistent with the aggregate data obtained by multi-parametric flow cytometry.

Chapter four describes the experimental design to obtain full panel data from live cell microscopy. In this chapter, I describe the parameter inference algorithms consistent with the full panel data. Then, I present the parameter estimation results of applying the parameter maximum likelihood estimatation to the full panel data of angiogenic endothelial cell population under the inflammatory cytokine treatment conditions. In addition to the parameter estimation, I describe the further step I took to show that within a presumably homogeneous population, angiogenic endothelial cells adopt a few unique transition patterns (clusters) distinguished by the dwell time in and the transition frequencies among the four phenotypic states. Based on this

finding, I purpose two conceptual models to account for the different state transition patterns and how they are modulated in the presence of the inflammatory cytokines PF4.

In this final chapter, I conclude the thesis and discuss the future perspectives of this thesis work. I specifically describe the framework for incorporating the experimentally obtained single cell transition dynamic parameter to agent based simulation of angiogenesis. With the additional end point dataset I used to estimate the sprouting (stalk-to-tip transition) probabilities under different cytokine conditions and the collaboration with Levi Wood for his sprout elongation model, we will use this approach to try to predict different sprout morphologies.

1.1 Angiogenesis as a therapeutic target

Blood vessel arose in evolution as a mechanism that allows the supply of nutrients, oxygen, and waste exchange in multi-cellular species and thus evolutionary survival of genes in such systems. In modern medicine, it is also utilized as a conduit through which physicians may obtain diagnosis and/or introduce therapeutic drugs to patient's internal organs. As a living tissue, blood vessel can be induced to overgrow, degenerate or become dysfunctional in many physiological conditions. The ability to modulate and normalize blood vessel morphology and vessel properties has enormous therapeutic appeal as it can be used to cure diseases characterized by inappropriately overgrown vessel such as in age-related macular degeneration, insufficient blood supply such as in diebetic wounds and coronary artery obstruction. The ability to control blood vessel growth can be also used to stop unwanted misregulated blood vessel growth such as in tumor angiogenesis.

Promises in controlling of angiogenesis to meet therapeutic goals have led to a spurt of research efforts in the recent decades to develop experimental and computational methods to study the angiogenesis process and series of clinical trials following

the efficacies of therapeutic strategies stemming from these research efforts. For most of these research initiatives, the main goal is to understand how angiogenesis process occurs especially in tumor context. In this section, I review the experimental and computational approaches to study angiogenic process. In the subsequent section, I will describe how the designs and implementation of my thesis work are drawn from the strengths of these efforts and how the findings from my thesis work add to understanding on angiogenesis understanding at the cell population level.

1.2 Experimental advances in sprouting angiogenesis

The scientific attempts to control angiogenesis started during the 1970s when the research team led by Judah Folkmann successfully developed methods to culture endothelial cells and induce vascular growth *ex vivo*. The experimental platform of angiogenesis during that early time includes the chick-embryo chorioallantoic-membrane (CAM) assay, the sustained-release polymers and the implantation of these polymers as pellets in the rabbit and murine cornea. These *in vitro* angiogenesis bioassays has allowed the Folkmann team to rapidly discovered and purified myriad of angiogenesis modulating agents that can be use for therapeutic purposes – especially a family vascular endothelial growth factor (VEGF) inhibitors.

1.2.1 In vitro assay of sprouting angiogenesis

While *in vivo* assays may better mimic the physiological states in which angiogenesis occurs, *in vitro* assay provide several advantage over the *in vivo* counterparts. These advantages includes the ability to manipulate the cell types, extracellular matrices, genetic manipulation, ease of result evaluation, and direct assessment of therapeutic agents. In this section, I briefly review a few *in vitro* assay that remain the mainstay of angiogenesis research.

- **Aortic ring assay**

  The aortic ring assay is an organ culture model in which angiogenic sprouts form from a segment of aorta containing native cell types and extracellular matrices [9, 70]. The rings of aortic explants are embedded in collagen gel and cultured in serum free medium for approximately one week. During this period, the aortic explants send out vascular outgrowths [80, 116]. that elongate, form branches and anastomose (fuse) into a capillary network (Figure 1-1). In this assay setup, some experimental conditions such as gel concentration and mechanical stiffness, and bulk concentrations of angiogenesis modulators can be modulated. The main strength of the assay are that the vessel outgrowths are anatomically similar to angiogenic sprouts *in vivo*. However, the variability in the handling of the rings and in the amount of sprouting active cells can significantly influence the sprouting responses.

- **Retinal explant culture assay**

  Retinal explant culture is another organ culture model that have been widely used. In this assay, retinal tissue containing microvascular is isolated from neonatal mice and culture *ex vivo*. This assay provides an advantage over the aortic ring assay in that the vascular sprouts are formed from microvascular endothelial cells (rather than aortic cells). This assay has been successfully been used to made important discoveries in angiogenesis. Such advances includes the identification of the specialized endothelial cell situated at the tip of vascular sprouts, the so-called tip cell [42, 92]. The main disadvantage of this assay is that retinal explants cannot be maintained for long-term culture. The retinal explants likely experience hyperoxic conditions and lesions made during the dissection typically leads to sprout regression by increased cell death or by vessel pruning.

- **Matrigel tube formation assay**

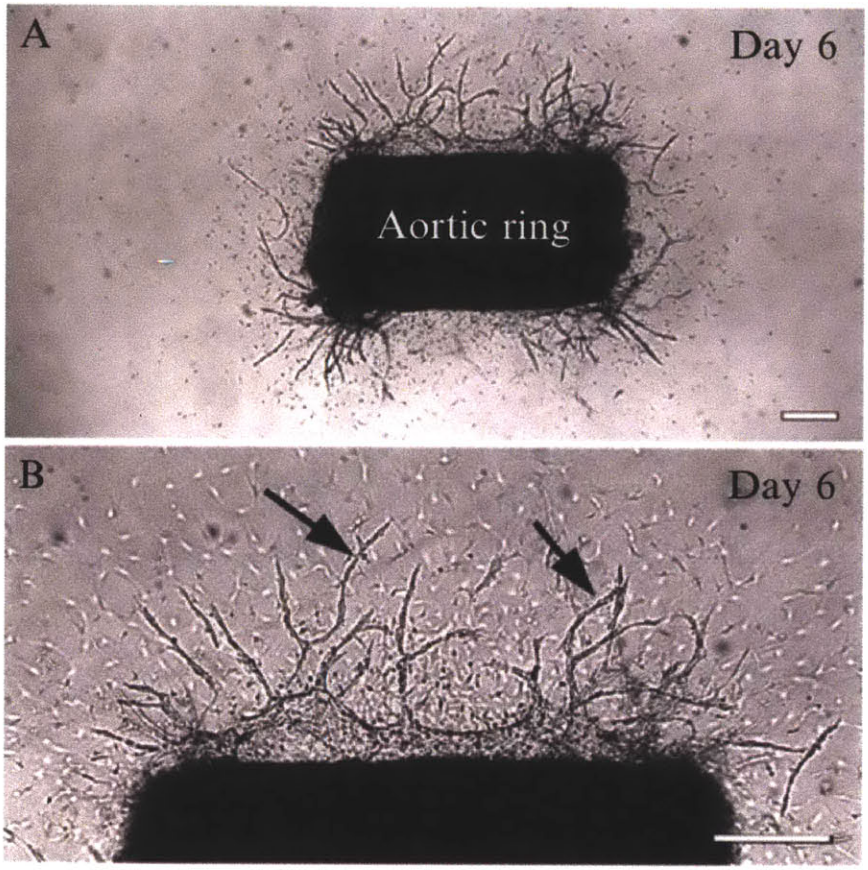

Figure 1-1: Angiogenic sprouts formation from a segment of mouse aorta. (a) Aortic ring in day 6 of culture in Type I collagen gel sends out numerous vascular outgrowth. (b) High resolution image of the same aortic ring explant reveals the continuous sprout formation led by invasive tip cells. Scale bar is 400 μm. Images are taken from a review by Aplin *et al* [9].

The matrigel tube formation assay is a cell culture model in which angiogenic endothelial cells form multicellular network like structure (referred to as "tube") when seeded on Matrigel. The ability of endothelial cells to form this two dimensional network structure has been referred to as capillary-like tubes and has been used as a measure of the endothelial cells' ability to form three dimensional network [16]. Due to the ease of assay setup and the reproducibility [10], the assay has been used to study various biological applications – to quantify the effects of pro- and anti-angiogenic factors and small molecule therapeutics, to screen for genes and proteins regulating angiogenesis [45, 44] and to characterize the endothelial progenitor cells [12, 76]. The assay result can be relatively easily

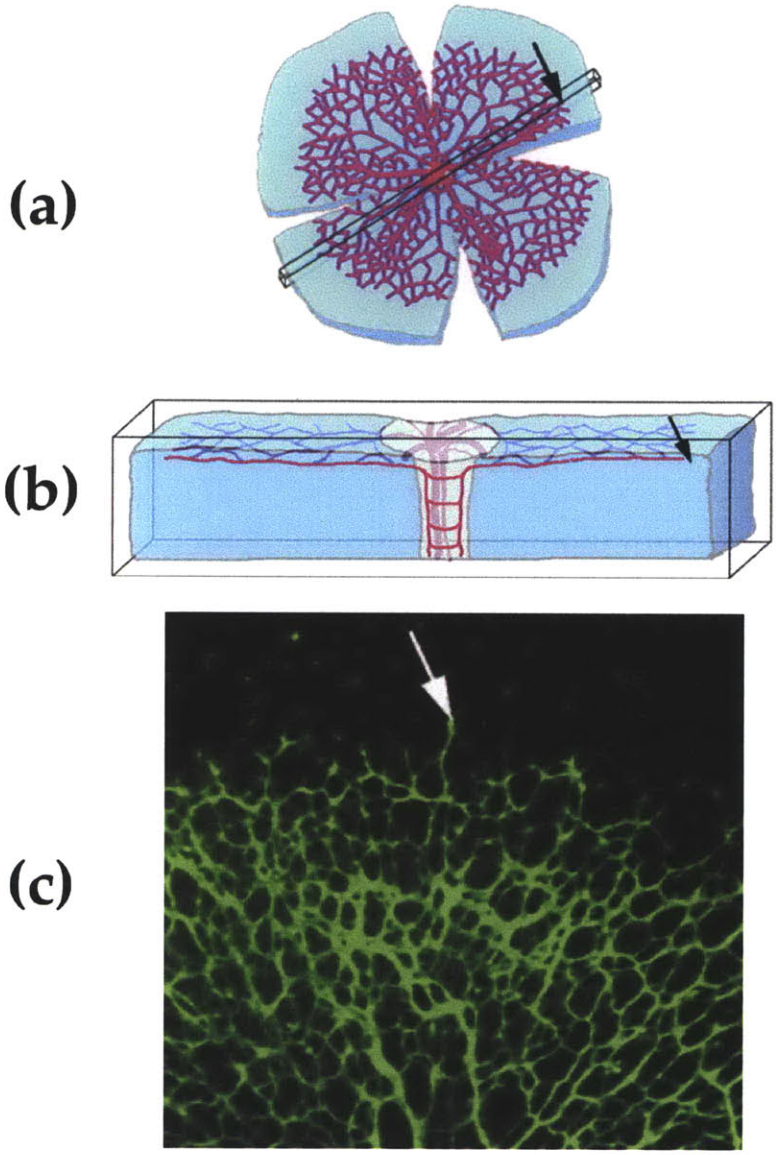

Figure 1-2: Neonatal mouse retinal explant culture sends out vascular outgrowths. The vascular development in this model system progress in a reproducible spatiotemporal manner. (a) Schematic presentation of an entire neonatal retinal explant with developing primary plexus of the retinal vascular network. (b). Schematic drawing of the explant's cross-sectional slab showing the sprouting angiogenesis in the fiber layer (top) of the retina, and subsequently in the deep layer. (c) Isolectin staining of the retinal vasculature revealing the invasive tip cell at the leading edge. Images are adapted from Gerhardt *et al.* [42]

assessed by 2 dimensional microscopy. One of the major criticism of assay is that the tube-forming ability has been reported in non endothelial cell types including fibroblasts.

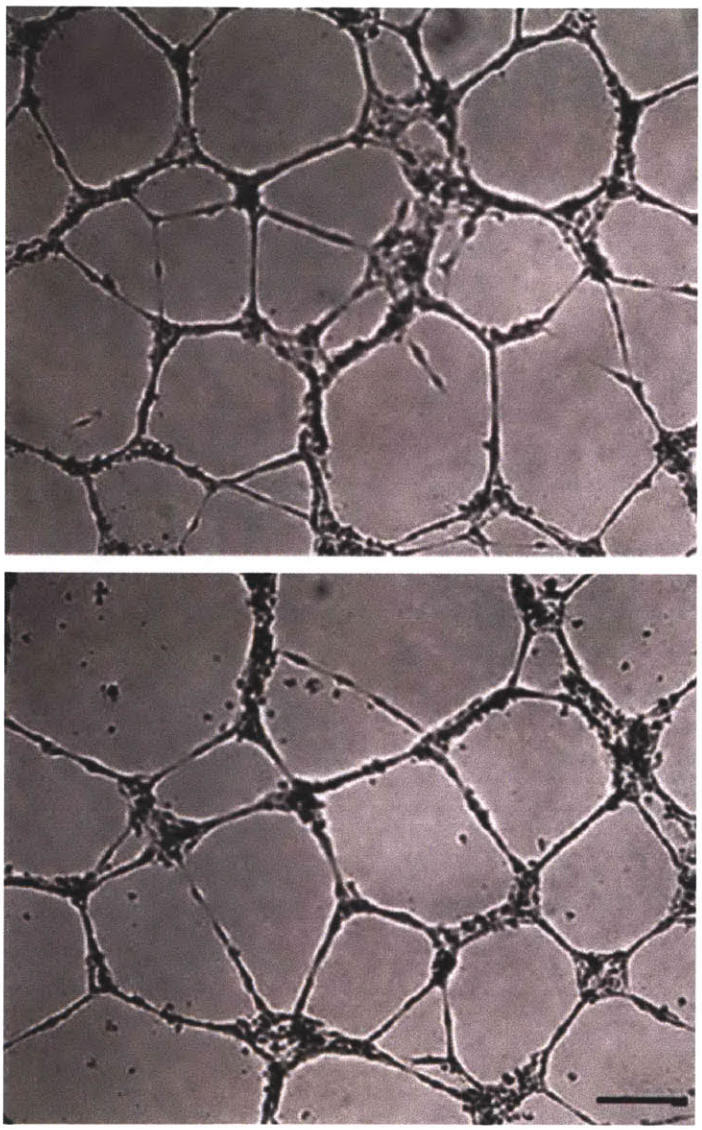

Figure 1-3: Angiogenic endothelial cell seeded on matrigel form network liked tubules on the gel. Representative images show the typical network structure formed after 24 hours culture on reduced growth factor Matrigel. Images are taken from Khoo *et al* [56].

- **On-gel sprouting assay and transwell assays**

  The on-gel sprouting assay is cell culture *in vitro* model. The experimental setup for this assay is similar to the matrigel tube formation assay setup. Angiogenic endothelial cells seeded as a confluent monolayer on Type I and Type II collagen and fibrin gels can invade the gel in 3D [15]. The main advantage of this assay are multiple folds. The on-gel invasion assay is relatively require a simple experimental setup and the results are reproducible. As such the assay can be used in a larger scale such as in screening studies. Contrary to the tube formation on Matrigel, the ability to form a continuous invasive sprout and capillary like network on these gels is unique to endothelial cells.

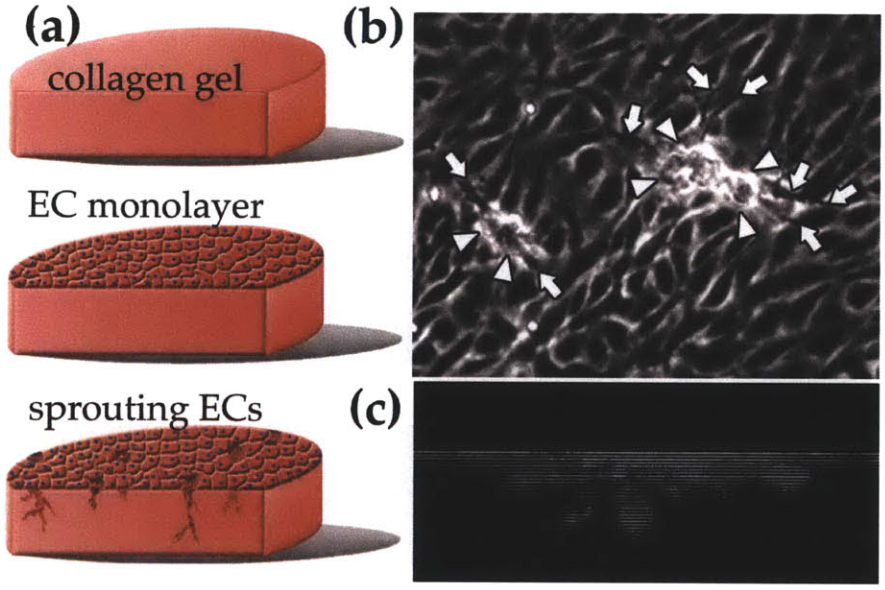

Figure 1-4: Experimental setup and representative images of sprout formation in on-gel cell culture model. Extracellular matrix such as collagen gel is prepared and casted inside a well of a transwell plate or of a glass bottom dish. After the gel solidify to a flat gel surface, endothelial cells is seeded at confluent monolayer seeding density. Cell culture medium containing growth factor can be added on top of the collagen gel monolayer. Images are adapted from Bayless *et al* [15]. (b) Representative images of invasive sprout formation imaged from top. (c) Confocal imaging of the sample showing the extent of sprout invasion. Images are taken from Yamamura *et al* [112].

- **Sprouting assay on microcarrier bead**

  Sprouting assay on microcarrier bead (aka microcarrier bead assay) is another

cell culture model of angiogenesis. HUVECs and hMVECs incubated with microcarrier beads in suspension adhere to the beads. The cells remain attach to the beads when transferred to a culture dish containing culture medium. When the coated beads are suspended in extracellular matrix including fibrin and collagen gel, angiogenic endothelial radially sends out vascular sprouts similar to those observed in aortic ring assays [79, 78]. The main strength of this assay are that the number of cells required is small and that the the cells are surrounded by extracellular matrix in 3D which better mimics the physiological environments.

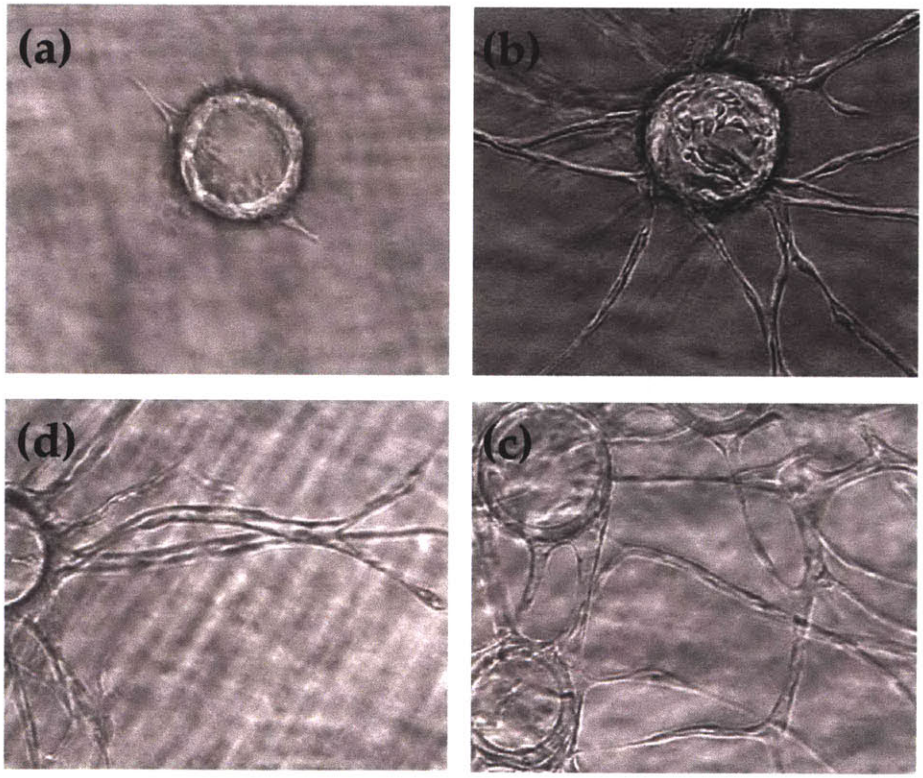

Figure 1-5: Representative images of sprout formation on microcarrier bead coated with angiogenic endothelial cells. Beads were embedded in fibrin gel(a) Human umbilical vein endothelial cell (HUVEC) coated bead form nascent sprouts on fibrin gel after 2 days in culture. (b-c) Continuous sprout continue to grow and extend away from the beads over longer period in culture. (d) Angiogenic sprouts from the same and different beads can fuse when they come into contact. Images are taken from [78, 77]

- **Microfluidic device assays**

In the cell culture model of angiogenesis discussed so far, the sprouting response is studied using macroscale culture systems, so termed for the inability to control cell patterning and biomolecular transport at length-scales down to a cell diameter. In recent year, the microfabrication technology has enabled the creation of 2D patterns and 3D scaffold. These microsystems have proven to be a powerful technology to study cell biology and tissue engineering, offering significant improvements over traditional cellular macroscale assays. Microfluidic technology allows for a wide variety of micro-channel dimensions and geometries [25] for generating soluble and insoluble gradients of biochemical factors, on-chip valving and pumping through multilayer fabrication [46] and incorporation of membranes [96] and three-dimensional extracellular matrices for increased functionality [28]. In addition to the ability to control the culture microenvironment, microfluidic assay requires much less experimental material – including cells, culture medium, extracellular matrix, and biochemical factors – than the traditional macroscale counterparts. As such it can be used when resources are limited such as for testing new pharmaceutical agents.

Many of tissue culture and cell culture experiments can be performed in microfludic devices. In recent years, several research groups have adopted the microfluidic technology for *in vitro* studies of sprouting angiogenesis [94, 28, 95, 27]. By combining the strength of the cell culture models (technical simplicity, manipulability, reproducibility) and of microfludic technology (the ability to control the microenvironment), microfluidic sprouting angiogenesis assays are now at the forefront of *in vitro* angiogenesis research.

In the recent studies, the Heilshorn group adopts the bead culture assay into a two channel microfluidic device. This microfluidic setup allows the group to investigate the effect of matrix stiffness on angiogenic sprouting response induced by vascular endothelial growth factor (VEGF) gradient [94]. Our own research group has developed a three-channel microfluidic device separated by

two gel regions. The exposure of angiogenic endothelial cells to two gel regions are useful as they can be used to test the same cell population under two microenvironments that differ only by one factor. One gel region can be used as no cytokine control region [28], or the two regions can be infused with gradients of two different biochemical, pharmaceutical factors[53]. The two gel regions can be filled with two types of extracellular matrices. Alternatively, the multichannel microfluidic system can be used for heterotypic cultures on angiogenesis by addition of a non-endothelial cell types in one of the two side channel [115, 103].

1.3 Computational modeling of angiogenesis

Computational modeling is a useful tool for studying specific questions pertaining to complex process such as angiogenesis. For the past two decades, computational models has used to study angiogenesis. These models can be classified by the approaches taken from a mathematical and computation ground.

- **Continuum based models**

  Continuum based modeling approximates the vascular tissue as a continuous series of entities [49, 6]. These approaches implicitly assume that individual cells that constitute the sprouting angiogenesis span much smaller length scale than the length-scale of tissue being model. The variations among the different parts of the tissue is accounted for by gradual transitions over individual cellular constituent. For this reason, the continuum models can be implemented by assigning one set of system of different equations as a continuous spread over the modeling space and time.

- **Discrete models**

  In contrast to the continuum approaches, discrete models describes the constituent parts of the tissue being model as discrete entitites such that their

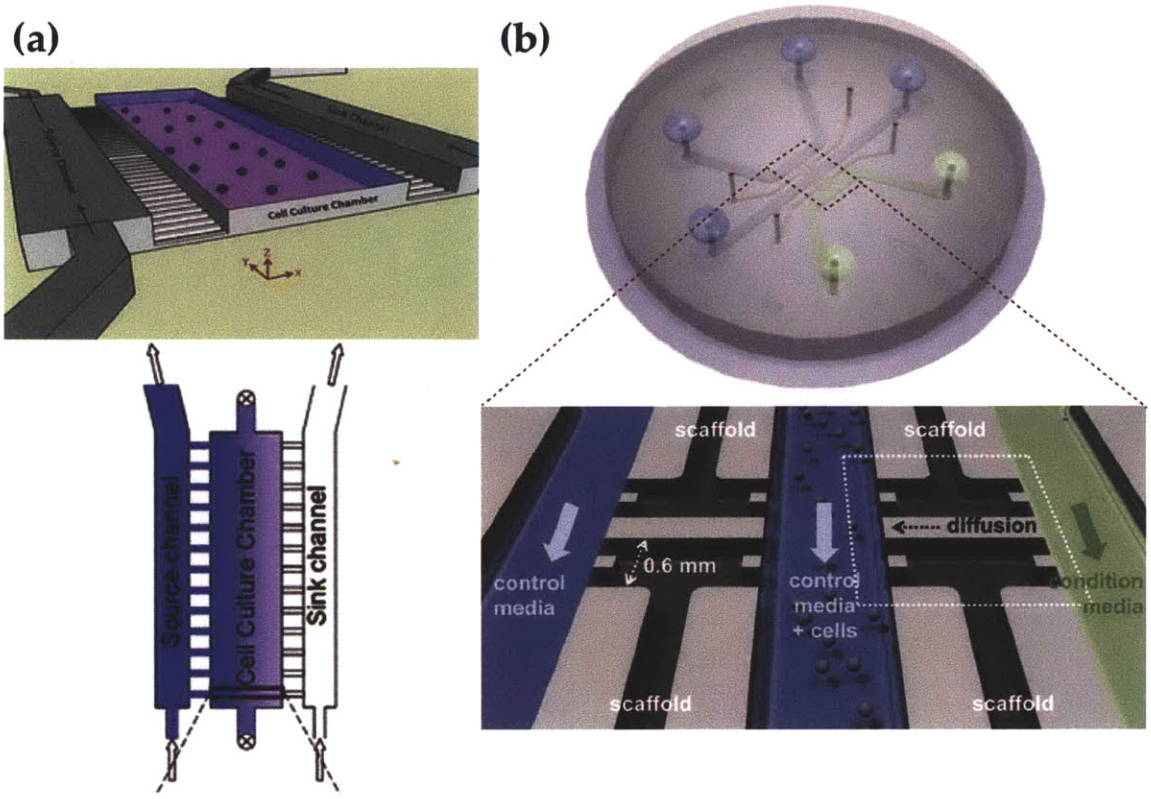

Figure 1-6: Microfluidic assays for studying sprouting angiogenesis. (a) Schematic drawing of the two-channel microfluidic device in which the bead assay is adopted. The device consists of two channels separated by a gel region. Endothelial cell coated beads are suspended in collagen gel and injected into the gel region through which the sprouting response can be observed microscopically. The images are taken from Shamloo *et al.* (b) Schematic drawing of the three-channel microfluidic device in which on-gel setup is adopted. The three channels are separated by two gel regions. Endothelial cells seeded in the middle channel can adhere to the extracellular matrix on both sides. The angiogenic sprouts can be observed within the gel regions with standard light microscopy. The images are taken from Chung *et al* [27].

unique and independent behaviors are explicitly represented [98]. These approaches discretize the modeling space and time as small increments. In the context of angiogenesis, discrete constituent units are individual endothelial cells. The model can be implemented by numerically solving the system of differential equations at discrete lattice points. An example of such approach is the Cellular Potts Model (CPM) developed by Glazier *et al* [43] and applied to model vascular morphogenesis by [71]. The main feature of CPM is the lattice-based description of cellular structure and their interactions which can

be described by agent-based interaction rules.

- **Stochastic vs. deterministic models**

  The evolution of the system can be described either deterministically or stochastically. In deterministic model, the state of the systems has no randomness associated with it such that the set of differential equation describing the evolution of the systems predict the systems' exact outcome - i.e., under the same model parameter and initial conditions, deterministic models always produce the same predictions. On the contrary, stochastic models describe the evolution of biological process probabilistically [99]. These models can accommodate the multiple possible outcome associated with biological process by using probability distributions to describe the outcomes in the simulation.

- **Hybrid and combined modeling approaches**

  Most of the recent modeling efforts in angiogenesis focuses on combining desirable aspects of the aforementioned modeling approaches. For example, in a hybrid stochastic agent deterministic field modeling approach [30, 111], the *cells* are described as discrete stochastic agents, while the chemical and biochemical environment within the *'field'* is governed by a continuous deterministic systems of differential equations. The solutions of the *field* equations in discrete space and time affects the behaviors of the stochastic cells.

In recent years, multi-scale modeling approach has become a powerful tools for studying angiogenesis which is inherently a multi-scale process [64]. The receptor-ligand binding of angiogenesis modulating factors, extracellular matrix cleavage, and corresponding intracellular signaling events occurs at the molecular level spanning diffusion time scale (in the order of 1 seconds [105, 34, 58, 65, 63]). These molecular events influence the changes in cellular behaviors that occurs at a longer time scale (in the order of minutes for intracellular signaling events and minutes to hours [59, 114] for transcriptional and translational changes). The collective changes at the level of cell population lead to tissue

tissue level response at an even longer time scale (hours to days). The integration of computational modeling across different length scales can be extremely powerful and essential as they are capable of predicting the effect of molecular and cellular intervention on tissue level outcomes.

As with most of the modeling approaches, there are certain challenges and limitations of computational approaches of modeling of angiogenesis. Understanding these limitations are crucial in enhancing our understanding of angiogenesis. The limitations of the computational issues can be include the simplifying assumption, parameter identification, and model validation. Excellent discussion of these issues are discussed in an excellent review by Pierce [83].

1.4 Predictive values of the computational models and requirement of quantitative experimentation

Computational modeling can be a powerful tool for address specific questions in angiogenic research. First, computational predictions often is valuable in suggesting potential hypotheses or addressing alternative and competing hypotheses in angiogenesis research. In addition, computational model can be used to determine experiments necessary in addressing those hypotheses. Recently, Bentley *et al* use their agent-based model of tip cell migration and selection to form a hypothesis and guide the experimental design for addressing the molecular mechanism of the tip cell selection [52, 17, 18].

Computational modeling is also useful in evaluating and predicting abstract quantities or quantities that are not easily measurable by experimental means. As an example, the concentration of growth factors or enzymes around a tip cell or on the endothelial monolayer maybe very difficult to measured and controlled experi-

mentally. These quantities can be computationally evaluated given the constitutive equations description their transport phenomana and the spatiotemporal scales of the computation. In addition, computational modeling is useful in identifying the keys parameters and evaluating the sensitivity of the system outcomes to these parameters.

Mathematical models especially the multi-scale approaches are emerging with capabilities to integrate biological understanding of the angiogenesis that span multiple spatial and temporal scales. Astute design of the modeling approaches in such a way that complement experiments can tremendously enhance our understanding of the angiogenesis process and ways to control it.

The main underlying hypothesis in this thesis work is that the complex cell behavior leading to sprouting angiogenesis is a consequence of cell-level decisions. Endothelial cells may follow trajectories in a state space containing sessile (S), proliferative(P), migratory(M), and apoptotic (A) states. As I discussed in Chapter 4 of this thesis, the multi-response transition among these phenotypic states can described as a stochastic process. With the appropriate stochastic model of the phenotypic transition, I addressed the parameter identification issue for a hybrid stochastic agent based model [30]. More specifically, I have designed and implemented experiment consistent with a hybrid discrete cell, continuous environment model of angiogenesis. The details of this method are discussed in Chapter 3, 4, and 5 of this thesis. This parameter estimation framework combined with corresponding intracellular measurements can be used to construct a predictive model of how intracellular signalings implicated in sprouting angiogenesis affect the state transitions in the stochastic model. We aim to develop a predictive signal-response-state model governing angiogenesis.

Chapter 2

Tissue level angiogenic response driven by phenotypic decision in acute inflammatory angiogenesis

2.1 Summary

Chronic wounds represent a significant burden to health care professional and patients. It has been reported that in the USA alone, more than 35 million cutaneous wound cases require major medical intervention annually, costing more than 20 million dollars [20]. As a result, the social and financial burden in support of chronic wound care is staggering [107]. One of the primary goals of better managing chronic wound and driving down this cost are to accelerate wound closure and achieve functional and aesthetic scars.

Successful wound healing depends on the formation of new blood vessel at the wound site (known as wound angiogenesis). In a typical healing wound, new capillaries appear in the wound bed 3 - 5 days after an injury. The formation of these new capillaries occurs in the context of granulation process at the wound site – the creation of a supporting matrix consisting of proliferative endothelial cells, migrat-

ing fibroblasts, and the deposition of new extracellular matrix especially collagen. Angiogenesis supports acute inflammation during wound repair process in a number of ways by providing nutrient supply and inflammation promoting cytokine environment. Failure in sprouting angiogenesis associated with impaired granulation is a hallmark of poorly resolved injuries leading to chronic wounds [107, 47]. As such, better understanding in the regulation of angiogenesis in wound healing not only is scientifically interesting, but also may suggest unforeseen therapeutic strategies in managing chronic wounds.

In this chapter, I report experimental results that address how two potentially counteracting inflammatory cytokines secreted during an early phase of wound healing affects a longer term angiogenic outcomes. The main goal of this study is to quantify the contributions of two mechanisms whereby PF4 - one of the most abundant proteins secreted by platelets during inflammation - can suppress VEGF-mediated angiogenesis.

2.2 Background and Motivation

2.2.1 Wound angiogenesis determines the switch regulating the development from acute to chronic wound

Wound healing is a finely coordinated process in which a damaged tissue repairs itself after an injury. Wound healing occurs in most multicellular organisms across the animal kingdom. The resolution of wound healing process ranges from complete regeneration (occurring only in fetuses and planarians) to development of chronic wounds and scars. An important step in determining whether an injury will heal completely or develop into a chronic wound is wound angiogenesis.

In the classic model, wound healing process is divided into 3 to 4 sequential phases:

hematostatic (not recognized as a separate phase by some experts), inflammatory, proliferative, remodeling phases. These phases are distinct in cellular activities, but can be overlapping in timing. For example, the onsets of hematostasis and the inflammatory phase occur almost simultaneously.

Onset of injury to an endothelium immediately sends off signals that start the hematostatic (the process that stops bleeding) and inflammatory phases of wound healing. Early events during these phases includes the activation of the coagulation cascade that leads to platelet recruitment and activation. To achieve hematostasis, recruited platelets aggregate and form platelet plug at the injury site on the endothelium. Aggregated platelets also activate the coagulation pathway that leads to fibrin clot formation. This clot acts to further control active bleeding and tissue losses.

In the inflammatory phase, innate immune cells including neutrophils are recruited to the wound site to remove bacteria and debris. Aggregated platelet secretes a myriad of factors that contributes crucially to the recruitment of neutrophils and macrophages and usher the next phase of wound healing [20, 47]. The inflammatory phase typically last 2 to 4 days in healing wounds.

The next phase of wound healing - the proliferative or new tissue formation phase - is characterized by cellular migration and proliferation of various cell types. Peaking in number during this phase, fibroblasts initiate sprouting angiogenesis, epithelialization and collagen formation. Sprouts of new capillaries replace the fibrin clot with granulation tissue which serves as new substrate on which keratinocytes migrate to cover the injured tissue [47]. This phase occurs after the inflammatory phase approximately 3 day post injury and can last from 10 days or more. In tissue injuries with dysregulated angiogenesis such as in diabetic or ischemic wounds, the wound healing process stalls in the inflammatory phase for a long period of time and evolves into a chronic wound [14]. Sprouting angiogenesis plays an important role in determining this development as it is reported that application of a potent angiogenic factor

VEGFA can normalize the healing [33, 11, 24, 90, 72].

The last phase of wound healing - the remodeling phase is characterized by resolution of all of active cellular processes, increased collagen deposition and reorganization, and mobilization of cells out of the wound site. During this phase myofibroblast differentiates into myofibroblast and causes tissue contract. Most of the capillaries disintegrates as the endothelial cells undergo apoptosis, while neutrophils and macrophages exit the wound site.

The switch in tissue level response from acute and healing wound to a chronic wound occurs between the inflammatory and the proliferative phases of wound healing. This decision is primarily determined by the platelet-secreted cytokine environment during the inflammatory phases which in turn determines the extent of sprouting angiogenesis at the wound site.

Platelets contributes crucially to multiple physiological and pathological processes in mammalian biology. They are involved in thrombosis, haemostasis, inflammation, angiogenesis and atherogenesis. Most of platelets' involvement in myriad of physiological processes are mediated by the chemical regulators that are synthesized in megakaryocytes and stored within platelets' α granules.

Platelets are known to store and release a large number of proteins within their α-granules including angiogenic factors (angiogenin, VEGF), and angiostatic/anti-angiogenic factors (endostatin, angiostatin, PF4) [29]. At sites of vascular injury, circulating platelets adhere to collagen fiber of the subendothelial basement membrane, followed by aggregation and release of their α and dense granules. Surrounding potentially harmful pathogens exposed to high concentration these chemical are killed. In addition to pathogen killing, platelet aggregation and α-granule secretion creates a biochemically rich microenvironment that activates surrounding tissue especially the injured endothelium itself.

Some of the platelet secrete cytokines during the inflammatory phases have been reported to have opposing functions. As such, it is unclear how these cytokine release is regulated and how such regulation may affect wound angiogenesis. There are multiple lines of hypotheses suggesting that the regulation occurs at the level of platelets through selective cargo-sorting into α-granules and/or differential α granules release. Alternatively, the regulation can occur at level of endothelial cell response. By simultaneously secreting factors with opposing functions on the endothelium, the platelet could exert a finely balanced effect at the damage site. In this chapter, we will address this possibility in the context of the opposing potent cytokines released by activated platelets: the angiogenic VEGF and the angiostatic PF4.

2.2.2 VEGF and PF4 are important and relevant inflammatory cytokine determining the tissue level sprouting angiogenesis in wound healing.

Platelet factor 4 (PF4 aka CXCL4) is one of the most abundant protein released during platelet activation. It belongs to a CXC family cytokine family as it was previous found to promote neutrophil chemotaxis (which was later shown to be due to contamination by other CXC family members). It is predominant synthesized in megakaryotes residing in bone marrow, stored in platelets' α granules and are released upon the onset of acute inflammation.

From its early studies, PF4 has been reported to be mainly involved in the coagulation pathway. PF4 can bind to heparin with a notably high affinity and avidity , thereby neutralizing heparin's anti-coagulation activity. It is of note that this prothrombotic effect of PF4 is achieved only at high concentration (3 - 10 μg/mL). This high local concentration range of PF4 has been reported on injured vascular wall within minutes of platelet recruitment and disappeared after several hours [109]. In

addition to its role in modulating heparin activities, PF4 have been reported to be able to suppress basic fibroblast growth factor (b-FGF) and VEGF modulated angiogenic sprouting. Recently, the PF4's specific receptor has been identified. However, the signaling cascade downstream of PF4 that may regulate PF4's angiostatic activity have not yet been elucidated in details.

Vascular endothelial growth factor (VEGF) is the first and among the best studied pro-angiogenic cytokine. VEGFA, the predominant form of VEGF ligand, belongs to a family of growth factors, ubiquitously expressed in vascular cells in arteries, veins, and lymphatics [36, 35]. It activates proliferation only in cells of vascular origin including in human umbilical vein endothelial cells (HUVECs) and human microvascular endothelial cells (hMVECs). It also functions as a survival factor for endothelial cells *in vivo* and in serum-depleted endothelial culture [61], possibly by inducing the expression of anti-apoptotic protein Bcl-2 [41]. VEGFA interacts with both VEGFR1 and VEGFR2, the two main VEGF receptors expressed in HUVECs and hMVECs. VEGFR1 is a decoy receptor and VEGFA binding to VEGFR1 does not trigger intracellular signaling. Only the binding of VEGF to VEGFR2 leads to receptor autophosphorylation and recruitment of a number of signaling adaptor proteins. *In vivo*, VEGF has been shown to induce vascular permeabilization and angiogenesis.

VEGF and PF4 have been detected in α-granules of unactivated platelets [23]. Physiological levels VEGF and PF4 can be detected in thrombin induced platelet aggregation *ex vivo*, suggesting that VEGF and PF4 are released by platelets during an early phase of inflammation. Given the potential roles of VEGF and PF4 involving a fine regulation of angiogenesis outcome, we set out to investigate the effect of VEGF and PF4 at the single cell decision level leading to tissue level responses. The effect of VEGF and PF4 on the tissue level outcome will be discussed in this chapter, while the single cell decision results will be discussed in chapter 4.

Using multiple tissue level angiogenic assays, we examine whether the simultaneous treatments of VEGF and PF4 can regulate successful angiogenesis. If so, the angiogenic switch regulating acute to chronic wound outcome does not necessarily occur only at the platelet secretion level but also at the endothelial cell response level. More specifically, we determine whether there are VEGF and PF4 concentration ranges within which the tissue level response switches (between no sprouting vs. with extensive sprouting).

In this chapter, we demonstrate that highly angiogenic primary endothelial (HUVECs and hMVECs) express high levels of VEGFR2 and CXCR3, receptors specific to VEGF and PF4 respectively. Using an *in vitro* microfluidic angiogenic sprouting assay and a more traditional bulk ongel angiogenic assay(collagen gel invasion assay), we show that PF4 dose-dependently suppresses VEGF mediated angiogenic sprouting of hMVEC and HUVECs cultured on Type I collagen gel measured in term of sprout density, sprout length, and sprout diameter. The concentration range at which the suppressive effect occurs falls within the two ends of the physiological ranges of PF4. Using a Matrigel cord formation assay, we show that PF4 reverses VEGF stabilization of endothelial cord of hMVECs and HUVECs. In addition, PF4 reverses VEGF induced changes in cell morphology and cell-cell adhesion of hMVECs cultured on type I collagen gel. To tease out the molecular details of PF4 effects in modulating VEGF-induced endothelial cell responses, we consider two types of mechanisms of PF4 on VEGF mediated sprout formation. First, because of its high affinity and avidity to HSPG, PF4 can interfere with VEGF recruitment by heperan sulfated proteoglycans (HSPG) and we refer this potential mechanism as *extracellular*. Alternatively, PF4 can bind to its specific receptor CXCR3 highly expressed in HUVECs and hMVECs, thereby triggering signal transduction that potentially cross-talks to VEGFR2 mediated signaling. By assuming that the two mechanisms linearly combine to determine the VEGF mediated sprout density, length, and diameter, we propose the scheme by which we can quantify the relative contributions of the two potential mechanisms.

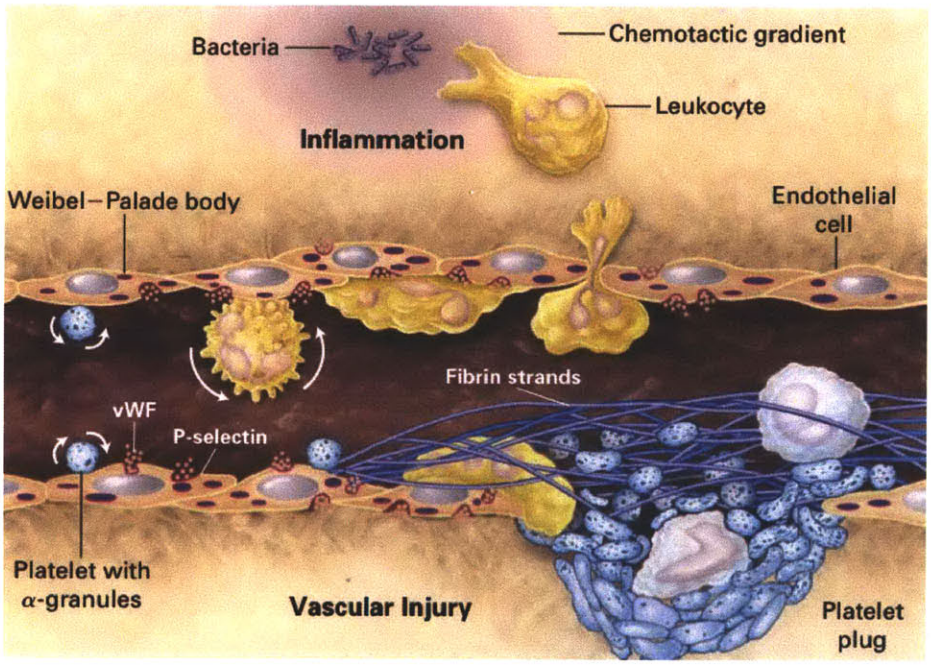

Figure 2-1: The series of events following the onset of vascular injury during the early stage of wound healing. In the moments after an injury occurs, components of blood coagulation and inflammatory cascades are needed to prevent ongoing blood and tissue losses. First, as part of the coagulation response, circulating platelets recruited to the injury site adhere to the injured endothelium and form platelet plug. Platelets also mediate the activation of thrombin leading to conversion of fibrinogen to fibrin which helps seal the damaged endothelium [109]. The plug forming aggregated platelets secretes high concentration of VEGF and PF4 that can potentially act upon the endothelial cells at the injury sites. The illustration is modified from Frenette *et al* 1996 [39].

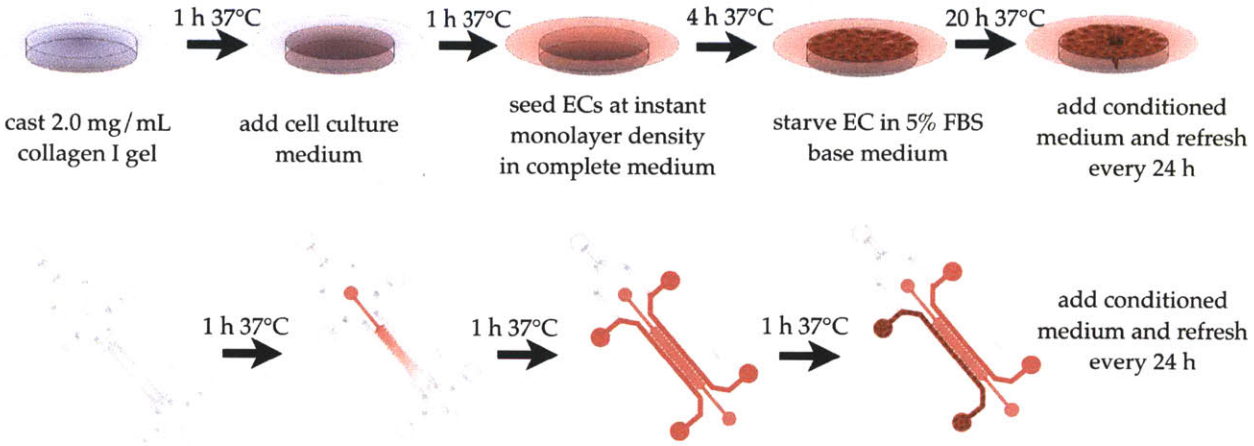

Figure 2-2: Angiogenic sprouting assay setups. (a) Schematic drawings of the on-gel sprouting assay setup. Type-I Collagen gel was prepared as previous described. (In [28] 2.0 mg/mL pH 7.4 Collagen gel has previously been shown to promote angiogenic sprout formation of hMVEC in microfluidic devices). The gel was evenly spread into individual well of a multi-well glass bottom plate, let solidified at 37°C in humidified environment and soaked in cell culture medium for at least 1 hour before cell seeding. hMVECs and HUVECs suspended in cell culture medium was allowed to adhere for 4 hours. For cytokine studies, adhere cells were incubated with low serum medium (5% FBS suppplemented base medium) for 20 hours, completing a 24 hour after seeding period. Cells were refreshed with VEGF and PF4 containing medium every 24 hours until the assay end point (72 hours after cytokine treatment). The entire samples were fixed with 4% paraformaldehyde, permeabilize, and stained with DAPI and Phalloidin to visualize the angiogenic sprout formation. (b) Schematic drawings of the high throughput microfluidic devices for an *in vitro* angiogenic sprouting assay. The device consists of two fluidic channels (flanking an extended gel regions). Collagen I gel was injected during standard micropipette tips into the gel region through the gel filling port. Cells are culture medium were introduced into the device after the gel solidification through the cell seeding and media ports. Cytokine containing medium were refreshed every 24 hours since the start of the treatment.

2.3 Material and Methods

2.3.1 Angiogenic endothelial cells source

Primary human adult microvascular endothelial cells (hMVECs) from dermal origin and primary human umbilical vein endothelial cells (HUVECs) were purchased (Lonza NJ; Cat.No. CC-2543 and CC-2519 respectively) and maintained according to manufacturer's instruction. The cells were used at passaged 7 for all on-gel sprouting assay, unless indicated otherwise.

2.3.2 On-gel sprouting (collagen gel invasion) assay

Type I rat tail collagen (BD Bioscience; Cat.No. 354236) diluted in 0.02 N Acetic acid to 2.0 mg/mL at pH 7.4 was prepared on ice and was immediated casted in glass bottom 24-well multi-well plate (MatTek Corp; Cat.No. P24G-0-13-F) and allowed to solidify at 37°C for 30 minutes in a humidified environment. After gel solidification, cell culture medium was added to the plate to prevent the gel from desiccation. After at least 1 hr of medium incubation with collagen gel, hMVECs or HUVECs introduced at instant monolayer density (50000 cells/cm^2) which consistently were allowed to adhere to the gel. At this seeding density, HUVECs and hMVECs consistently formed a confluent endothelial monolayer on collagel gel at 18 hours after seeding (Figure 2-2). To test the effect of cytokine conditions on sprouting, cytokine containing medium was introduced at 24 hours after seeding. The conditioned media were refreshed every 24 hours until the end of experiment (72 hours after seeding, unless indicated otherwise).

2.3.3 Angiogenesis sprouting assay in a *high throughput* microfluidic device (HTD)

PDMS device preparation

High throughput microfluidic photoresist pattarned silicon wafer mold was designed in house and custom-ordered from the Stanford University Microfluidic Foundry. The microfluidic system consisting of PDMS (polydimethylsiloxane; Silgard Dow Chemical, MI; Cat.No. 184) was prepared on SU-8 2050 photoresist-patterned wafers (MicroChem, MA) using a standard soft lithography process described previously [26, 28]. The fabricated PDMS channel and the microscopy grade cover slip used to seal the channel were sterilized and dried at 80°C overnight. Subsequently, they were plasma treated (Harrick, CA) in air, and bonded together to form a closed microfludic channel. After the plasma bonding, all microfluidic channels were coated with 1 mg/mL poly-D-lysine hydrobromide (Sigma-Aldrich St. Loius, MO; Cat.No. P7886) and incubated for at least 4 hours at 37°C in a humidified environment. The device was then washed thoroughly with sterile water and dried at 80°C overnight to allow the PDMS surface to return to its native hydrophobicity – a crucial surface property in confining the extracellular matrix within a specified region.

Extracellular matrix casting and cell seeding

Microfluidic device that have been bonded, sterilized and surface treated were brought to room temperature prior to gel injection. Type I rat tail collagen is diluted to 2.0 mg/mL concentration and calibrated to pH 7.4 as in the on-gel sprouting assay. While at 4°C, the collagen gel solution was carefully injected into the microfluidic gel region through a gel filling port using a standard 200 μL micropipette tip. The collagen gel was allowed to solidify at 37°C in a humidified chamber for at least one hour. After gel solidification, 37°C cell culture medium was flown into the device on both sides of the gel through the medium ports. The gel was incubated with the cell culture medium for at least one hour before cell seeding. At the cell seeding time, hMVECs

and HUVECs cell suspensions were diluted to the instant monolayer seeding density, flown into the channel, and allowed to adhered for at least one hour prior to additional medium filling.

Inflammatory cytokine treatment

After at least 24 hour of seeding in cell culture medium (EGM2MV; Lonza NJ Cat.No. CC-3202), hMVEC culture were switched to conditioned medium containing specified concentrations of recombinant human VEGF and PF4 (Peprotech NJ; Cat.No. 100-20 and 300-16 respectively). Conditioned media were refreshed every 24 hours onward.

2.3.4 Angiogenic sprout visualization and quantification

Sprouting endothelial cells in HTD were visualized under a phase contrast microscope every 24 hours after seeding. Images were taken and analyzed using an image processing MATLAB script developed in house. At the end point of the assay, 3D images of DAPI and Alexa-568 Phalloidin (Molecular Probes, Eugene, OR; Cat.No. A12380) stained samples (in ongel and HTD setups) were imaged using a laser scanning microscopes (Zeiss LSM510 and Olympus FV1000).

2.3.5 Tube (cord) formation assay

Growth factor reduced, phenol red free Matrigel (BD Biosciences, Bedford, MA; Cat.No. 356231) were used at 100% concentration, managed while on ice, and casted on to wells of 24 well plate prior to seeding. Gel was allowed to solidify for 30 mins 37°C in a humidified chamber. hMVECs suspended in cell culture medium were seeded onto solidified Matrigel at the instant monolayer density (50,000 cells/cm^2). Under this condition, hMVECs tube formation can be seen on the Matrigel at 18 - 24 hrs after seeding. Condition media containing specified concentrations of VEGF and PF4 in base medium (5% FBS EBM-2; Lonza NJ; Cat.No. CC-3156) was refreshed every 24 hours after seeding onward.

2.3.6 siRNA transfection

CXCR3 level in HUVECs and hMVECs were knocked down by a validated CXCR3 siRNA pool (Dharmacon Lafayette CO; Cat.No. L-005472). HUVECs and hMVECs were seeded at low density to achieve 25 - 30% confluence at the time of siRNA transfection. On the day of transfection, transfection media were prepared according to manufacturer's recommendation. siRNA delivery was ensured by the visualization of Cy3-labeled oligos 4 hours after transfection. After 4 hours of siRNA incubation, cells were refreshed with antibiotic free, serum and growth factor containing medium for 20 hours before antibiotic is added back.

2.4 Results

2.4.1 PF4 suppresses VEGF-induced induction of angiogenic sprouting in both on-gel sprouting assay and microfluidic devices

To determine whether the regulation of angiogenic outcome in inflammatory angiogenesis occur at the endothelial cell level, we quantitatively characterized the angiogenic response following VEGF and PF4 treatments. In the absence of any growth factors, both HUVECs and hMVECs can form a complete monolayer on type I collagen gel, but their angiogenic activities are minimal with HUVECs consistently being less invasive and sending in fewer angiogenic protrusion into the gel. Consistent with previous findings, 20 ng/mL VEGF increases the overall angiogenic sprout density both in HUVECs and hMVECs. More specifically, VEGF and PF4 effectively modulates angiogenic sprouting densities at their respective physiological concentrations – 20 ng/mL for VEGF; 500 ng/mL for PF4 during the inflammatory phase of wound healing (Figure 2-3 a and b).

The observed angiogenic sprouts can be classified based on their attachment to the endothelial monolayer at the gel interface; class 1: attached nascent sprout, class

2: detached. Attached sprout (class 1) often consists of multiple cells (string of cells) or starts off with a single cell but subsequently develops into a multicellular sprout (forming string of cells) and forms cell enclosed lumen. The attachment and the lumen formation are important characteristic of functional angiogenic sprout (Supplementary Figure 1 (Section 2.6)). On the other hand, detached sprout (class 2) fails to maintain the contact with the monolayer and only contains a few invasive cells. Based on high resolution imaging data, only the class 1 sprout will lead to a functional vascular network. We found that VEGF strongly increases the density of attached (class 1), but only minimally affects the density of detached sprout as measured at 24, 48, and 72 hours of cytokine treatments in microfluidic devices (Figure 2-3b and d).

To examine the effect of VEGF and PF4 on sprouting angiogenesis over a wider range of concentrations, we performed a dose response sprouting experiment. We first performed the assay in high throughput microfluidic devices (HTDs). However, the device-to-device variabilities make the assay less scalable and the HTD based dose response results less reliable. As such, we moved to performing the assay in multi-well glass bottom plate - the platform in which image-based quantification of the result remain possible and the results are more reproducible.

In adopting a new experimental setup, we first validated that the HUVECs and hMVECs can be induced to form angiogenic sprout in an ongel assay and that the resulting sprouts are comparable in size and morphology to those observed in HTD (Figure 2-4a). At 72 hours after the treatments, we observed dose dependent increase in sprout density of hMVECs seeded on type I collagen in the ongel assay (Figure 2-4b). This increased sprout densities were dose dependently suppressed in response to increasing PF4 concentration in the background of 20 ng/mL VEGF (Figure 2-4c). The dose response range of VEGF spans the entire tested range (0 - 80 ng/mL) and the response is almost linear from (0 - 40 ng/mL). On the other hand, the dose response curve of PF4 is characterized by a narrow transition range (compared to

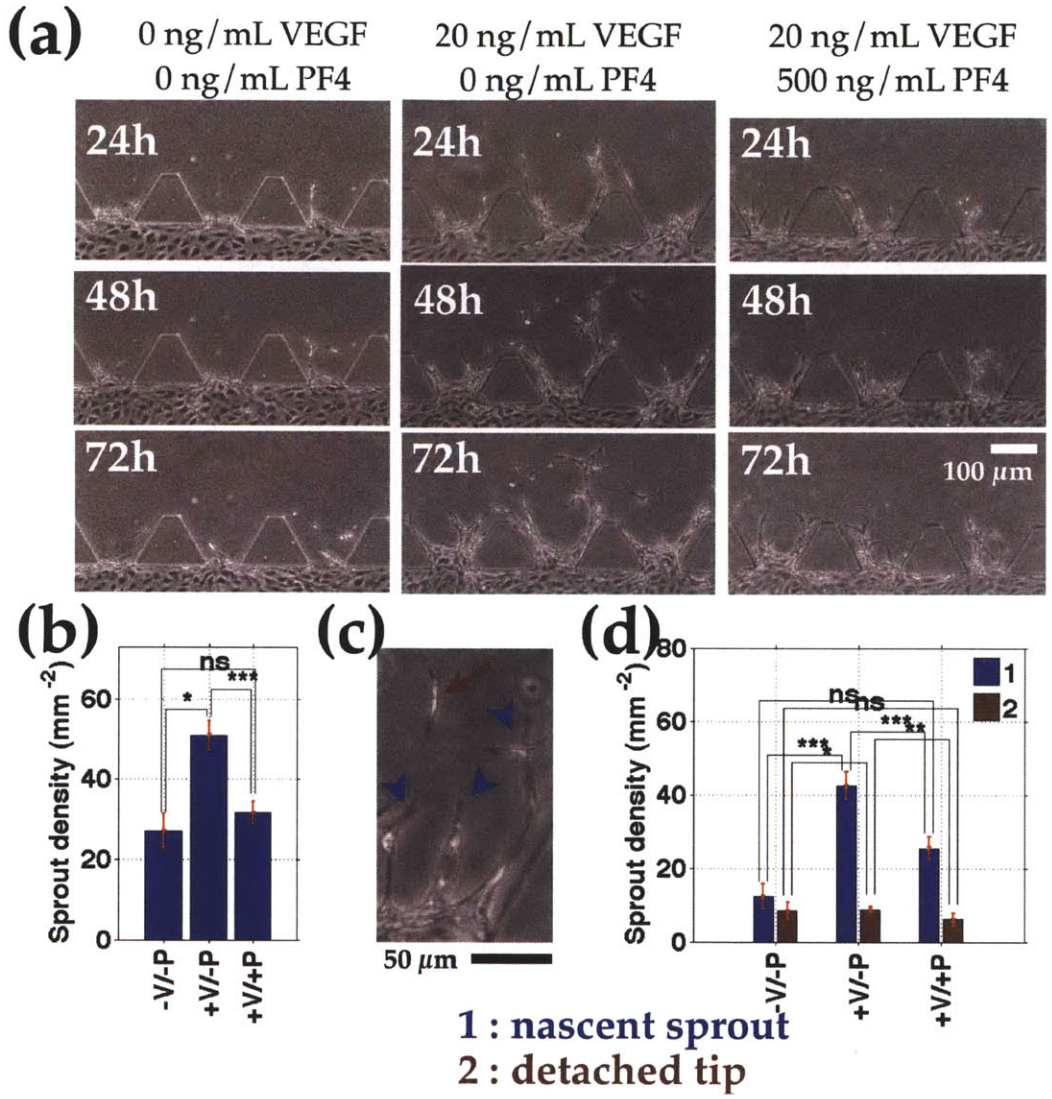

Figure 2-3: VEGF and PF4 modulate angiogenic outcomes. (a) Representative images showing the varying extent of angiogenic sprouting of HUVECs observed after 24 - 72 hours of treatments (20 ng/mL VEGF and 500 ng/mL PF4). (b) Quantification of sprout density of HUVECs observed after 72 hours of treatments. (Statistically significant difference are denoted as follow: $***-p \leq 0.005$; $*-p \leq 0.05$; ns - $p > 0.05$ (not significant)). (c) High resolution image of angiogenic sprouts in microfluidic devices showing class 1 (blue arrow heads) and class 2 (red arrow) sprouts. (d) VEGF and PF4 differentially affects nascent attached sprout (class 1) and detached sprout (class 2). VEGF significantly increases the average density of class 1 sprout but does not significantly affect class 2 sprout density. PF4 suppresses the effect of VEGF induced increase in class 1 sprout density.

the test range) of 10 - 80 ng/mL PF4. Notably, the transition range (range of PF4 concentration at which transition occurs) falls within the bracket of reported physiological PF4 concentration – 2 - 10 ng/mL in the plasma (no inflammation) and 5 - 10 μg/mL in serum [109] (generated by thrombin-mediated platelet aggregation and coagulation as occurring during inflammation).

In addition to quantifying sprout density, we examined additional sprout characteristics that may indicate the quality of sprout formation under the same VEGF and PF4 concentrations. These characteristics are sprout length, invasion depth, and sprout diameter. Sprout length measures the contour length of an attached sprout from the invasive tip to the base of the sprout at the gel interface where it comes into contact with the monolayer. This quantity reflects the extent to which individual sprout has extended within a gel. Invasion depth represents the perpendicular distance from the base of the sprout to the invasive tip. This quantity indicates how persistent individual sprout is in moving away from the monolayer and invading collagen gel. Lastly, sprout diameter represents the width of the sprout at the gel interface. This quantity reflects the ability of sprout to become part of a functional conducing vascular network.

HTD sprouting assay under selected VEGF and PF4 concentrations shows that 20 ng/mL of VEGF significantly increases sprout length and invasion depth and significantly decreases sprout diameter (Figure 2-5a-c). High concentration of PF4 only mildly suppresses sprout length and invasion depth. On the other hand, PF4 suppresses VEGF-induced reduction in sprout diameter. Ongel sprouting assay reveals the effect of dose response of the aforementioned sprout characteristics. Under a constant concentration of VEGF, increasing PF4 concentration does not significantly affect sprout length, and invasion depth. These results is consistent with the effect of PF4 found in microfluidic devices.

Taken together these results indicate that endothelial cells respond to the oppos-

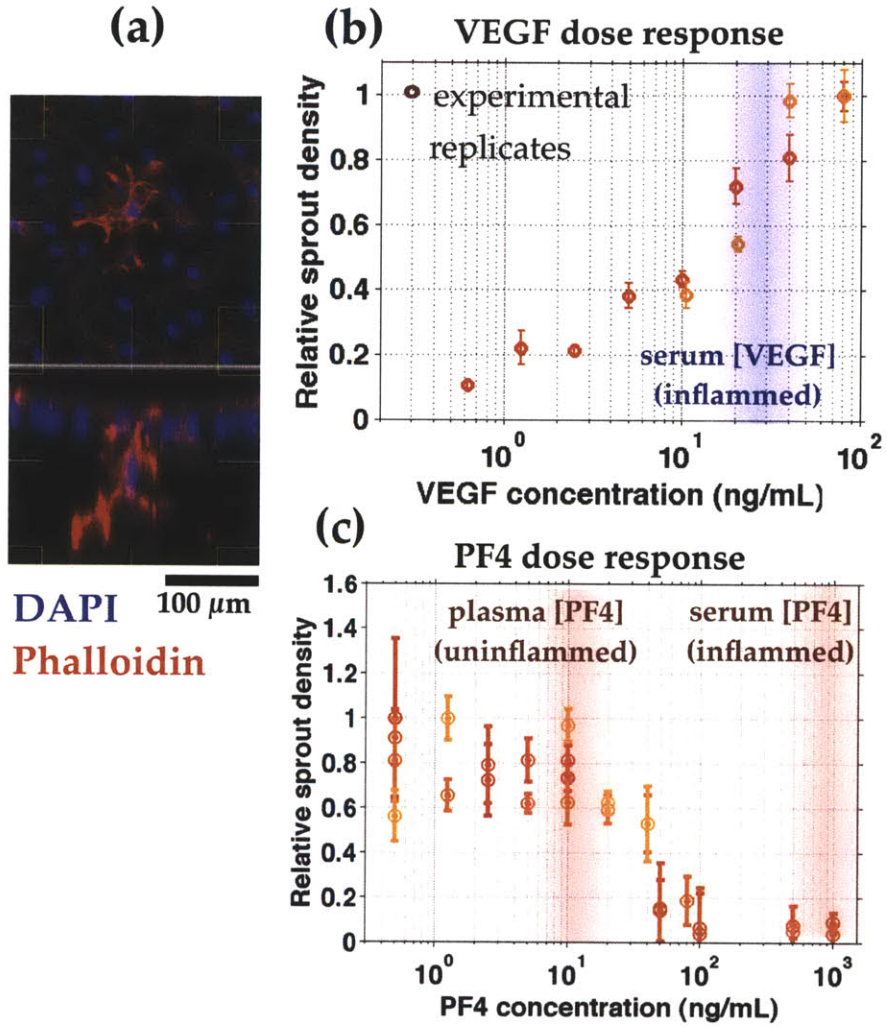

Figure 2-4: Inflammatory cytokine modulates the tissue sprout density in an *in vitro* on gel assay of angiogenesis. Human microvascular endothelial cells (hMVECs) cultured on Collagen I gel can form angiogenic sprout that invades into three dimension (a). The extent of sprout formation measured as sprout density (number of sprout per unit gel a rea) can be modulated by treatments with inflammatory cytokines (VEGF and PF4) (b). VEGF dose dependently increases sprout density after 72 hours of treatment. On the other hand, platelet factor 4 (PF4) dose dependently reverses the sprout-inducing effect of VEGF measured after 72 hours of treatment. It is of note that in the PF4 dose response curve, the sprout density change within a narrow window of PF4 concentration. This transition window falls within the two physiological concentrations of PF4. The lower end coincides with the reported PF4 concentration in plasma (7 ng/mL) where is not inflammation. On the other hand, the higher end of this range coincides with the reported range of PF4 in serum (3 - 10 μg/mL) extracted from aggregated platelets, similar to that occurs during an early state of inflammation.

ing inflammatory cytokines VEGF and PF4, which are secreted by activated platelets during the inflammation phase of wound healing. These observations indicate that angiogenic switch regulating the outcome of wound angiogenesis can occur at the endothelial cell level irrespective to whether platelet cytokine secretion occurs in thematic manner. More specifically, our results suggest that VEGF promotes lengthy and invasive sprout formation. PF4 modulates the sprout responses by causing a reduction in sprout density and sprout diameter without changing how far and how persistent sprout invades the gel. Recall that sprouting angiogenesis can be divided into the following sequence of events: (1) tip/stalk cell selection; (2) tip cell navigation and stalk cell proliferation; (3) branching coordination; (4) stalk elongation, tip cell fusion, and lumen formation; and (5) perfusion and vessel maturation. The quantified sprouting responses suggest that PF4 most strongly affects the tip/stalk selection step, but has minimal effect at the tip cell navigation, stalk cell proliferation and stalk elongation steps.

2.4.2 PF4 reverses VEGF-mediated deceleration of endothelial cord dissociation

To examine the role the PF4 in regulating sprout formation on a more physiological substrate, HUVECs and hMVECs were analyzed for their ability to form tubes on growth factor reduced Matrigel in the presence of VEGF and/or PF4. HUVECs and hMVECs seeded on Matrigel form network-like structure on gel. This network structures gradually dissociate over multiple days in culture. VEGF helps maintain the network structure over at least 36 hours. Addition of PF4 significantly accelerates cord dissociation (Figures 2-6).

To quantify the different level of cord dissociation in the presence and absence of physiological PF4 concentrations, we computed the fractional area covered by the endothelial cord, branch point density and end point density. When endothelial cords

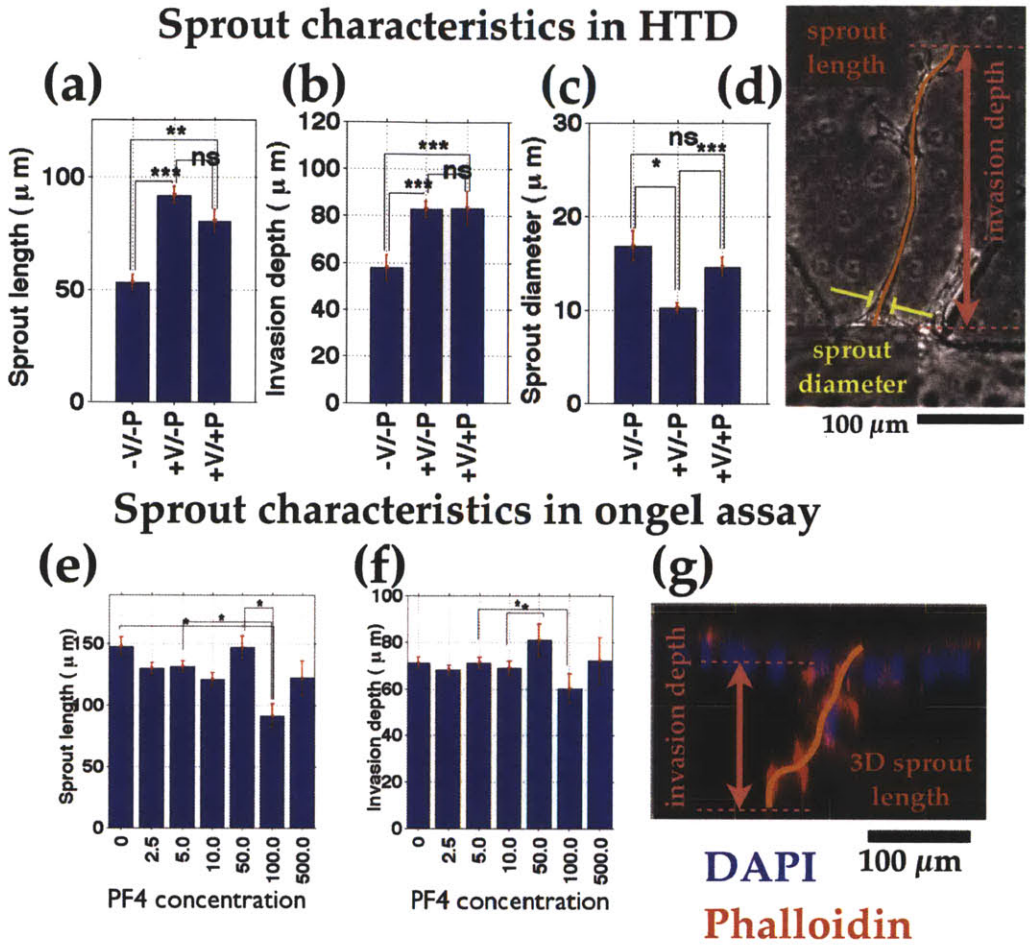

Figure 2-5: (a-c) The effect of VEGF and PF4 on the average sprout length, average invasion depth, and average sprout diameter of hMVECs at 72 hours after treatment in microfluidic devices. (Statistically significant difference are denoted as follow: $***-p \leq 0.005$; $*-p \leq 0.05$; ns - not significant, $p > 0.05$). (e-f) The effect of VEGF and PF4 on the average sprout length and invasion of hMVECs at 72 hours after treatment in ongel assay (Only statistically significant different among cytokines are plotted). (d and g) Sprout length is measured along the trunk of an angiogenic sprout from the tip to the point at the gel interface to which the sprout attached to the endothelial monolayer. Sprout diameter is measured as the diameter of the sprout lumen at the gel interface to which the sprout attached to the monolayer. Invasion depth represents the distance in direction perpendicular to the monolayer from the monolayer to the tip of the sprout.

disintegrate, the fractional area coverage and the number of cord branch point decrease. On the other hand, the number of end points increases as dissociation of endothelial cord results in new ends. These metrics were quantified from from phase

contrast images of endothelial cord over time. Quantification reveals that, compared to the no PF4 control (0 ng/mL PF4, 75 ng/mL VEGF), physiological level of PF4 (400 ng/mL PF4, 75 ng/mL VEGF) causes a more rapid reduction in fractional area coverage and in branch point density, and more rapid increase in the end point density (Figure 2-7). These results together suggest that PF4 accelerates endothelial cord dissociation.

2.4.3 PF4 reverses VEGF-mediated changes in cell orientation and in cell-cell adhesion

PF4's effect in accelerating cord dissociation leads us to hypothesize that PF4 may counteract VEGF's effect by modulating cell-cell adhesion and cell-ECM interactions. In endothelial cell population, cell-cell adhesion occurs through the homotypic interactions of vascular endothelial cadherin (VE-cadherin). VEGF has been shown to disrupt cell-cell adhesion by interfering with VE-cadherin's homotypic binding. Mechanistically, VEGF can signal through VEGF receptor 2 (VEGFR2) which in turn initiates the signaling cascade that leads eventually to VE-cadherin phosphorylation and conformational change. Inhibition of VE-cadherin by anti-VE-cadherin antibody or the knockdown of *CDH5* (gene encoding VE-cadherin) suppresses sprouting in an organotypic angiogenesis assay and during embryonic development in zebrafish [2].

To test whether PF4 can modulate VE-cadherin mediated cell-cell adhesion, we examine the VE-cadherin expression in hMVECs on type I collagen gel under VEGF and PF4 dosages. At the same bulk concentrations of VEGF and PF4 as in the sprouting assay, 72 hour treatments with VEGF and PF4 cause changes in VE-cadherin band thickness as observed in the confocal images. Quantitative analysis of the immunofluorescent staining of VE-cadherin band reveals that VEGF treatments leads to dose-dependent reduction in VE-cadherin band thickness and an approximately two-fold reduction at the highest tested concentration (80 ng/mL VEGF, Figure 2-

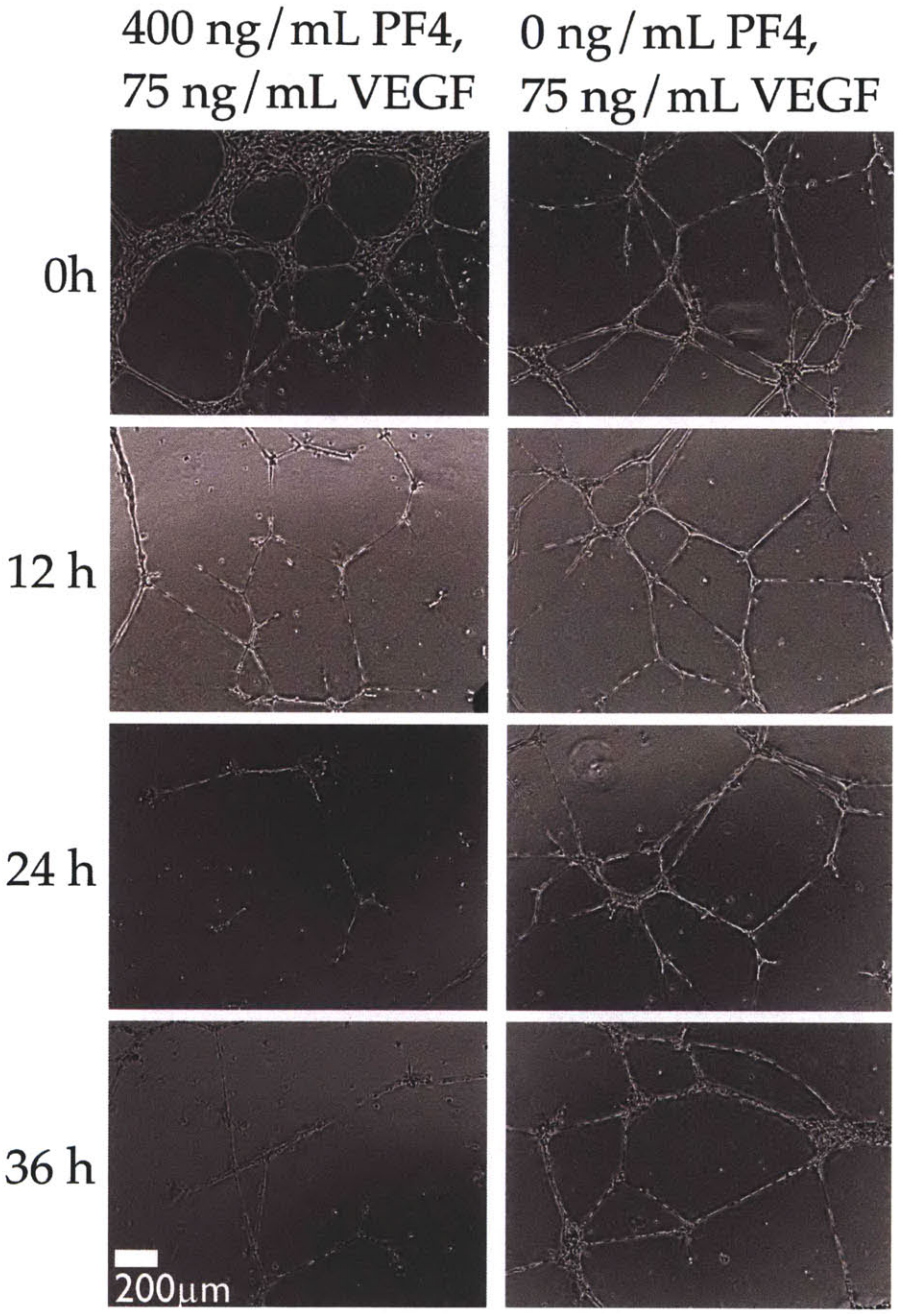

Figure 2-6: Representative phase contrast images of hMVEC on Matrigel under the NO PF4 vs physiological PF4 conditions. In the absence of PF4, VEGF prevents endothelial cord dissociation over 36 hours. PF4 accelerates the cord dissociation observed as reduction in endothelial cord density and cord branching over time.

8). On the contrary, PF4 treatment in the presence of low concentration of VEGF (20 ng/mL) dose-dependently reverses the effect.

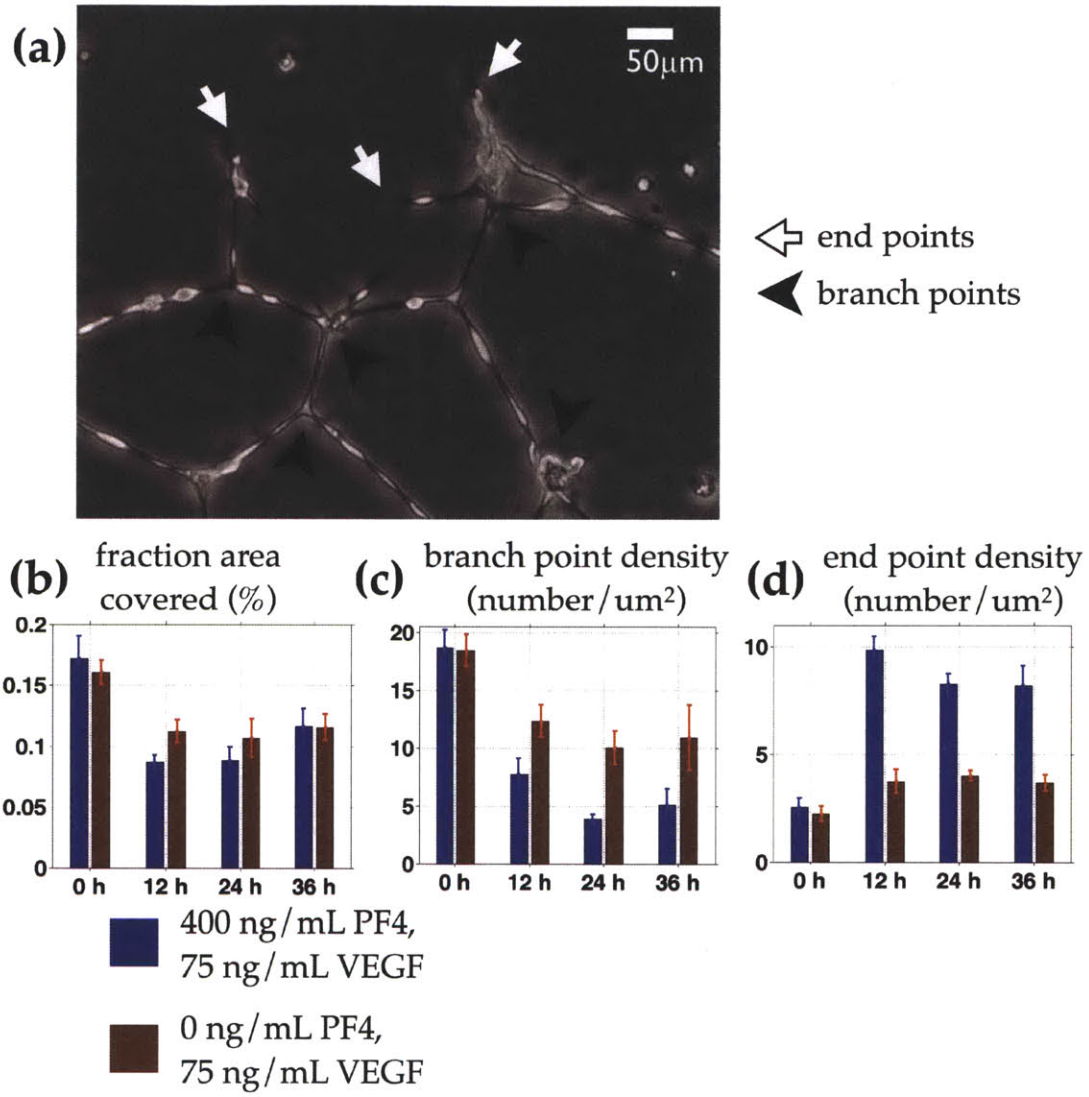

Figure 2-7: Platelet factor 4 reverses VEGF-mediated deceleration of endothelial cord dissociation. (a) High resolution image of the endothelial cord showing distinction between the endothelial cord branch point vs. end points. (b) Quantified fractional area coverage by the endothelial cord (ratio between cord area vs. total image area) (c) Quantified branch point density and (d) end point density.

In addition, VEGF and PF4 treatments lead to opposing dose-dependent changes in cell-shape (Figure 2-9). At the same VEGF and PF4 concentrations as in the sprouting assay, increasing VEGF dosage is correlated with more elongated cell shape detected at 72 hours of treatment. On the contrary, PF4 dosage in the presence of low concentration of VEGF (20 ng/mL) is associated with more squamous and rounded

cell shape.

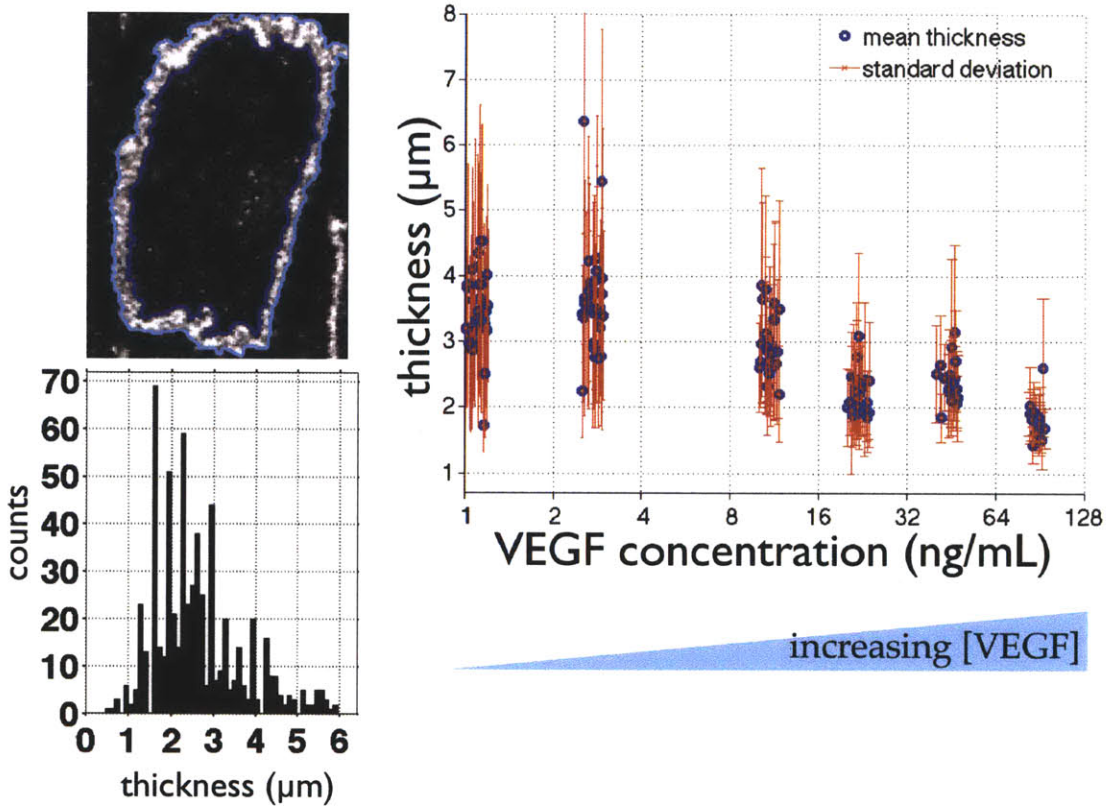

Figure 2-8: VEGF and PF4 treatments are associated with opposing changes in VE-cadherin band thickness at the cell-cell junctions. (a) Quantification of the VE-cadherin band thickness of a representative cell based on contour tracking. The outer and inner contours were represented by two hundred control points. The VE-cadherin band thickness are computed as the perpendicular distance between the two contours at the aligned control point coordinates. (b) VE-cadherin band thickness distribution for a representative cell in (a). (c)VEGF treatments correlates with a dose dependent reduction in VE-cadherin band thickness in hMVECs.

2.4.4 Two classes of PF4's potential mechanisms in reversing VEGF-mediated endothelial cell behavior

The results so far support the hypothesis that PF4 reverses VEGF-mediated changes in endothelial cell phenotypes in angiogenic sprouting and cell-cell adhesion. Several molecular mechanisms have been proposed to explain PF4's effects on angiogenic

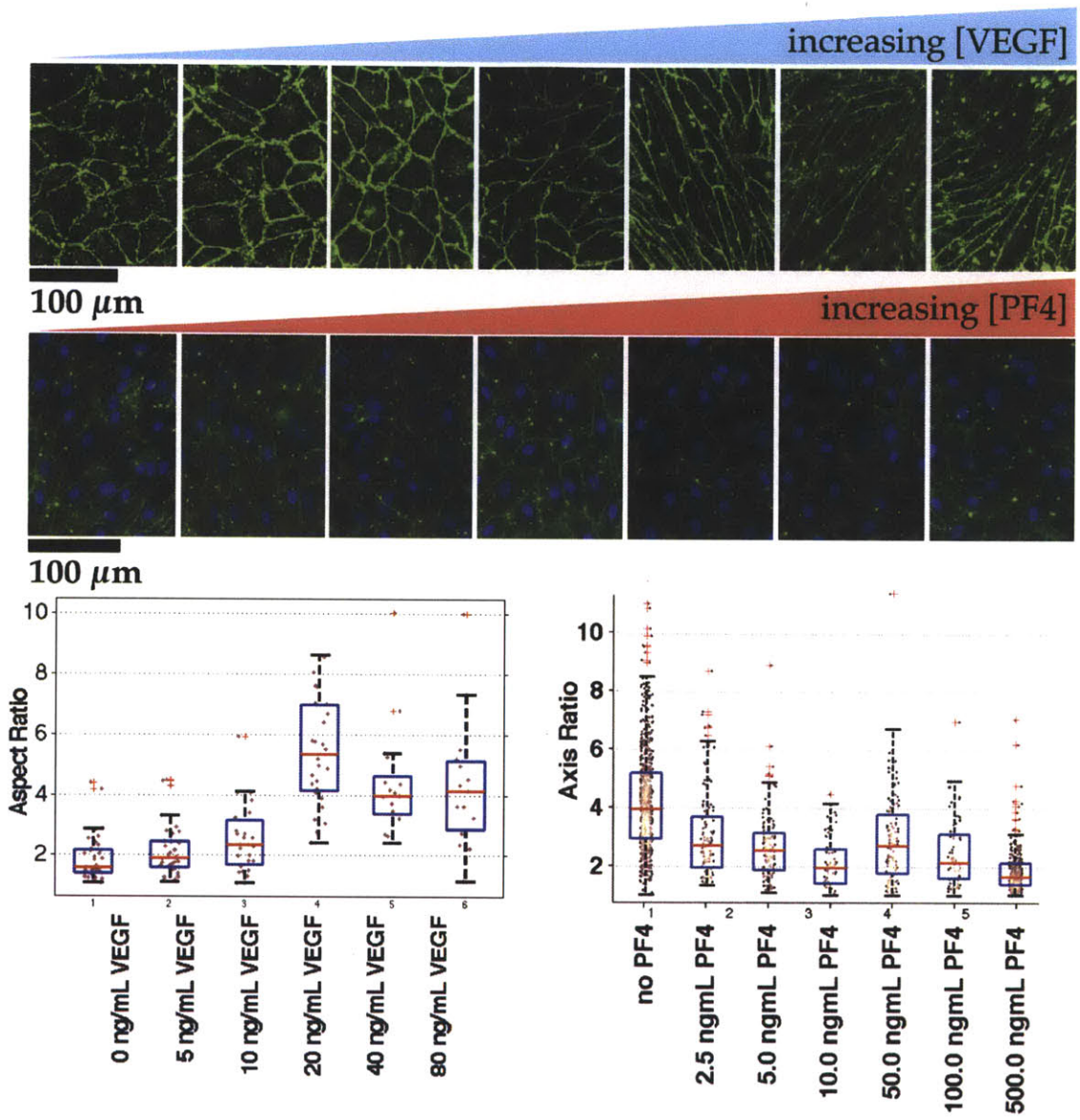

Figure 2-9: Platelet factor 4 reverses VEGF-mediated change in cell shape and cell-cell adhesion formation. hMVECs seeded at instant monolayer density (50,000 cells/cm^2) form confluent monolayer on collagen I gel. Treatments of cells with physiological concentrations of VEGF and PF4 modulates the cell morphology and VE-cadherin mediated cell-cell junctions.

endothelial cells. They can be largely classified into two major types: 1. Heparan sulphate proteoglycan (HSPG)-mediated non-signaling mechanism and 2. CXCR3B receptor mediated signaling mechanism (Figure 2-11).

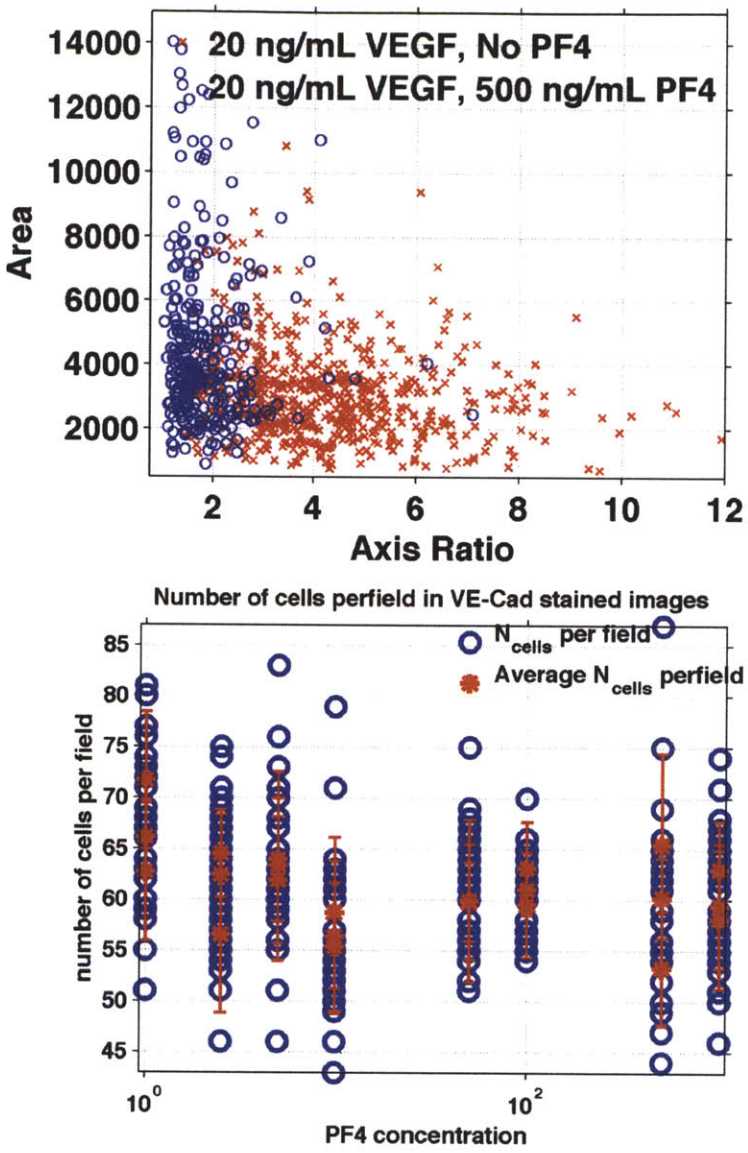

Figure 2-10: VEGF and PF4 changes are associated with changes in cell area and shape. (a) Cell area vs. axis ratio of hMVECs on Type I collagen gel after 72 hour treatment with 20 ng/mL VEGF alone (red x's) or with addition of 500 ng/mL PF4 (blue circles). VEGF treated hMVECs are elongated. With PF4 treatment, hMVECs adopt a more rounded morphology and some of the cells spread out more as seen by the increase in cell area. (b) Quantified changes in numbers of cells within an imaging frame as a measure of cell densities under 72 hour dosage treatment with PF4 in the background of 20 ng/mL VEGF. Number of cell in each of 12-16 image frames taken from each of the three experimental triplicate samples were shown as blue circles. The mean and standard error within each of the three triplicates are shown as red asterisks and red error bars respectively.

- **HSPG mediated extracellular mechanism**

  PF4 binds with high affinity and avidity to several types of glycans including HSPGs and chondroitin sulfate proteoglycans (CSPGs) [67]. *In vitro* studies have shown that HSPGs are also implicated in the angiostatic capacity of PF4. The evidence from *in vivo* studies, however, seem to indicate a contrary role of HSPG in PF4's angiostatic effect. Maione *et al* and others reported that modified recombinant PF-4 variants that have lost their HSPG binding domains exhibit even stronger angiostatic effect [69, 106].

  Given PF4's high affinity and avidity to cell surface proteoglycans, it can outcompete VEGF for glycan binding. The potential effects of PF4 occupancy on these glycans are two folds. First, PF4 occupancy excludes glycan molecules from capturing soluble VEGFs. HSPG have been reported to be an important mediator of VEGF-VEGR2 interactions. Second, PF4 occupancy excludes glycan molecules from binding fibronectin (FN). HSPG has been shown to be essential for conformational change of FN from a closed non-VEGF binding to an open VEGF binding conformation [73, 74]. Both of these effects can lead to an overall reduction in VEGFR2 binding and activation. Since the HSPG mediated mechanism occurs upstream of VEGF receptor activation and phosphorylation, we also refer to it as *'extracellular mechanism.'*

- **CXCR3 mediated intracellular signaling mechanism**

  Recent studies have discovered a new variant of CXCR3 receptors [60] known as CXCR3B. Several lines of evidence suggest that this newly identified receptor variant play an important role in mediating the angiostatic effect of PF4. Compared to the more prevalent *'A'* variant, CXCR3B binds preferentially to PF4. More importantly, CXCR3B is selectively expressed on the surface of angiogenic endothelial cells especially in microvessels [40, 57]. Molecular studies in CXCR3B signaling in non-endothelial cell lines have shed some light on the

the signal transduction pathways downstream of CXCR3B. For instant, recent studies in the effect of modulating CXCR3 in renal cancer cells indicates that CXCR3B can modulate the levels of the anti-apoptotic heme oxygenase-1 protein, leading to the better prognosis of the cancer [31]. However, the molecular details of CXCR3B signaling leading to its angiostatic effect of PF4 remains largely unknown. We refer to the effect of PF4 through CXCR3B as *'intracellular signaling mechanism.'*

2.4.5 Experimental methods to perturb the two mechanisms of PF4

Based on the current understanding of PF4, we hypothesize that both the *'extracellular'* HSPG-mediated and the *'intracellular'* CXCR3B-mediated mechanisms contribute to the observed angiostatic effect of PF4. To quantify the partial contributions, we dedicate the following section for discussing the methods to perturb the two mechanisms.

- **Inhibition of HSPG mediated mechanism**

  HSPG synthesis can be blocked by non-specific Sodium Chlorate treatment, Heparinase treatment, and inhibition of Ext-1/Ext-2 gene expression by shRNA. In the context of this thesis, preliminary treatment of HUVECs with Hep III does not significantly affect cell viability. Further experiments need to be conducted in order to quantitatively determine the effect of HSPG depletion on the angiostatic capacity of PF4.

- **Inhibition of CXCR3B mediated mechanism**

  CXCR3B expression can be inhibited by specific small molecular inhibitors, blocking antibodies, siRNAs, shRNAs, and targeted knockdown using site-specific Zn-finger nuclease. Commercially available siRNA pool was used to knock down the expression CXCR3B receptors in the cells. In the context of this thesis, further experiments need to be conducted to quantify the effect of

CXCR3B receptor depletion on the angiostatic effect of PF4.

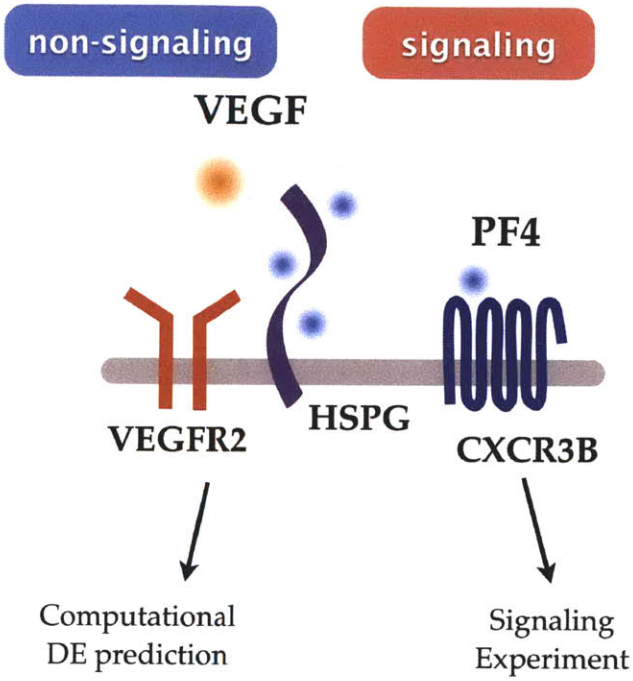

Figure 2-11: Potential mechanisms of PF4 on VEGF-mediated endothelial cell biology. PF4 can modulate VEGF-mediated endothelial cell behavior through two main classes of mechanisms. (1) Non-signaling HSPG mediated mechanism. PF4 binds to HSPG and precludes VEGF from adhering to HSPG and fibronectin. This effect causes a significant reduction in local effective concentration of VEGF around VEGF receptor 2 on the cell surface. (2) Signaling CXCR3 mediated mechanism. PF4 binds specifically to CXCR3B, a G-protein couple receptor variant specific to PF4 that is expressed exclusively on endothelial cell types. PF4 mediated activation of CXCR3B trigger intracellular signaling that can cross talk to VEGFR2 mediated signaling. CXCR3B activation by PF4 has been reported to activate p38 MAPK.

2.4.6 HUVECs and hMVECs express high level of VEGFR2 and CXCR3

In order to address the signaling mechanism of PF4 on VEGF signaling, we visualized the relative level of CXCR3B and VEGF receptors in the endothelial monolayer and the angiogenic sprouts. Immunofluorescent staining of HUVECs and hMVECs on absorbed collagen coated glass slide reveals that both cell types express comparably

high level of CXCR3 receptors compared to the unstained control (Figure 2-12a). Flow cytometry measurements of cells co-stained for VEGF receptor 2 and CXCR3 receptor confirms the presence of both receptor types in HUVECs and hMVECs (Figure 2-12b). To visualize the localization of the two receptor types in monolayer and angiogenic sprouts, hMVECs were cultured in HTD and allowed to form angiogenic sprouts. The HTD were refreshed with cell culture medium every 24 hours after seeding and fixed after 72 hours. Immunofluorescent staining against VEGF receptor 2 and CXCR3 receptor of these samples reveals that both receptor types are present in the monolayer and in the angiogenic sprout. High resolution confocal images of the samples show that the two receptors are distinctly localize on the membrane of hMVECs both in the monolayer and in the angiogenic sprouts.

2.5 Discussion:

Platelets store and release their cargos in thematic way – supporting angiogenesis in one circumstance by releasing pro-angiogenic cytokines or suppressing angiogenesis by releasing anti-angiogenic cytokines in another. Italiano *et al* reported that platelet stored angiogenic and angiostatic cytokines in separate subsets of α granules [51]. Ma *et al* and Chatterjee *et al* found that platelets selectively release pro-angiogenic and angiostatic upon activation of distinct receptor mediated signaling pathways [68, 23]). The two lines of evidence together support a hypothesis that platelets can serve as a *'contextually adaptive'* delivery device, by being selective of the subsets of α-granules, or of the timing of the granules to be released or both. High resolution imaging of the platelets cargo and detailed co-localization studies by Kamykowski *et al*; however, indicates that the cytokine release of platelets are considerably variable and less thematic [54]. Colocalization analyses in their study reveal that cargo distribution follows a Gaussian distribution that implies random cargo sorting into α-granules. Suggesting that platelet may achieved selective delivery of cytokines by differential timing of release.

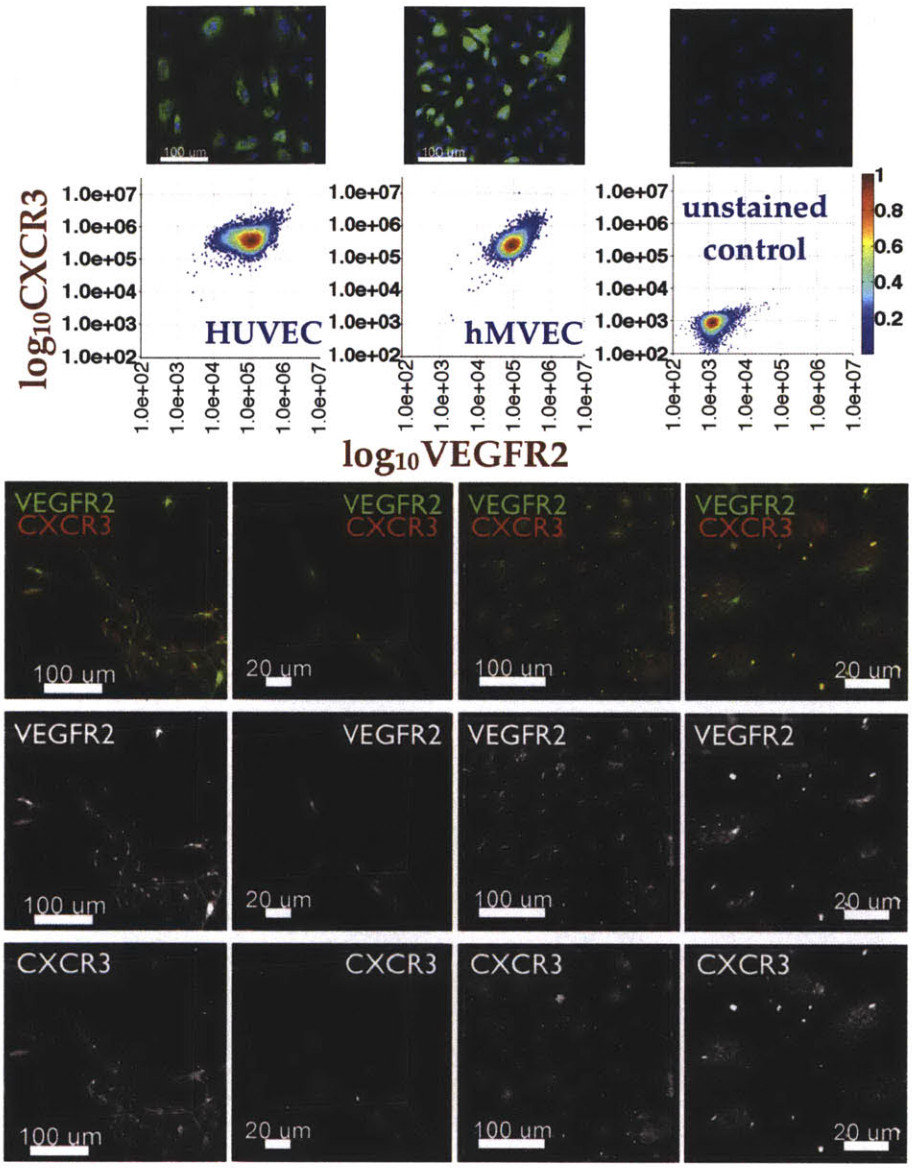

Figure 2-12: High levels of VEGFR2 and CXCR3 are detected in both HUVECs and hMVECs as determined by immunofluorescent (IF) staining and flow cytometry. Immunofluorescent staining of cells in microfluidic devices reveals the two receptors are co-expressed in angiogenic sprouts as well as in an endothelial monolayer. Since VEGFR2 and CXCR3 are specific to the potent angiogenic VEGF and angiostatic PF4 respectively, their presence on the highly angiogenic primary endothelial cells suggest that the two factors can counteract and jointly determines angiogenic outcomes inflammatory angiogenesis.

In this chapter, we show that angiogenic sprouting decision can occur at the level of endothelial cells in response to the co-release of angiogenic and angiostatic cytokines VEGF and PF4. The highly angiogenic endothelial cell types HUVECs and

hMVECs express the receptors for both the these platelet cytokines. We show that the angiogenic response of hMVECs to PF4 exhibits a switch like response with the narrow transition concentration range lying between the two ends of physiological concentrations – one detected during inflammation and the other in the absence of inflammation. In addition, PF4 reverses VEGF-mediated endothelial phenotypes including Matrigel tube formation, cell-cell junction formation, and cell shape. These lines of evidence suggest that the multitude of PF4 effects may be directly to oppose the role of VEGF in endothelial cell behaviors.

PF4 has previously been reported to exhibit anti-angiogenic properties through potential two main mechanisms. The quantitative contributions of these mechanisms has not been determined. Only recently has the CXC3B receptor – the only defined receptor for all ELR-negative CXC chemokines – been shown to be preferentially expressed on endothelial cells [89, 91]. We show that that hMVECs and HUVECs express high levels of CXCR3 and correspondingly response to the angiostatic effect of PF4, suggesting that the *intracellular signaling* mechanism has some contribution to the PF4's angiostatic effect. We propose a quantitative framework and experimental perturbations that need to be done to parse the contribution of PF4 effect through the two mechanisms. Further characterization of the signaling mechanism mediated by CXCR3B and the regulation of CXCR3 expression may provide another method by which the regulation of angiogenesis can be controlled in therapeutic settings.

2.6 Supplementary Figures

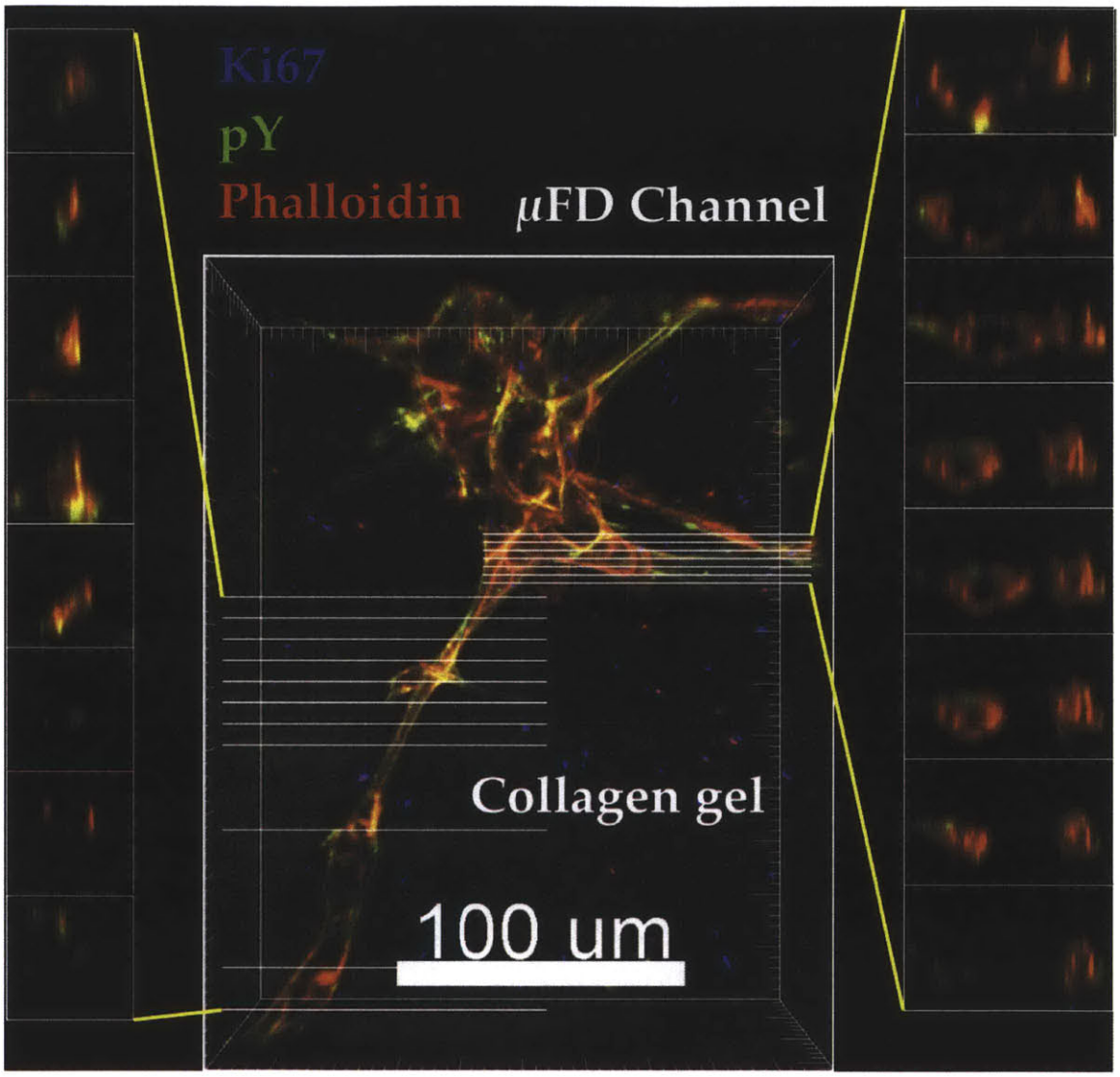

Supplementary Figure 1: Three-dimensional confocal images of continuous class 1 sprouts with lumens. hMVEC formed angiogenic sprouts in 3D collagen gel in HTD imaged at 72 hours after seeding. Cross sectional images showing continuous lumens from the base of sprouts (top side) to the tips (bottom side).

Chapter 3

Studying single cell decision in angiogenic endothelial cell population

3.1 Summary

Angiogenesis, the formation of new vascular networks from an existing vessel, is a multi-step process that requires fine regulation of multiple cellular response states including proliferation, migration and apoptosis. In order to coordinate successful angiogesis, endothelial cells switch their cellular states in response to environmental cues to maintain viability. Understanding the transition dynamics of cellular state transitions not only gives insight into the underlying process but also offers a means to make predictions of phenotypic outcome over time by numerical simulations. We hypothesize that the angiogenic vascular network formation is achieved as a result of a series of cell-level decisions in response to the infusion of growth factors. The challenge is to explain how a specific vascular network pattern emerges from individual agent behaviors. Currently, there is a substantial gap between individual cell-level behaviors and pattern formation as an aggregate effect of cell population behaviors. Agent based model is an important tool in bridging this gap. The model treats indi-

vidual cell as a decision making entity (*'agent'*) and encodes the single cell behaviors as *'rules'*. The model then simulates the tissue level responses arising from the collective results of single cell decisions. The reliability of this modeling approach depends crucially on the experimental validation of the model parameters. In this chapter, I present the development of an experimental methods for acquiring quantitative data and computational algorithms from inferring cell-decision parameters based on the two types of experiments. The first is the time-lapse aggregate population statistics acquired from multidimensional flow cytometry. The second is the individual cell state trajectories acquired by quantitative timelapse imaging. We formulate the parameter estimation algorithms based on the maximum likelihood estimation and the Bayesian inference of the posterior probabilities of transitions. These experimentally derived parameter values are novel and can be validated by stochastic simulations of endothelial cell populations with different initial conditions to experiments.

3.2 Introduction

3.2.1 Single cell decision as a stochastic process

Cellular phenotypes represent observable biological states among which cells adopt to accommodate to changing environmental cues. Transition patterns of cell from one phenotypic state to another have been reported to exhibit high degree of stochasticity [3, 86, 84, 62, 13]. In fact, stochastic decisions are ubiquitous in biology. From the genetic switch in the bacterial virus λ-phage in prokaryotic system to stem cell reprogramming in mammalian eukaryotic system, cells make stochastic switch in their behaviors [66]. Stochastic choices in cellular phenotypic response are advantageous for multiple reasons. In the case of single cell organisms such as bacteria and yeast, stochastic choices may allow for adaptive responses which confer evolutionary advantages in the face of changing environments. A strong evidence supporting this hypothesis is the existence of the persister state observed in many bacteria [13]. Multitude

of studies have shown that populations of bacterial cells containing subpopulations that enter non-growing or slow-growing state in which they can elude killings by most antibiotics. In the case of multi-cellular system, stochastic choices can create diverse gene expression patterns and genetic individuality which proved useful in sperm and egg productions and expansion of olfactory receptor repertoire. If these patterns are deterministically encoded, the amount of genetic material and machineries required to encode and decode this amount of information would be costly. In these cases, stochastic choices offer an advantage in economy of information storage.

Stochastic decisions are by definition non-random, but probabilistic. In modeling the multi-state stochastic decision processes, the key parameters are the phenotypic state transition rates. These parameters characterize the dynamics of cell decision within a population succinctly and enables the predictions pertaining to transition dynamics and steady-state distributions of the population. As such, the quantitative knowledge of transition probabilistic rates not only provides valuable insight to the underlying biological process and how they are influenced by external stimuli, but they also enable simulation and predictions of the population behaviors.

3.2.2 Types of data available for studying cell decision

Given the current state of the art experimental techniques in mammalian cell biology, there are two types of experimental data containing single cell decision information. The first type of data is the snapshot measurement of cell population at discrete time points. This types of data can be obtained by detecting single cell levels of phenotypic cellular state markers of a cell population at fixed time points such as in immunofluorescent staining (IF), or flow cytometry (FC). Since such measurements do not keep track of cell identities across time points, the resulting data only consists of aggregated head-counts of cells in the populations adopting different states. We refer to this type of data as *aggregate* data (Figure 3-1a). The second type of data is the time series measurements of cellular state markers by following individual cell over time. This

type of data can be obtained microscopically. Since the cell identities are recorded across time points in time series images, the resulting data is a full panel series of cellular states over time. We refer to this type of data as *full panel* data (Figure 3-1b).

The algorithms employed for parameter estimation depends on the types of data that can be experimentally obtained. We formulate methods for estimating the state transition rates under the aforementioned two types of observations. We rely on maximum likelihood estimation (MLE) and Bayesian inference (BI) for obtaining the parameters. Our decision to use both parameter estimation methods is motivated by multiple reasons. Maximum likelihood estimation selects the set of model parameters that yields the greatest likelihood of observing the data. Since the estimation does not rely on prior knowledge, MLE can be computed when prior knowledge regarding the parameter values is unavailable or unreliable. Moreover, MLE can be determined numerically even when the underlying probability model is complex or cannot be derived formally. On the contrary, Bayesian inference computes the degree of belief in the parameter values by combining both the evidence (the experimental data and the underlying probability model) with prior knowledge. Since BI infers parameter distributions rather than parameter values, it can capture the inherent inhomogeneity in the parameter values among the population members as distributions. Additionally, BI is equipped with a formal means to incorporate prior knowledge if available or derivable from the underlying biology.

3.3 Problem formulation

Consider a population of $\mathcal{N}$ cells undergoing single cell phenotypic transition. Each cell i adopts a phenotypic state $s_i(t) \in \mathcal{S}$ at time t. Let $\mathcal{U} = (s_0, t_0, s_1, t_1, ..., s_{k-1}, t_{k-1}, s_k)$ denotes the set of random variables describing a chain of single cell state trajectory up to time t. We start by a description of the temporal statistics of cell state transitions for the aggregate headcount data. We assume that cells transition in time from one

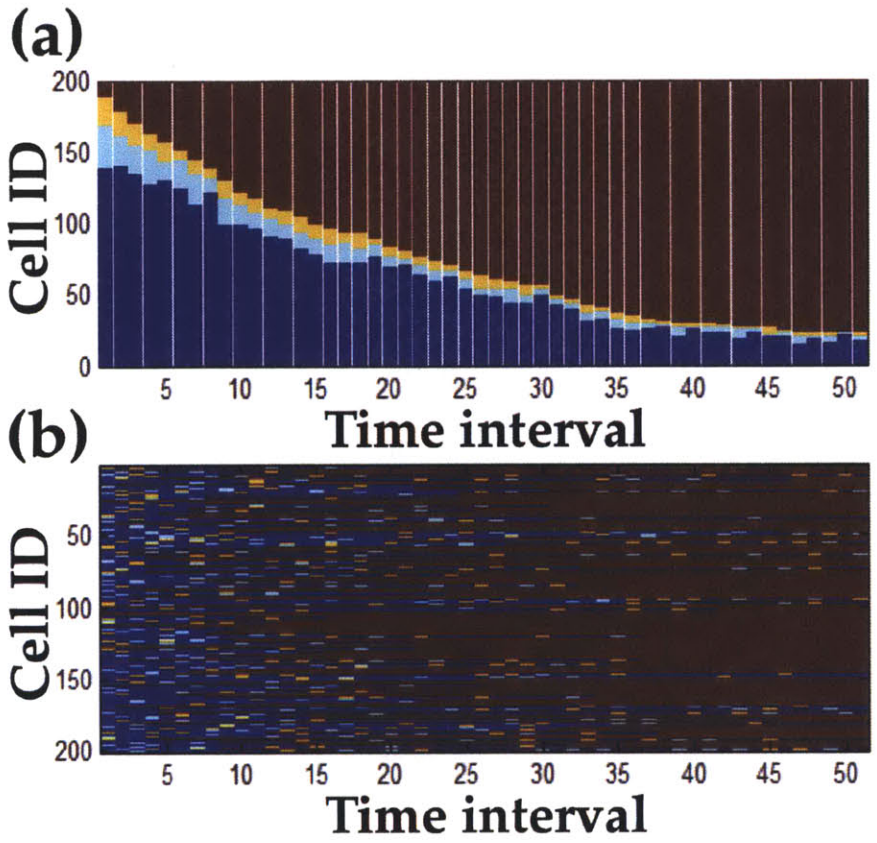

Figure 3-1: Two types of experimental data containing single cell decision information. (a) Longitudinal data is an aggregate counting of cells in different states, e.g. snap-shot measurement of population using flow cytometry. For this type of data, parameter inference is not straightforward and requires snapshot counting of large number of cells from population. (b) Full panel data contains individual cell state trajectories through time e.g. by live cell imaging. For this type of data, parameter inference is more straightforward and can be obtained by tracking of individual cells

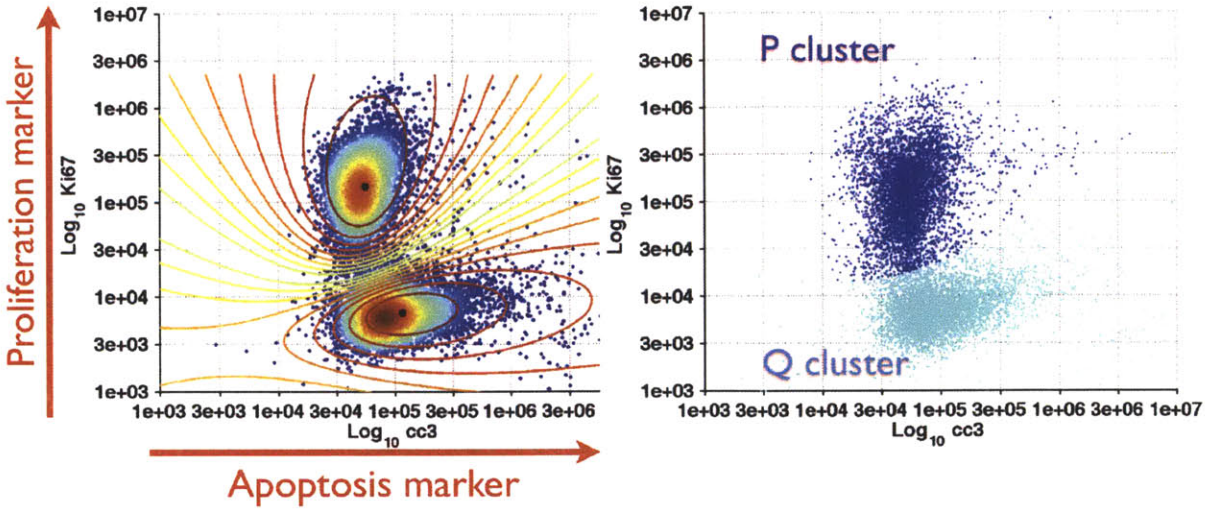

Figure 3-2: (a) State detection within one time point of a longitudinal dataset collected by measuring proliferative and apoptosis markers (Ki67 and cleaved caspase-3 respectively) by flow cytometry. Using Fuzzy clustering algorithms (in this case, the Gustason-Kessel clustering [1]) to define the mixture distribution, we consistently detect two phenotypic clusters from the flow cytometry data.

state to another according to a Poisson process, which is a common description of population transition times. The Poisson process assumption further implies that i) the number of transitions occurring within a particular time interval follows a Poisson distribution, and ii) the residence time of each cell as it visits a state follows an exponential distribution.

3.3.1 Problem 1 : parameter inference for aggregate head-count data

Measuring proliferation and apoptotic markers (Ki67 and cleaved caspase 3 respectively) within cell population by FC, we consistently detect two distinct subpopulations of cells (Figure 3-2) for at all time points measured. As proof-of-principle, we use the following treatments to drive the single cell decisions within the population: 1. starvation condition - in which case we expect the population to shift from proliferative (P) to sessile (S) and apoptotic (A) states; and 2. growth medium stimulation of a pre-starved population - in which case we expect the population to shift from

sessile to proliferative states. The single cell decision events we are interested in are the state transitions of from proliferative state (P) to sessile state (S) with probabilistic rate (λ_{PS}). To obtain the aggregate headcounts over time, we performed the FC measurements of cell population under these treatments at discrete time points (Figure 3-2).

3.3.2 Likelihood of one transition type can be modeled as Poisson arrival process

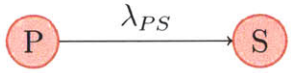

To model the state transition in the starvation experiment, we start with a simpler probability model with the following underlying assumptions:

- there is only one transition type
- the single cell decision Poisson process is homogeneous
- all cells are identical in transition dynamics

Poisson probability of one arrival

Given these assumptions, we employed the homogeneous *Poisson process* to describe the single cell decision (shown in the schematic diagram above). To construct an analytical expression for the likelihood function for MLE and BI, we first derive the probability of an occurrence of one cell. Let S_n be the state of the cell at time n and τ_n be the waiting time, then the probability of state transition occurring after an observed time τ according to the Poisson process is given by

$$
\begin{aligned}
P(S_{n+1} = j, \tau_{n+1} \geq \tau \quad &| \quad S_1, \ldots, S_n = i; \tau_1, \ldots, \tau_n) \\
&= P(S_{n+1} = j, \tau_{n+1} \geq \tau \mid S_n = i) \\
&= P(S_{n+1} = j \mid S_n = i) \cdot P(\tau_{n+1} \geq \tau | S_n = 1) \\
&= p_{ij} \cdot e^{-\nu_i \tau}.
\end{aligned}
$$

p_{ij} - transition probability ν_i - transition rate out of state i

$$
\begin{aligned}
P(1, \tau) &= p_{ij} \cdot e^{-\nu_i \tau} \\
&= p_{ij} \cdot e^{-\nu_{ij} \tau} \\
&= (\lambda \tau) \cdot e^{-\lambda \tau}.
\end{aligned}
$$

In the following section, we extend the Poisson probability function to account for multiple observed arrivals over an interval τ by treating multiple arrivals as independent events.

Poisson probability of more than one arrivals

It is of note that when FC runs are performed, only a fraction of cell population are taken for the measurements. As such, the FC results are representative samplings of the cell population in P, S states at certain observation time. We denote these samplings as fractions of cells in P and S states($\mathcal{F}_{\mathrm{P}}(t), \mathcal{F}_{\mathrm{S}}(t) respectively$). Given a relatively long doubling time of the human microvascular endothelial cells (hMVECs), it is reasonable to assume that the total number of cells ($\mathcal{N}_{tot}$) does not change over the course of the experiment. As such, the following relationship holds:

$$
f_i = f(t_i) = \frac{\mathcal{N}(t = t_i) - \mathcal{N}(t = 0)}{\mathcal{N}_{\mathrm{tot}}} = \mathcal{F}_S(t = t_i) - \mathcal{F}_S(t = 0) = \frac{k_i}{\mathcal{N}_{\mathrm{tot}}}.
$$

Given the above relationship, we can turn the likelihood function of Poisson arrival in terms of the number of observed transition (k_i) into a function the fractions $\mathcal{F}_{t=t_i}$

and $\mathcal{F}_{t=0}$, the quantities we obtain directly from the FC measurements. Here we propose two ways of formulating the probability of k arrivals.

1. **Joint probability of k arrivals as a product of the probabilities of k independent one arrivals**

   Taken the probability of one arrival in time interval [0, t] from the previous section ($(\int_0^t Poiss(1,\lambda,\tau)d\tau)$), the probability of k independent arrival can be written as the product of individual arrival, i.e.,

$$\begin{aligned} P(t_{\text{trans}} \leq t|\lambda) &= P(k=1,\lambda,t_{\text{trans}} \leq t) \\ &= \frac{\int_0^t P(\mathcal{N}(t+t_{\text{trans}})-\mathcal{N}(t)=1\ ;\ t_{\text{trans}}=\tau)d\tau}{\int_0^\infty P(\mathcal{N}(t+t_{\text{trans}})-\mathcal{N}(t)=1\ ;\ t_{\text{trans}}=\tau)d\tau} \\ &= \frac{\int_0^t \lambda\tau e^{-\lambda\tau}d\tau}{\int_0^\infty \lambda\tau e^{-\lambda\tau}d\tau} \\ &= \left(1-e^{-\lambda t}-\lambda t e^{-\lambda t}\right). \end{aligned}$$

   If k independent transitions are observed over the interval [0, t], the likelihood is given by

$$\begin{aligned} P(t_{\text{trans}}^{(1)} < t \cap \ldots \cap t_{\text{trans}}^{(k)} \leq t \mid \lambda) &= \frac{1}{k!}\cdot P(t_{\text{trans}}^{(1)} < t)\cdot\ldots\cdot P(t_{\text{trans}}^{(k)} < t) \\ &= \frac{1}{k!}\big(P(t_{\text{trans}} < t|\lambda)\big)^k \\ &= \frac{1}{k!}\left(1-e^{-\lambda t}-\lambda t e^{-\lambda t}\right)^k. \end{aligned}$$

2. **Joint probabilities of k arrivals as described by the k Poisson arrivals**

   The probability of k arrivals for a given time t can alternatively be described using the k-arrival Poisson process ($(Poiss(k,\lambda,t))$) at certain amount of time t. Then, the probability of k arrivals in the interval [0, t] is given by the integral

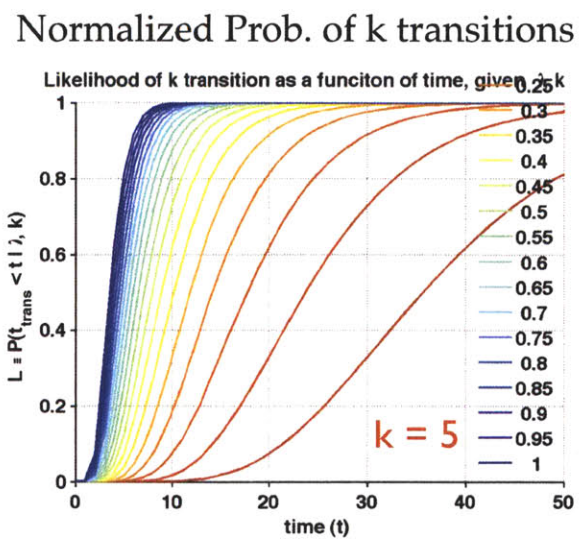

Figure 3-3: Predicted probabilities at varying transition rate parameter (λ_{PS}) of five transitions occurring within the population during the time interval τ between two consecutive FC measurements. For each value of transition rate, the transition curve exhibits a sigmoidal shape consisting of transition lag and parameter range over which rapid transition occurs similar to that observed in the FC data.

over the time period ($\int_0^t Poiss(k, \lambda, \tau) d\tau$) i.e.,

$$\begin{aligned} P(k > 1, \lambda, t) &= \frac{(\lambda t)^k}{k!} e^{-\lambda t} \\ P(t_{\mathrm{trans}}^{(1,\ldots,k)} \leq t \mid \lambda) &= \int_0^t \frac{(\lambda\tau)^k}{k!} e^{-\lambda\tau} d\tau \Big/ \int_0^\infty \frac{(\lambda\tau)^k}{k!} e^{-\lambda\tau} d\tau \\ &= \frac{\mathbf{\Gamma}(\frac{t}{\lambda}, k+1)}{\mathbf{\Gamma}(k+1)}. \end{aligned}$$

where $\mathbf{\Gamma}(\frac{t}{\lambda}, k+1)$ is an incomplete Gamma function.

Note that the predicted likelihood calculated with the first and the second methods yield slightly different expressions. We numerically assert that the two methods are equally valid as the produce same predictions in the domain of all admissible parameter values (λ, t, k).

3.3.3 Parameter estimation formulations

Given the likelihood function derived in the previous section, we can now formulate the parameter estimate based on MLE and BI.

Maximum Likelihood Estimation (MLE)

For the one step transition with single path model, the only parameter in the model is the transition rate λ_{PS}. The likelihood function given the aggregate headcount data is just the joint probability function conditioned on the observed transition k_i derived from the FC measurements. For the PS transitions, the log likelihood function of the transition parameter λ_{PS} is given by

$$
\begin{aligned}
\mathcal{L}(\lambda|\{k_i,t_i\}) &= \log\Bigg(\prod_{i=1}^{\mathcal{N}}\Big(P(t_{\mathrm{trans}}^{(k_i)} < t_i|\lambda)\Big)\Bigg) \qquad k_i \geq 0, t_i > 0, \forall i \\
\mathcal{L}(\lambda) &= \sum_{i=1}^{\mathcal{N}}\log\Bigg(\frac{1}{k_i!}\Big(P(t_{\mathrm{trans}} < t_i|\lambda)\Big)^{k_i}\Bigg) \\
\mathcal{L}(\lambda) &= \sum_{i=1}^{\mathcal{N}} k_i\log\Bigg(\frac{1}{\lambda}\big(1-e^{-\lambda t_i}-\lambda t_i e^{-\lambda t_i}\big)\Bigg) \\
\mathcal{L}(\lambda) &= \mathcal{N}_{\mathrm{tot}}\sum_{i=1}^{\mathcal{N}} f_i\log\Bigg(\frac{1}{\lambda}\big(1-e^{-\lambda t_i}-\lambda t_i e^{-\lambda t_i}\big)\Bigg), \qquad \text{where} \\
\lambda^{\mathrm{MLE}} &= \underset{\lambda}{\mathrm{argmax}}(\mathcal{L}(\lambda))
\end{aligned}
$$

Here, it is worth noting that the number of transitions from i^{th} observation (k_i) is a positive linear coefficient inside the sum in the log likelihood function. By replacing the derived variable k_i with the experimentally measured f_i, we merely scale the likelihood function by a positive integer $\mathcal{N}_{\mathrm{tot}} > 0$ without affecting its shape. As such we can directly evaluate and optimize the resulting likelihood using the experimentally observed (f_i, t_i).

We apply the MLE formula to compute parameter estimates from the FC measurements of hMVECs under starvation and refreshment experiments. With the one

transition type assumption, we show that the Poisson likelihood estimate the FC measured fraction of cells in S and P state reasonably well (Figure 3-4).

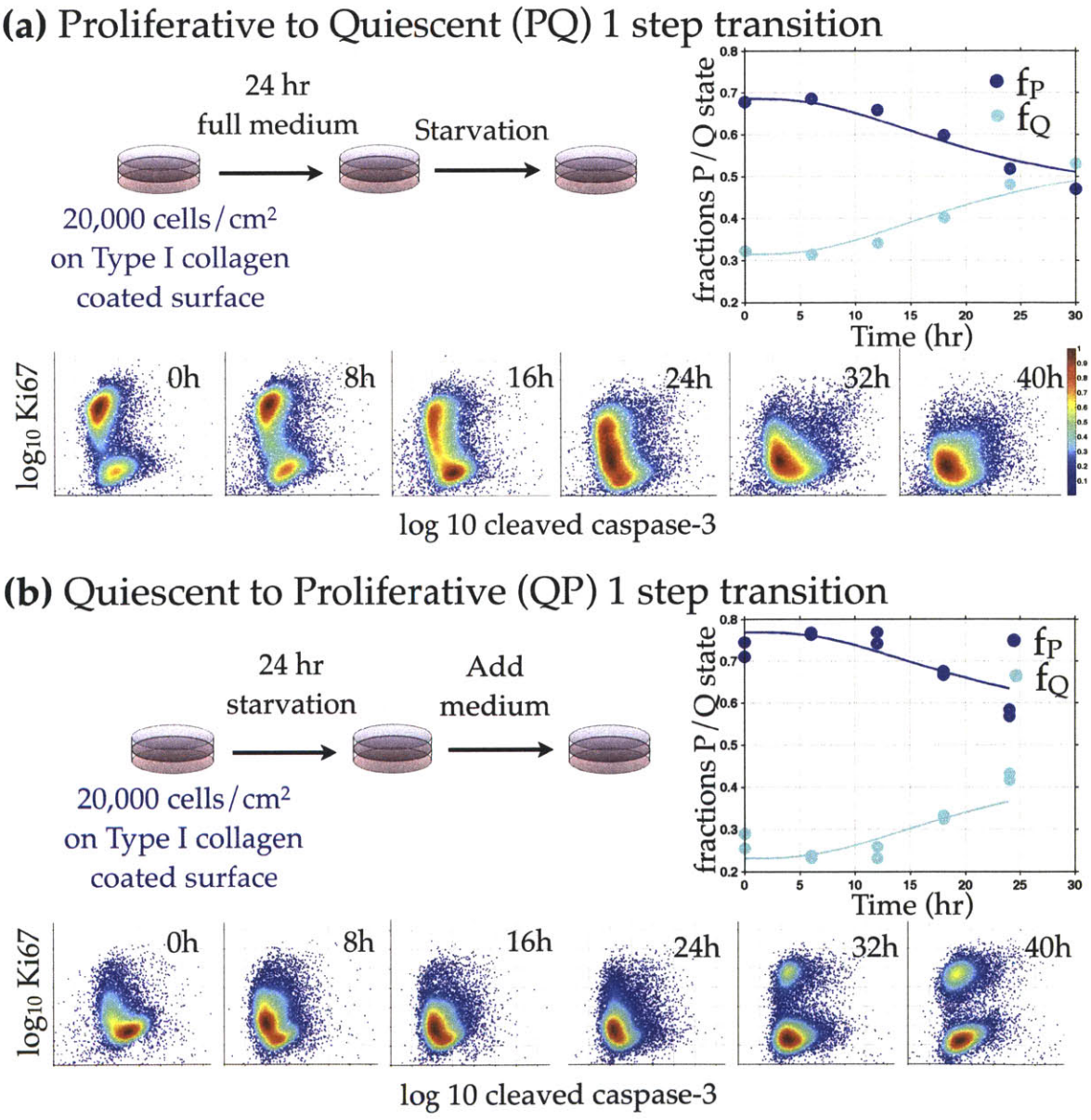

Figure 3-4: (a) Expression of proliferative and apoptotic markers of hMVECs under the serum starvation (a) and serum addition treatments (b).

Bayesian inference

Given the likelihood function and the FC measurements at two successive time points $(f_i, t_i; f_{i+1}, t_{i+1})$, we can easily compute k_i. To estimate the probability distribution of the transition parameters by the Bayesian approach, we write the Bayes' rule in terms of these variables:

$$P(\lambda|\{k_i\},\{t_i\}) = \frac{\overbrace{\prod_{i=1}^{\mathcal{N}} P(k_i,t_i|\lambda)}^{\text{likelihood}} \cdot \overbrace{P(\lambda)}^{\text{prior}}}{\underbrace{\prod_{i=1}^{\mathcal{N}} P(k_i,t_i)}_{\text{evidence}}}$$

In Bayesian analysis, the prior distribution $P(\lambda)$ is either given or assumed based on biological (prior) knowledge of the parameter. When such information is not available or unreliable, we may consider the following priors:

1. **Conjugate prior**

   Conjugate prior is the prior distribution of the same family as the posterior distribution. Using conjugate priors in Bayesian analysis is mathematically convenient as the posterior distribution can often be expressed analytically. Consider a general problem of inferring the parameter distribution, the posterior distribution can be express as the product of the likelihood and the prior distributions, i.e.,

   $$p(\lambda|x) = \frac{P(x|\lambda)\cdot P(\lambda)}{\int_\lambda P(x|\lambda)\cdot P(\lambda)d\lambda},$$

   where x denotes observations.

   Using conjugate priors, we demonstrate that we can obtain the posterior distribution of the parameters for the Poisson transition with a single parameter transition problem and the dual transition problems (Figure 3-5).

2. **Non-informative prior**

When conjugate priors yield improper posterior distributions, we consider alternative priors that does not require prior knowledge about the parameter values. As the name suggest, non-informative prior is appropriate choice when no prior belief is available or when one does not wish to influence the analysis with the prior. The problem with non-informative priors are that the it may be uniform in one scale, but might take a different shape and information upon parameter transformation. To avoid this problem, we rely on Jeffreys prior to make sure that the statement of non-informative prior belief is transformation-invariant.

Jeffreys prior is among the most widely used non-informative prior in Bayesian analysis. It is defined as the expectation of Fisher information, a measure of the amount of information observations provide about unknown parameters of a probability distribution [5]. Fisher information is formally defined as:

$$I(\lambda) = \int_x \left(\frac{d}{d\lambda}\mathcal{L}(\lambda|x)\right)^2 p(x|\lambda)dx,$$

or alternatively,

$$I(\lambda) = \int_x \left(\frac{d^2}{d\lambda^2}\mathcal{L}(\lambda|x)\right) p(x|\lambda)dx,$$

where, x represents the set of parameters that define the probability distributions; $\mathcal{L}$ denotes the likelihood function of the parameter λ.

In the alternative form, Fisher information measures the expected curvature or acceleration in the log-likelihood function with respect to the parameter λ [55]. High curvature in log-likelihood surface indicates that the observations x provide much information about the parameter λ. For the aggregate data parameter estimation problem at hand, $x = \{k_i, t_i\}$ is the set of the observed

transitions the and intervals between aggregate data acquisition.

For single parameter problems, Jeffreys prior is proportional to the square root of the determinant of the Fisher information, i.e.,

$$P(\lambda) \propto \sqrt{I(\lambda)} \quad .$$

Given the likelihood function we derive in the previous section, we can write the Fisher information and Jeffrey prior in term of the observation parameters $\{k_i, t_i\}$ as:

$$\begin{aligned} I(\lambda) &= \sum_{k_i} \int_{t_i} \left(\frac{d}{d\lambda} \mathcal{L}(\lambda | \{k_i, t_i\}) \right)^2 p(\lambda | k_i, t_i) d_{t_i}, \\ \text{and} & \\ P(\lambda) &= \left(\sum_{k_i} \int_{t_i} \left(\frac{d}{d\lambda} \mathcal{L}(\lambda | \{k_i, t_i\}) \right)^2 p(\lambda | k_i, t_i) d_{t_i} \right)^{1/2}. \end{aligned}$$

3.4 Two state model with dual transitions

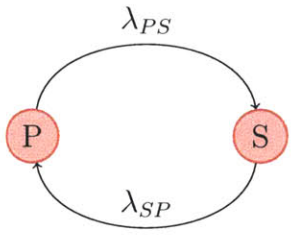

So far the previous analysis implicitly assume that all cell in the population go through only one transition type. The assumption is justified in the context where the transition is irriversible in cell fate determination and differentiation. In most cases of phenotypic transitions, however, cells with two accessible phenotypic states can transition between the two states both ways. Therefore, we extend the development of the previous section to explicitly account for the *'dual'* transition.

3.4.1 Model setup and parameters

First, recall the probability of Poisson likelihood of each type of transition is given by:

$$\begin{aligned} P(k_{\mathrm{PS}} = 1, \tau) &= \lambda_{\mathrm{PS}} \tau \cdot e^{-\lambda_{\mathrm{PS}} \tau} \\ P(k_{\mathrm{SP}} = 1, \tau) &= \lambda_{\mathrm{SP}} \tau \cdot e^{-\lambda_{\mathrm{SP}} \tau} \end{aligned}$$

As in the previous case, let $f_i^{(PS)}$ and $f_i^{(SP)}$ be the fraction of cells that undergoes PS and SP transition over the interval t_i respectively. These quantities are not measured directly from the flow cytometry experiments.

$$\mathcal{F}_S(t = t_i) - \mathcal{F}_S(t = 0) = f_i^{(\mathrm{PS})} - f_i^{(\mathrm{SP})}.$$

From the previous part, the probabilities of k_{PS} transitions are given by

$$\begin{aligned} P(t_{\mathrm{PS}}^{(1)} \leq t \cap \ldots \cap t_{\mathrm{PS}}^{(k_{\mathrm{PS}})} \leq t \mid \lambda_{\mathrm{PS}}) &= \frac{1}{k_{\mathrm{PS}}!} \left(1 - e^{-\lambda_{\mathrm{PS}} t} - \lambda_{\mathrm{PS}} t e^{-\lambda_{\mathrm{PS}} t}\right)^{k_{\mathrm{PS}}} \\ &= P(k_{\mathrm{PS}}, \lambda_{\mathrm{PS}}). \end{aligned}$$

$$\begin{aligned} P(k_{\mathrm{PS}}, k_{\mathrm{SP}}, \lambda_{\mathrm{PS}}, \lambda_{\mathrm{SP}}) &= P(k_{\mathrm{PS}}, \lambda_{\mathrm{PS}}) \cdot P(k_{\mathrm{SP}}, \lambda_{\mathrm{SP}}) \cdot P(k_{\mathrm{PS}}, k_{\mathrm{SP}}) \\ &= \frac{\left(1 - e^{-\lambda_{\mathrm{PS}} t} - \lambda_{\mathrm{PS}} t e^{-\lambda_{\mathrm{PS}} t}\right)^{k_{\mathrm{PS}}}}{k_{\mathrm{PS}}!} \times \frac{\left(1 - e^{-\lambda_{\mathrm{SP}} t} - \lambda_{\mathrm{SP}} t e^{-\lambda_{\mathrm{SP}} t}\right)^{k_{\mathrm{SP}}}}{k_{\mathrm{SP}}!} \\ &\quad \times \underbrace{P(k_{\mathrm{PS}}, k_{\mathrm{SP}}).}_{\text{by sampling methods}} \end{aligned}$$

In the above expression, there are two unobserved number of transitions (k_{PS}, k_{SP}) and two rate parameters (λ_{PS}, λ_{SP}). The joint probability $P(k_{\mathrm{PS}}, k_{\mathrm{SP}}, \lambda_{\mathrm{PQ}}, \lambda_{\mathrm{SP}})$ depends on $P(k_{\mathrm{PS}})$ which we neither know apriori nor wish to optimize. Instead, we would like to find the maximum likelihood estimate and the posterior probabilities of these rate parameters under all the admisable values of $(k_{\mathrm{PS}}, k_{\mathrm{SP}})$. To

get around this problem, we note that the two unobserved number of transitions (k's) are dependent and are bounded by the following constraints:

$$\begin{array}{ccccccc} & & \Delta\mathcal{F}_S\mathcal{N}_{tot} & \leq & k_{PS} & \leq & f_S & \leq & \mathcal{N}_{tot} \\ 0 & \leq & k_{SP} & \leq & k_{PS} - \Delta\mathcal{F}_S\mathcal{N}_{tot} & \leq & (1 - f_S). \end{array}$$

Since $f_S, \mathcal{N}_{tot}$, and $\Delta\mathcal{F}_S$ are measured or can be derived from the experimental measurements directly, these constraints are well defined for each experimental measurement and form a bounded domain.

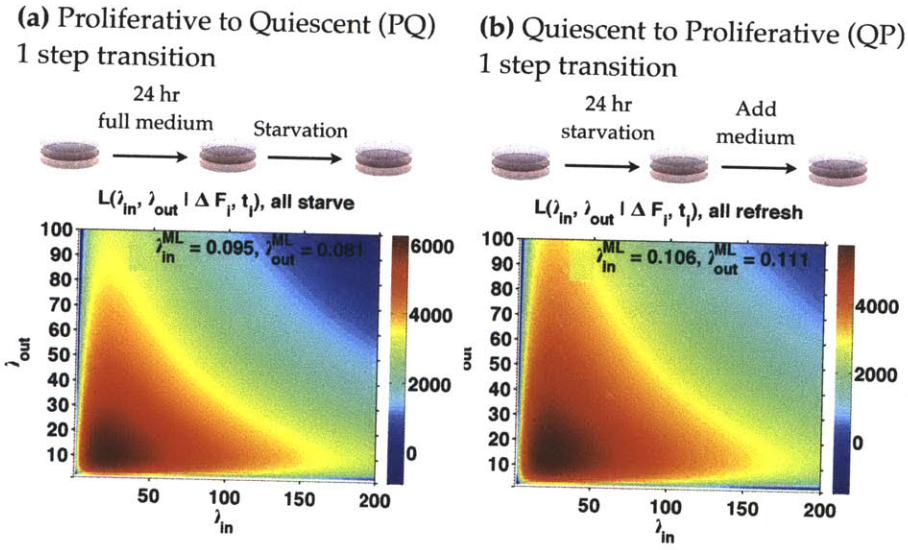

Figure 3-5: Bayesian inference of joint transition rate parameter distribution in dual transition problem using conjugate priors. (a) The posterior distributions in serum starvation experiment and (b) in serum addition experiment.

3.4.2 Problem 2 : parameter inference for full panel longitudinal data

As we discussed in the beginning of the chapter, there are two types of experimental data available for single cell phenotypic transition probability inference. When obser-

vations are made for every single agent at frequent time interval, the resulting dataset (full panel dataset) simplifies the parameter interference algorithm significantly since the likelihood function can be computed directly. In the next chapter, we will explain the experimental method for acquiring full panel data from live cell microscopy. Given the full panel data availability, we will discuss parameter inference in details.

3.5 Conclusion and discussion

In this chapter, we discuss the types of experimental from which single cell decision parameters can be extracted: 1. the aggregate measurements of phenotypic state markers across the population measured by FC and 2. the full panel data containing single cell trajectories over time. We derive the formulation for estimating transition rates between proliferative and quiescent states based on aggregate FC measurements of proliferation marker (Ki67) and apoptotic marker (cleaved caspase-3). For this dataset, we showed that we can use Poisson process to model the single cell decision. The derivation of likelihood function based on Poisson description leads to successful estimation of phenotypic transition rates based on MLE and BI. In the next chapter, we will discuss the parameter estimation based on the full panel data derived from microscopic imaging of endothelial cell population.

Chapter 4

Quantitative analysis of phenotypic transition in angiogenic endothelial cell from full panel data

4.1 Summary

Angiogenesis requires coordinated dynamic regulation of multiple phenotypic behaviors of endothelial cells in response to environmental cues. Multi-scale computational models of angiogenesis can be useful for analyzing effects of cell behaviors on the tissue level outcome, but few experimental studies have been dedicated to determining the required quantitative rules for cell-level phenotypic responses across a landscape of pro- and anti-angiogenic stimuli. Here we employ single-cell microscopy to ascertain phenotypic behaviors of more than 500 human microvascular endothelial cells distributed across 5 combinations of angiogenic (VEGF) and angiostatic (PF4) cytokine concentrations, analyzing their dynamic transitions among sessile, migratory, proliferative, and apoptotic states. We find that the cells exhibit an identifiable set of phenotypic state transition patterns consistent across all conditions, with the proportion of a population following a particular pattern being condition-dependent. VEGF strongly increases the population proportions in the proliferation-associated P clus-

ter along with migration and migration/sessile switching-associated M cluster and Sw cluster, at the expense of the sessile-associated S cluster and apoptosis-associated A cluster, as expected. PF4 does not affect the population proportions significantly by itself, but reverses the VEGF-induced ratio of P cluster to A cluster dramatically. Under any given treatment condition a fraction of the population follows dynamic phenotypic transitions characterized by each of these clusters, with the particular fractions altered by treatment condition. Thus, overall population behavior is represented by individual cell programs rather than by each cell following an idiosyncratic transition trajectory, and environmental stimuli govern the proportion of cells operating within a particular program.

4.2 Background and Motivation

The power of hybrid-agent based approach to model angiogenesis is critically dependent on having a strong foundation in experimental characterization of the phenotypic behavior responses of endothelial cells to angiogenic and angiostatic stimuli. This characterization needs to possess a number of complex features, including: a a probabilistic nature, since individual cells may exhibit different phenotypic behaviors in a given environment; b a dynamic nature, since any given cell may exhibit different phenotypic behaviors over the course of time; c a contingent nature, since these behaviors will likely be influenced by environmental conditions such as cytokine stimuli. With an aspiration for aiding the advance of computational modeling approach of angiogenic sprouting predictions, we endeavor in this work to contribute a necessary advance in the underlying experimental foundation.

Toward the goal of constructing a framework for characterizing quantitative, probabilistic, dynamic, and contingent endothelial cell phenotypic behaviors to combinations of angiogenic and angiostatic stimuli, we have designed and implemented an experimental and analytical methodology to determine stochastic transition rate parameters among the four key phenotypic behaviors involved in angiogenic sprouting:

proliferation, migration, apoptosis, and a state representing quiescent/sessile (i.e., not proliferating or migrating). Although we are aspiring to broader generality, we have aimed this initial manifestation of our framework to be consistent with a particular agent-based model from the Kamm laboratory at MIT [111]. We establish a method to identify phenotypic cell behavioral state from time-lapse live-cell microscopic imaging, showing that the basic phenotypic states can be inferred from cell morphology and movement parameters. Using this state identification tool, we then characterize the state transition dynamics of more than 500 individual human microvascular endothelial cells (hMVECs) over 24-30 hours across 5 different concentration combinations of angiogenic and angiostatic cytokines (VEGF and PF4, respectively). We find that the transitions among the phenotypic states are consistent with the conditional independence and the memoryless properties of a continuous-time Markov (CTM) process. As such, a continuous-time Markov framework provides a valid model of dynamic phenotypic state transitions, with the transition rates estimable from single-cell trajectories. We discover that the hMVEC population comprises several subpopulations, which cluster with respect to distinct state transition patterns that remain categorically consistent across the landscape of cytokine conditions. The angiogenic VEGF and angiostatic PF4 treatments alter the hMVEC population behavior by changing the proportion of cells adopting the various state transition patterns categories, or "programs."

4.3 Results

4.3.1 Human microvascular endothelial cells can generate angiogenic sprouts from confluent monolayer on Collagen I gel

Human microvascular endothelial cells (hMVECs) can be induced to initiate angiogenic sprouts from a monolayer seeded upon a Collagen I gel (Figure 4-1a,b). The extent of sprout initiation has been attributed to the net balance between

pro-angiogenic, anti-angiogenic and angiostatic cytokines in the microenvironment [19, 21]. Using both a more traditional angiogenic assay setup (endothelial monolayer on gel as reported in [112, 15]) and our microfluidic device, we can modulate the extent to which sprout initiation occurs by treatments with the potent angiogenic cytokine VEGF (Supplementary Figure 1b).

To understand how combinations of angiogenic and angiostatic cytokines affect the hMVEC population at individual cell level, we used microscopy to track cells over the course of 24-30 hours and ascertained their phenotypic patterns by image analysis. To follow individual cells in fluorescent time-lapse images, a mixture of cytoplasmic GFP-labeled, RFP-labeled, and unlabeled hMVECs were seeded at a 1:1:3 ratio. This mixed cell population was allowed to adhere on 2.0 mg/mL Collagen I gel for 4 hours in endothelial growth medium and then incubated with growth factor-free, low serum medium for 20 hours, completing a 24 hour period after seeding. The cells are then stimulated with cytokines and immediately imaged in a live-cell imaging chamber with regulated temperature, humidity and CO_2 levels (Figure 4-1c). Cell contours were detected using a modified level set active contour algorithm [110], with cell centroids computed as the center of mass of the detected contour points (Figure 4-1d). From these individual-cell contours and centroid tracks, we determined the phenotypic state of each time point in the track using morphology- and movement-related features as discussed in the following section.

4.3.2 Individual endothelial cells exhibit four identifiable phenotypic behaviors: Sessile, Proliferative, Migratory, and Apoptotic

Timelapse imaging and tracking of hMVEC contours and centroids revealed four distinct major phenotypes exhibited by any given cell at any given time-point: proliferative, apoptotic, migratory, and sessile; these are identifiable based on cell morphology

and dynamics of transient motility features (Figure 4-2a). Proliferative and apoptotic phenotypes are characterized by doubling/splitting and disappearance/shrinkage of existing contour respectively and can be detected as changes in contour topology. Migratory phenotype is characterized by productive and persistent translocation of the centroid, whereas sessile phenotype is characterized by erratic and unproductive centroid variation. A single-cell track is obtained from live-cell imaging as a temporal series of snapshots of the cell contour and centroid properties; we refer to individual snapshot as an instance in the track. To assign a phenotypic state to each instance of a given track, we used a hybrid approach outlined in Figure 4-2b. First, we determined whether the contour topology changes (splits, or collapses), with respect to the previous time-step within the instance being state assigned. If a contour instance splits or collapses, we assign the instance to be in proliferative or apoptotic state respectively. If the contour topology does not change, the instance is subjected to further classification into either migratory or sessile states.

Based on the above description of migratory vs. sessile states, it is unlikely that a single motility feature is sufficient as a discriminatory criterion. To undertake migratory vs. sessile classification in a more informed yet still unbiased manner, we computed morphological and motility related features of instances of centroid tracks (listed in Table 1). Among these features, we include cell step size and velocity autocorrelation function (VACF), which are one-interval equivalents of speed and directional persistence of cell migration respectively. Hierarchical clustering analysis in the feature space reveals two distinct subsets of instances (Figure 4-2c). Notably, the first subset (orange cluster) is characterized by high mean $VACF_N$ and low variance of $VACF_N$, fitting the migratory description. Conversely, the other subset is characterized by low mean $VACF_N$ and high variance of $VACF_N$ (aqua cluster) which follows the sessile description. Three-dimensional principle component embedding of the instances shows clear separation of the two clusters, supporting that mean and variance of VACFs are important determinants of migratory vs. sessile instances (Figure 4-2d).

To achieve a robust classification result, we performed hierarchical clustering on multiple randomly-drawn subsamples of cell track instances. In all of the subsamples analyzed, the hierarchical clustering yields two clusters (example shown in Figure 2d). To reliably classify the rest of the cell track instances, we used these cluster assigned subsamples (of cell track instances) as labeled data to train, test, and cross validate an ensemble of base classifiers using the Adaptive Boosting algorithm [93, 87]. The validated ensemble classifier achieved the desired classification task as seen from the images of cell centroid tracks and the sessile vs. migratory state prediction (Figure 4-2e). In the instances in which cells exhibit productive locomotion, the instances are labeled migratory (shown as orange centroid track and contours), while those in which cell contours or centroid fluctuate erratically the instances are labeled sessile (shown as aqua centroid track and contours). Taken together, these results demonstrated that our state annotation approach yields satisfactory classification results using an unbiased image analysis algorithm.

4.3.3 Single cell state transition patterns statistically follow one step dependent continuous time Markov chain (CTMC) dynamics

Applying the state classification method described above, we converted the time-series snapshots of each cell track into a sequence of states with corresponding waiting time prior to each transition; we refer to this sequence as a single-cell state trajectory (illustration in Table 2). We verified that the transition dynamics of these single cell trajectories are well characterized by continuous time Markov process based on two criteria. First, the waiting time distributions of the state transition in the data are well estimated by an exponential distribution (Supplementary Figure 2a). Second, the state transitions are consistent with the conditional independence properties of a one step dependence continuous time Markov chain [81].

An advantage of modeling single cell trajectory as a continuous time Markov chain (CTMC) is that the parameter estimation problem based on likelihood function

can be solved analytically. In a CTMC, the probability at which a cell transitions from a state s to another state s after some time t depends on the relative rates to s compared to the rates to other states s reachable from s (details in SI). Since individual state transitions in CTMC are independent, the likelihood of a single cell trajectory (as a sequence of state transitions and corresponding waiting time) is a product of likelihood of all individual transitions (illustration in Table 2). From this likelihood of single cell trajectories (expression in Table 2), we can determine the set of transition rate parameter values most consistent with the observed single cell trajectories by either a maximum likelihood estimation (MLE) or Bayesian inference. In either case, we rely on the same likelihood distribution of the phenotypic transition rates given the observed single cell trajectories (details in SI). For MLE, we solved for the rate parameter sets that maximize the likelihood distribution function whereas for the Bayesian approach we weighted the likelihood distribution by a conjugate prior and renormalized the resulting distribution.

By combining automatic phenotypic state identification from single-cell data and the parameter estimation procedure, we have a method that enables determination of the phenotypic state transition rates consistent with agent-based modeling. Our rate parameter estimation methodology consists of three main aspects. First is the contour tracking method that maps the input time-lapse images to sets of contour points outlining individual cells. Second is the automated state annotation based on features derived from the input images, the detected contour points, and the centroids. Third is parameter estimation method based on CTMC. We can now proceed to the application of our method to a particular biological system: quantitative analysis of how hMVEC population behavior related to angiogenic sprouting is influenced by competing angiogenic and angiostatic stimuli.

4.3.4 VEGF and PF4 differentially influence hMVEC dynamic phenotypic state transitions by altering the distribution of cells among diverse behavioral subpopulations.

With our analysis methodology in hand, we proceeded to examine the phenotypic state transition dynamics of hMVECs treated with vascular endothelial growth factor (VEGF) and platelet factor 4 (PF4) – opposing angiogenesis modulators that are co-released from activated platelets during the onset of inflammation[51, 23]. The cytokine conditions selected for this study (control, 20 ng/mL VEGF, 50 ng/mL PF4, and 500 ng/mL PF4, and combinations thereof) are physiologically relevant for angiogenesis under acute inflammation conditions, and have been shown to effectively modulate sprouting angiogenesis in vitro and in vivo [60, 101, 108]; VEGF induces sprouting at this concentration, and PF4 at the higher concentration suppresses VEGF-induced sprouting. The question we address here specifically is how these treatments influence the various individual-cell phenotypic behaviors that are coordinately involved in determining the extent of sprouting.

Figure 4-3 shows the single-cell state trajectories for each of the 5 cytokine treatment conditions. Some differences among the sets of trajectories seem readily apparent, such as more migratory states for the VEGF-treated cells, but the quantitative comparisons of both kinds of states and transitions between them are not obvious from inspection. Thus, we need to bring a next layer of computational analysis to bear on these data, in order to elucidate the key treatment condition-related influences.

We can imagine two kinds of conceptual models to account for the individual-cell phenotypic state transitions as they are distributed across a cell population (Figure 4-4). A *Uniform Population Model* (UPM) posits that all cells in the population intrinsically possess identical potential to adopt different phenotypic states, such that

the population state transition rates are described by a single transition rate parameter set. In contrast, a*Diverse Population Model* (DPM) posits that endothelial cells within angiogenic population are heterogeneous in their state transition dynamics such that it cannot be described by a single parameter set (Figure 4-4). One or the other kind of model might prove superior with respect to capturing the features of our experimental data, although it is possible that both kinds of models can do so satisfactorily. If the UPM is superior, the dependence of phenotypic transitions on context conditions is due to a uniform population of cells exhibiting transition probabilities that are as a whole modulated by context (angiogenic/angiostatic cytokine treatment); if, on the other hand, the DPM is superior, the context dependence is better explained as due to cell subpopulations exhibiting transition probabilities invariant with respect to treatment but with the treatment modulating the proportion of cells in each subpopulation.

To address this question, we applied our parameter estimation method in two ways. First, under the UPM, we performed parameter estimation on the single cell trajectories within each condition separately and refer to the rates estimates obtained via this approach as *condition-based estimates* ($\lambda^{(\text{cond})}$). Alternatively, under the DPM, we first determined whether subpopulations of distinct state transition dynamics exist, using unsupervised clustering of the single-cell trajectories in the feature space of transition dynamic descriptors (Table 2). We subsequently performed parameter estimation on the single-cell trajectories within each cluster separately. The rate estimates obtained via this approach is referred to as *cluster-based estimates* ($\lambda^{(\text{clust})}$).

For this set of cytokine treatments, the UPM-derived condition-based estimates are shown in Figures 4-5a and b. Some differences can be seen between the phenotypic state transition rates for different cytokine treatment conditions. Going from no cytokine control to VEGF-treated conditions (fourth and third bars in Figure 4-5b subplots respectively), the transition rates among S, P, and M states increase dramatically while the S-to-A transition rate decreases mildly, consistent with previous

findings that VEGF promotes proliferation, migration, and survival [50]. Going from control to PF4-treated (fourth and fifth bars in Figure 4-5b subplots), the S-to-P transition rate diminishes, S-to-M transition mildly decreases, while S-to-A transition mildly increases, suggesting that PF4 suppresses proliferation [101, 55]. Going from VEGF-treated to combination with PF4 (third, second, to first bars in Figure 4-5b subplots respectively), the P-to-S, M-to-S, M-to-P, and M-to-A directionally decreases as PF4 concentration increases, while other rates do not change directionally. Pair-wise comparisons using Kolmogorov-Smirnov (KS) criteria (Figures 4-5c and 4-5d) indicates that majority of these treatment-related changes are statistically significant. White space in these panels indicate state transitions that are not observed to a quantitative extent. Figure 4-2c shows the log p-values which in this case represent the probabilities of rejecting by mistake the Komolgorov-Smirnov null hypothesis that a change in the transition probability between the particular treatment condition pair is due merely to chance. Figure 4-5d denotes the statistically significant changes in white squares. Thus, only about 13% (20 out of 160 of the off-diagonal squares) of the observed changes do not reach significance of 0.05 with Bonferroni correction; however, the vast majority of these 13% are associated with PF4-related treatments. All together, these results suggest that while the VEGF-induced changes are consonant with previous findings and are predominantly statistically significant, the PF4-induced changes are more complex and difficult to interpret with the UPM framework.

To pursue the alternative DPM-derived cluster-based estimates, we ascertain descriptors of state transition dynamics that will resolve the differential transition rates of single cell trajectories within the population pool. Accordingly, we investigate the likelihood expression specifying the probability of observing single cell trajectories given particular values of the rate parameters (equation in Table 2). The expression contains two sets of experimentally obtainable variables: {a} $f_{ss'}$ is the trajectory length normalized frequencies of the transition from s to s' states; and {b} $\sum t_s$ is the total dwell or waiting time in a particular state s for that trajectory. Note that

$f_{ss'}$ describes the average frequency at which ss state transition occurs, while $\sum t_s$ the total s state dwell time is inversely proportional to the rate at which an agent escape state s. Intuitively, these parameters are relevant descriptors of state transition dynamics and can be used as clustering features.

Hierarchical clustering of single cell trajectories based on the aforementioned features reveals three to five identifiable clusters (Figure 4-6a). Notably, the clustering pattern and the cluster assignment correspond well to the different cellular phenotypes in which cells dwell in the most. Clusters 1 and 2 consist exclusively of single-cell trajectories that transition through apoptotic and proliferative states and are referred to as apoptotic (A cluster) and proliferative (P cluster) respectively. Clusters 3, 4, and 5 contain trajectories that traverse only through sessile and migratory states and are more related. Trajectories in Cluster 3 are characterized by relatively longer dwell time in sessile and Cluster 4 by relatively longer dwell time migratory states and are referred to as sessile (S cluster) and migratory (M cluster) respectively. Cluster 5 is highlighted by the high frequencies of transitions between sessile and migratory states and is referred to as switching (Sw cluster). Each of these clusters can be represented by cluster-based transition rate constant values (Figure 4-6b), characterizing the dynamic probabilities for each subpopulation in quantitative manner. The MLE matrices here permit explicit appreciation of the underlying structure of the key phenotypic transitions, which may not be easily discerned from the trajectories. For instance, A cluster exhibits the largest rate constants for transition into A state, but predominantly from S state and M state. For another, P cluster shows a large rate constant for transition into P state but only from S state.

As a complementary way to see these behavioral subpopulations, projection in principle component subspace (Figure 4-7a) shows clear separation among A cluster and P cluster and the aggregate of S, M, and Sw clusters confirming that single cell trajectories of different clusters should be assigned distinct sets of transition rate constants. The same hierarchical clustering analysis performed on single-cell

trajectories of different treatment conditions yield similar clustering patterns (Figure 4-7b), suggesting that: {a} the hVMEC population is heterogeneous with respect to angiogenesis-related phenotypic behaviors and can adopt one of a few distinct state transition patterns; and {b} that angiogenic and angiostatic cytokine treatments alter the distribution of the population among these distinct patterns.

To examine the cytokine effects within the DPM framework, we computed the cluster weight coefficients of each treatment condition with respect to proportion of cells in each behavioral subpopulation (Figure 4-6c). In the no cytokine control condition (fourth bar), almost half (0.48) of the weight is in the S cluster (blue), while about quarter of the weight (0.24) of is in the Sw cluster (purple). In this condition, the proliferative (green), migratory (orange), and apoptotic (red) cluster weights are small (about 0.1 each). Upon adding 20 ng/mL VEGF alone (third and fourth bars in Figure 4-6c), the cluster P and cluster M weights increase while cluster A and cluster S weight decreases drastically. Upon adding 500 ng/mL PF4 alone (comparing fourth and fifth bars in Figure 4-6c), the weights do not significantly change, suggesting that PF4 alone does not alter the phenotypic state transition rates. However, increasing PF4 concentration from 0 to 500 ng/mL under constant 20 ng/mL VEGF concentration (comparing third, second, to first bars in Figure 4-6c respectively) yields a reduction in the proliferative cluster weight from 0.16 to 0.03 and an increase in the apoptotic cluster weight from 0.04 to 0.10. Compared to the corresponding conditions with VEGF, the conditions with no VEGF have higher apoptotic (0.10 vs. 0.14) and sessile cluster weights (0.36 vs. 0.48) and slightly lower migratory cluster weights (0.10 vs. 0.08).

To determine whether these directional changes are statistically significant, we estimated the distribution of weight coefficients by bootstrapping. We drew 1000 random samplings with replacement of 50 trajectories from the pool of all single-cell trajectories. For each of these samplings, we assigned clusters based on relative similarities of the sampled trajectories to the cluster prototypes (cluster means in the

feature space) in Figure 4-6a and computed the cluster weight coefficients. We performed pair-wise comparisons of the resulting cluster weight coefficient distributions across different cytokine conditions using non-parametric Kolmogorov-Smirnov (KS) tests with the null hypothesis that the two samplings are drawn from the same distributions. For 47 of the 50 pair-wise comparisons, the weight coefficient differences are statistically significant to the 0.05 level (Figures 4-8b and c). These results confirm that the cytokine-elicited changes in the cluster weights are robust across the various treatment conditions, and suggest that the DPM appears to be more effective than the UPM in characterizing individual endothelial cell phenotypic transitions as they are modulated by angiogenic and angiostatic cytokines.

4.4 Discussion

To understand why the cluster-based estimates were better suited to our experimental data, we examine the optimization conditions in condition-based and cluster-based MLE derivations. Condition-based rate estimation seeks to find a set of rate parameters that maximizes the likelihood of observing the pool of single-cell trajectories subjected to the same cytokine conditions. Alternatively, cluster-based rate estimation first determines the similarity/differences or patterns in the transition dynamics of the entire pool of the single cell trajectories, and then seeks the rate estimates consistent with the patterns of state transition dynamics. This difference is reflected in optimization conditions as the sum over different sets of single cell trajectories log likelihood (SI section 3). In the presence of cell subpopulation of different transition dynamics (as in Figure 7a), adopting condition-based estimates amounts to attempting to describe a multimodal distribution by unimodal distribution descriptors.

In our hMVEC population, we have found that regardless of treatment condition a few distinct behavioral subpopulations exist with respect to phenotypic trajectories. We hypothesize that these patterns represent unique phenotypic programs available

to individual cell. Based on the results presented here, we surmise that angiogenic endothelial cells do not switch a chosen phenotypic program (i.e., do not transition to a different cluster) at least within the 24-30 hours observation period. For proliferative program, this observation is consistent with the reported average period of proliferation cycle (23 - 67 hours depending on the growth medium conditions and number of passages [37, 113]). While the information on apoptotic dynamics in endothelial cells is limited, our findings are consistent with the reported average apoptotic time in Hela cells [97].

4.4.1 Implications of phenotypic diversity in angiogenic population

An important challenge in developing reliable, and even predictive, approaches to modulate angiogenesis in biomedical applications, such as for tissue regeneration or anti-cancer therapeutics, is the need for design principles that offer guidelines for how molecular-level interventions will alter tissue-level properties via cell-level behavioral processes. The past decade has witnessed advances in multi-scale (often agent-based) computational modeling of angiogenesis aimed toward this objective, generating theoretical predictions and insights concerning the molecular-to-cell and cell-to-tissue relationships. A consequent need is accompanying quantitative experimental information from which these models can be constructed and constrained. In the work we offer here, we have designed and implemented an experimental measurement and data analysis method that quantifies multiple concurrent phenotypic behavioral responses of individual cells to angiogenic and angiostatic cytokine treatment conditions relevant for new blood vessel sprouting along with a set of parameter estimates that characterize the dynamic transition rates among these various behavioral responses as they depend on the different conditions. Our method consists of three main components: cell contour detection, automated state annotation, and rate maximum likelihood estimate (MLE) computation based on continuous time Markov

model analysis. Combined with application-specific variations of the contour detection algorithms, our automated state identification and rate MLE computation can be applied to estimate parameters describing other dynamical processes from single-cell data.

To address the effect of opposing inflammatory cytokines VEGF and PF4 on phenotypic state transition dynamics, we have considered two conceptual models to account for variations in phenotypic transition dynamics across cell population: uniform population model (UPM) and dynamic population model (DPM). We have shown that under DPM, the cytokine-elicited changes can be understood in a more straightforward and directional manner (Figure 4-6c). More importantly, the endothelial subpopulations identified under DPM are distinct and well separated in their unique transition dynamics (Figure 4-6a and 4-7a) and consistent across all cytokine treatment conditions (Figure 4-7b). Taken together, our findings offer a novel perspective in understanding the phenotypic behaviors of endothelial cell population as a unique consistent set of dynamic transition cassettes across both angiogenic and angiostatic cytokine stimuli. In this light, the influence of the angiogenic and angiostatic cytokines is usefully characterized as the directional changes in cell population proportions within the various dynamic transition programs.

Agent-based models of angiogenesis in the literature (including previous contributions from our laboratory [30, 111]) typically assume that the vascular endothelial cells can be described in terms of a uniform population model in which the cell population is homogeneous and any given treatment condition modulates the phenotypic behaviors according to an identical relationship (whether deterministic or probabilistic) for all individual cells. We have found in our studies here that the phenotypic behavior of a human microvascular endothelial cell population is heterogeneous and, most remarkably, that this heterogeneity can be mapped to a small number of distinct patterns based on phenotypic transition dynamics. This heterogeneity may reflect cell-to-cell variability in genetic, epigenetic regulation and protein

expression. Alternatively, we speculate that the observed heterogeneity may serve as diverse potential phenotypes among which endothelial cell can adopt, especially if such heterogeneity can be directionally altered by relevant cytokine stimulation. In this study, we demonstrate examples supporting cases of such directional alterations by potent angiogenic cytokine VEGF and PF4 – as VEGF induces higher fraction of the population to adopt the transition pattern consistent in proliferative program and lower fraction to adopt apoptotic program while angiostatic cytokine PF4 exerts the opposite directional effect on endothelial population.

Primary angiogenic endothelial cells take on multiple roles in physiological and pathological conditions. Apart from being central players in sprouting angiogenesis, they act as selective barrier for transport of molecules and immune cells between blood and tissues, help regulate blood fluidity, and participate in inflammatory responses. In each of these roles, endothelial cells need to exhibit different phenotypes (31,32). To achieve wide variety of phenotypic requirements, individual cells in a homogeneous endothelial population have to be able to switch their responses accordingly. Our findings suggest that in a microvascular endothelial population, at least transiently, endothelial population may achieve such diverse phenotypic requirement by possessing subpopulations specialized for different phenotypic responses.

4.5 Materials and Methods

4.5.1 Live imaging of hMVECs

Human adult microvascular endothelial cells (hMVECs) of dermal origin (purchased from Lonza at passage 4; Cat No. CC-2543) were maintained in culture according to manufacturer recommendations. Cells were passage once then stably infected with GFP and RFP plasmid following a standard retroviral infection protocol. For all live cell imaging experiments, GFP-labeled and RFP-labeled hMVECs were used at second passage after infection, while unlabeled hMVECs were used after three passages after the cells were received. hMVECs were mixed at 1:1:3 ratio in complete medium to allow visualization of single cell when seeded at instant monolayer density (50000 cells/cm^2) to allow sprout initiation on 1 mm thick 2.0 mg/mL Collagen I gel (BD Biosciences; Cat No. 356236). At 4 hours after seeding, adhered hMVECs were replaced with 5% FBS no cytokine medium. At 24 hours after seeding, hMVECs on gel were stimulated with VEGF and PF4 (Peprotech; Cat No. 100-20 and 300-16 respectively) . The cell were imaged upon stimulation using Cellomic array scan microscope.

4.5.2 Contour and centroid tracking by level set active contour

Fluorescent live cell images were enhanced by median and entropy filtering algorithms using the builtin scripts in the MATLAB R2011a image processing toolbox (MathWorks - Natick, MA). These preprocessed image were binarized (thresholded based on intensity histogram to partition intensity levels into that of the foreground and the background) and the foreground-background boundary of preprocessed image was used as an initial contour. Contour detected by a level set active contour algorithm of Chan-Vese [110] implemented in MATLAB and applied to filtered, unbinarized images. For time series images, the first image in the series was contour detected as described. For subsequent images, the contour detection was initialized with the

optimal contour of an immediately previous image in the series.

4.5.3 Pairwise statistical comparisons by Kolmogorov Smirnov test

Pairwise comparison were performed most extensively in two tasks: 1. comparing the condition- based rate MLEs ($\lambda^{(\text{cond})}$) across cytokine conditions (Figure 5cd) and 2. comparing the cluster weights MLE across cytokine conditions (Figure 6d-6f). In comparing $\lambda^{(\text{cond})}$, 1000 bootstrapped samples of 50 single cell MLE trajectories were drawn from the pool of trajectories within each condition. Maximum likelihood of $\lambda^{(\text{cond})}$) were computed from the sampled trajectories to $\lambda^{(\text{cond})}$ distributions. In comparing the cluster weights, 1000 bootstrapped samples of 50 trajectories were drawn from the trajectories in each condition. The trajectories were assigned to one of the five state transition dynamic clusters based on the relative Mahalonobis distances of the trajectories to all the cluster centers. The cluster weights are computed for each bootstrapped sample to form the distribution of cluster weights. In both of the pairwise statistical comparison task, both the $\lambda^{(\text{cond})}$ distributions and cluster weight distributions across conditions are compared using MLE Kolmogorov-Smirnov test with the significance level of 0.05.

4.5.4 Semi supervised sessile vs. motile state classification

In our dataset, there are more than 500,000 contour instances that need to classified into either sessile or motile state. To meet the challenge of this classification task, we took a semi-supervised learning approach. First, 10 non-overlapped small training sets (about 1-2%) of these instances were randomly sampled and clustered using agglomerative hierarchical clustering algorithm based on Euclidean separation of the contour instances in feature space. Individual instance in the training sets were state-labeled based on the cluster assignment. This state-labeled training set is used to train an ensemble of 25 or 50 base classifiers (decision stumps) using Adaptive Boosting algorithm [87, 93]. As the number of base classifiers is comparable or larger

than the dimension of contours feature space, the ensemble classifier is cross validated on unseen set of contour instances. The cross validated ensemble classifier is used to classify the rest of the contour instances and the classification results were visualized against the contour traces to ensure that the classification result follow definitions of sessile and migratory states.

4.6 Modeling single cell state trajectories as continuous time Markov chains (CTMCs)

In this work, we model individual cell as a decision making entity called Markov agent that transition among a finite number of phenotypic states. As we follow individual agent over time, we can trace out a sequence of states through which the agent traverses as well as the corresponding waiting times before each transition. We refer to the observed sequence as a cell's state trajectory. In choosing a stochastic model to describe the state transition of angiogenic endothelial cells, we showed that state trajectories satisfy the two Markov criteria can be modeled as a continuous time Markov chain: 1. memorylessness and 2. conditional independence properties (Supplementary Figure 2). A continuous time Markov chain (CTMC) is defined by the following descriptors: (1). a finite state set $\mathbb{S}$, (2) initial (marginal) state probabilities, (3) transition probabilities, and (4) state waiting time parameter. In the case of angiogenic endothelial cells, the appropriate set of phenotypic states are sessile (S), proliferative (P), migratory (M), and apoptotic (A). In the following section, we construct the likelihood expression of a single cell state trajectories from which the state transition rate parameters can be optimized.

4.6.1 Likelihood of one transition

To construct an analytical expression for the likelihood function, we first derive the probability of an occurrence of a state transition. Consider a one step transition from

s to a finite number of state reachable from s'_n shown below. The transition to state $s' \neq s$ happens at an exponentially distributed random time with rate parameter $\mu = \lambda_1 + \ldots + \lambda_N$.

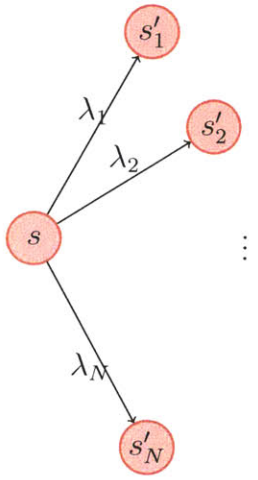

At the transition time, the new state s' is chosen with the probability

$$p_{s'} = \frac{\lambda_{s'}}{\lambda_1 + \ldots + \lambda_N} = \frac{\lambda_{s'}}{\mu}.$$

Given the transition rate parameter set $\Lambda = \{\lambda_s\}$ and the waiting time parameter μ and assuming that the process is in state s initially, the likelihood of the observing a transition ss' is given by

$$\begin{aligned} \ell(s_{k+1} = s' | s_k = s; T = \tau; \Lambda_s) &= Pr(\text{dwelling in } s_i \text{ for } t_i) \times \\ &\quad Pr(\text{transitioning from } s \text{ to } s') \\ &= e^{-\mu_s t_i} \times \frac{\lambda_{ss'}}{\mu_s}. \end{aligned}$$

4.6.2 Likelihood of one state trajectory

As the next step, consider an experimentally observed single cell state trajectory as a sequence of state transitions. Let $\mathcal{U} = (s_0, t_0, s_1, t_1, \ldots, s_{k-1}, t_{k-1}, s_k)$ denotes the set of random variables describing a CTMC of single cell state trajectory up to time t and let $\ell_{ss'}(t)$ represents the likelihood of ss' type transition at time t. Under the CTMC assumption, individual transition are independent of one another and the likelihood of a state trajectory $\mathcal{U}$ is simply the product of individual transition in the trajectory. As such, the likelihood of a particular state trajectory with η transitions is given by:

$$\ell(\mathcal{U}_t | s_o, \Lambda) = P_{s_o} \prod_{i=1}^{\eta} \ell_{s_i s_{i+1}}(t_i),$$

where P_{s_o} is the initial probability of finding the process in state s_o initially.

We can further simplify the likelihood expression as follows. Let $\eta_{ss'}$ be the total number ss' type transitions in a trajectory and let $\mathbb{H}$ be the set of all transition types. Since the transitions in a trajectory are independence, one can factorize the above likelihood expression based on the transition types. The resulting likelihood expression is given by

$$\begin{aligned}\ell(\mathcal{U}_t|s_o,\Lambda) &= P_{s_o}\prod_{ss'\in\mathbb{H}}\Big(\prod_{h_{ss'}=1}^{\eta_{ss'}}\ell(ss',\tau_{h_{ss'}})\Big)\\ &= P_{s_o}\prod_{ss'\in\mathbb{H}}\left(\frac{\lambda_{ss'}}{\mu_s}\right)^{\eta_{ss'}}\exp\big(-\mu_s\sum_{h_{ss'}=1}^{\eta_{ss'}}\tau_{h_{ss'}}\big).\end{aligned}$$

To obtain the generalized likelihood expression for the entire observed population, one assumes independence of state transition among cells in the population, in which case the joint likelihood is simply the product of the likelihood of all trajectories within the population.

4.6.3 Estimation of the transition rate parameters

To obtain the state transition rate estimates from the data, we rely on two parameter estimation techniques: Maximum likelihood estimation, and Bayesian estimation. Both of these estimation methods find parameter values (in MLE case) or posterior rate distribution of the parameter (in BE case) that are most consistent with the observation as described by the likelihood distribution.

4.6.4 Maximum Likelihood Estimation

Consider a set of state trajectories $\mathbb{U} = \{\mathcal{U} = (s_o, s_1, t_1, \ldots s_{\eta-1}, t_{\eta-1}, s_\eta)\}$. To find the parameter set that is most consistent with the observed trajectories, we seek to optimize the above likelihood function for a collection of state trajectories subject to

the following constraints:

$$\begin{aligned} \sum_{s'} \lambda_{ss'} &= \mu_s, \qquad \forall s \qquad \text{and} \\ \lambda_{ss'} &\geq 0, \qquad \forall ss' \in \mathbb{H}. \end{aligned}$$

Since it is more convenient to optimize the logarithm of likelihood, we set up the optimization in term of log likelihood using the Lagrange's method:

$$\begin{aligned} \underset{(\lambda_{ss'})\in\Lambda}{\operatorname{argmax}} \log(\ell(\Lambda)) &= \underset{(\lambda_{ss'})\in\Lambda}{\operatorname{argmax}} \mathcal{L} \\ &= \underset{(\lambda_{ss'})\in\Lambda}{\operatorname{argmax}} \left[\log(P_{s_o}) + \sum_{ss'\in\mathbb{H}} \left(\eta_{ss'} \log\left(\frac{\lambda_{ss'}}{\mu_s}\right) - \mu_s \sum_{h_{ss'}=1}^{\eta_{ss'}} t_{h_{ss'}} \right) \right. \\ &\qquad \left. - \sum_s \left(\zeta_s \left(\sum_{ss'} \lambda_{ss'} - \mu_s \right) \right) \right], \end{aligned}$$

where $\zeta_{ss'}$ are the Lagrange's multiplers. For each of the rate parameter $\lambda_{ss'}$, we take the derivatives of the log likelihood with respect to $\lambda_{ss'}, \mu_s, and \zeta_{ss'}$ and set them to zero. The resulting system of equations take the form:

$$\begin{aligned} \frac{\partial}{\partial \lambda_{ss'}} &= 0 = \frac{\eta_{ss'}}{\lambda_{ss'}} - \zeta_s \quad , \\ \frac{\partial}{\partial \mu_s} &= 0 = -\frac{\eta_{ss'}}{\mu_s} - \sum_{h_{ss'}=1}^{\eta_{ss'}} t_{h_{ss'}} + \zeta_s \quad , \\ \frac{\partial}{\partial \zeta_s} &= 0 = \sum_s \lambda_{ss'} - \mu_s. \end{aligned}$$

Assuming that $\lambda_{ss'} > 0$, we rearrange the above expression and to obtain the maximum likelihood estimates of the parameters:

$$\begin{aligned}
\lambda_{ss'}^{\text{MLE}} &= \frac{\eta_{ss'}}{\sum_{h_{ss'}} t_{h_{ss'}}} \left(1 - \frac{\eta_{ss'}}{\sum_s \eta_{ss'}}\right) \quad , \\
\mu_s^{\text{MLE}} &= \frac{\sum_{s'} \eta_{ss'}}{\sum_{h_{ss'}} t_{h_{ss'}}} \left(1 - \frac{\eta_{ss'}}{\sum_s \eta_{ss'}}\right) \quad , \\
\zeta_s &= \frac{\sum_{h_{ss'}} t_{h_{ss'}}}{1 - \frac{\eta_{ss'}}{\sum_{s'} \eta_{ss'}}}.
\end{aligned}$$

The above maximum likelihood estimators can be easily applied to multiple trajectories (i.e. a subpopulation of multiple cells) by extending the summation of log likelihood over all trajectories $\mathbb{U} = \{\mathcal{U}\}$.

4.6.5 Bayesian estimation

To estimate the posterior distribution of the rate parameter we rely on the Bayes' theorem which posits that the posterior distribution of the parameters given the evidence (observed data) equals the likelihood of the observed data given the parameters weighted by the evidence (marginal probability of the parameter), i.e.

$$\begin{aligned}
P(\Lambda|\mathbb{U} = \{\mathcal{U}\}) &= \frac{P(\mathbb{U}|\Lambda) \times P(\Lambda)}{P(\mathbb{U})} \\
&, = \frac{P(\mathbb{U}|\Lambda) \times P(\Lambda)}{\int_\Lambda P(\mathbb{U}|\Lambda) \times P(\Lambda)}.
\end{aligned}$$

4.7 Comparing the objective functions for the condition-based vs. the cluster-based phenotypic transition rate estimates

In this section, we examine the difference in the objective functions used to derive the *condition based* and the *cluster based rate estimates.* Starting with the likelihood ex-

pression derived in section 2, for *condition based estimates*, we optimize the likelihood function over the set of trajectories within one experimental treatment condition. Alternatively, for *cluster based estimates*, we derive the maximum likelihood values after clustering the trajectories.

Given a set of experimentally observed state trajectories collected under a set $\mathbb{C}$ of $\mathcal{N}_c$ cytokine conditions, let's assume that a set $\mathbb{K}$ of $\mathcal{N}_k$ clusters are detected, where $\mathbb{K}$ is the set of all clusters and $\mathbb{C}$ is the set of all conditions. Let $\rho_{ss'}^{c,k}$ denotes the total number ss' type transitions observed in the single cell state trajectories of cells under condition c and assigned to cluster k. (These subpopulations may be distinct in state transition dynamics as consistent with the diverse population model for the sake of model comparison.) Then, the log likelihood of observing just the trajectories within cluster k under condition c is given by

$$\mathcal{L}^{(c,k)} = \log(\ell^{(c,k)}) = \sum_{q^{(c,k)}} \log(P_{s_o}) + \eta_{ss'}^{(c,k)} \log\left(\frac{\lambda_{ss'}}{\mu_s}\right) - \mu_s \sum_{h_{ss'}=1}^{\eta_{ss'}^{(c,k)}} t_{h_{ss'}}.$$

Let $\xi_{ss'}^{(c,k)}(\lambda_{ss'}, \mu_s)$ be the derivative of log-likelihood with respect to $\lambda_{ss'}$ evaluated on the set of trajectories within condition c and condition k. From section 2, the this derivative take the following form:

$$\xi_{ss'}(\lambda_{ss'}, \mu_s) = \sum_{\text{trajectories}} \eta_{ss'} \left(\frac{1}{\lambda_{ss'}} - \frac{1}{\mu_s}\right) - \sum_{\text{trajectories}} \sum_{h_{ss'}=1}^{\eta_{ss'}} t_{h_{ss'}}.$$

Under the *uniform population model*, we optimize the log likelihood on the set each condition separate such that the derivative of likelihood for the subsets of trajectories within each condition n_c satisfy the following optimal condition

$$\sum_{k\in\mathbb{K}} \xi_{ss'}^{(c,k)}(\lambda_{c_{ss'}}^{(n_c)}, \mu_{c_s}^{(n_c)}) = 0 \quad \text{i.e.,}$$

$$\sum_{k\in\mathbb{K}} \rho_{ss'}^{(c,k)} \left(\frac{1}{\lambda_{c_{ss'}}^{(n_c)}} - \frac{1}{\mu_{c_s}^{(n_c)}}\right) - \sum_{k\in\mathbb{K}} \sum_{h_{ss'}=1}^{\rho_{ss'}^{(c,k)}} t_{h_{ss'}} = 0.$$

Alternatively, under the *diverse population model*, the derivative of log-likelihood follows the relation

$$\begin{aligned} \sum_{c\in\mathbb{C}} \xi_{ss'}^{(c,k)}(\lambda_{k_{ss'}}^{(n_k)}, \mu_{k_s}^{(n_k)}) &= 0 \qquad \text{i.e.,} \\ \sum_{c\in\mathbb{C}} \rho_{ss'}^{(c,k)} \left(\frac{1}{\lambda_{k_{ss'}}^{(n_k)}} - \frac{1}{\mu_{k_s}^{(n_k)}} \right) - \sum_{c\in\mathbb{C}} \sum_{h_{ss'}=1}^{\rho_{ss'}^{(c,k)}} t_{h_{ss'}} &= 0. \end{aligned}$$

In attempting to relate the condition and cluster based estimates, we introduce $\lambda_{ss'}^{(n_c,n_k)}$ and $\mu_s^{(n_c,n_k)}$ which are the transition and total exit rate parameter sets optimized over the single cell trajectories in the n_k cluster within the n_c condition. As such, this set of parameter satisfy the following optimization condition:

$$\begin{aligned} \xi_{ss'}^{(c,k)}(\lambda_{ss'}^{(n_c,n_k)}, \mu_s^{(n_c,n_k)}) &= 0 \qquad \text{i.e.,} \\ \rho_{ss'}^{(k,c)} \left(\frac{1}{\lambda_{ss'}^{(n_c,n_k)}} - \frac{1}{\mu_s^{(n_c,n_k)}} \right) - \sum_{h_{ss'}=1}^{\rho_{ss'}^{n_k,n_c}} t_{h_{ss'}} &= 0. \end{aligned} \tag{4.1}$$

The subcluster estimates $\lambda_{ss'}^{(n_c,n_k)}$ can be related to the condition based $\lambda_{c_{ss'}}^{n_c}$ and the cluster based estimates $\lambda_{k_{ss'}}^{n_k}$ as follow:

$$\text{Eq (4.1)} = \sum_{k\in\mathbb{K}} \text{Eq (4.1)} \quad ; \quad \left(\frac{1}{\lambda_{c_{ss'}}} - \frac{1}{\mu_{c_s}} \right) \sum_{k\in\mathbb{K}} \rho^{(n_c,k)} = \sum_{k\in\mathbb{K}} \left(\frac{1}{\lambda_{ss'}^{(n_c,n_k)}} - \frac{1}{\mu_s^{(n_c,n_k)}} \right) \rho^{(n_c,n_k)} \tag{4.2}$$

$$\text{Eq (4.1)} = \sum_{c\in\mathbb{C}} \text{Eq (4.1)} \quad ; \quad \left(\frac{1}{\lambda_{k_{ss'}}} - \frac{1}{\mu_{k_s}} \right) \sum_{c\in\mathbb{C}} \rho^{(c,n_k)} = \sum_{c\in\mathbb{C}} \left(\frac{1}{\lambda_{ss'}^{(n_c,n_k)}} - \frac{1}{\mu_s^{(n_c,n_k)}} \right) \rho^{(n_c,n_k)} \tag{4.3}$$

We can expand the sum, divide through by the total number of trajectories within a cluster ($\sum_{k\in\mathbb{K}} \rho^{(n_c,k)}$) for Eq (4.2) and the total number of trajectories within a condition $\sum_{c\in\mathbb{C}} \rho^{(c,n_k)}$) for Eq (4.3) to further simplify the above system of equations

to obtain the following relationships:

$$\frac{1}{\lambda_{c_{ss'}}} - \frac{1}{\mu_{c_s}} = \sum_{k \in \mathbb{K}} \left(\frac{w_c}{\lambda_{ss'}^{(n_c,n_k)}} - \frac{w_c}{\mu_s^{(n_c,n_k)}} \right) \quad \text{and}$$

$$\frac{1}{\lambda_{k_{ss'}}} - \frac{1}{\mu_{k_s}} = \sum_{c \in \mathbb{C}} \left(\frac{w_k}{\lambda_{ss'}^{(n_c,n_k)}} - \frac{w_k}{\mu_s^{(n_c,n_k)}} \right) \quad \text{, where}$$

$$w_c = \frac{\rho^{(n_c,n_k)}}{\sum_{k \in \mathbb{K}} \rho^{(n_c,n_k)}} \quad \text{and} \quad w_c = \frac{\rho^{(n_c,n_k)}}{\sum_{c \in \mathbb{C}} \rho^{(n_c,n_k)}}$$

are the relative occurrence weights of ss' type jump across condition within a cluster and the relative occurrence weights over cluster within a condition respectively. Though these results do not directly relate the condition based estimates to the cluster based estimates, they reveal that the condition based and cluster based estimates importantly differ by the relative occurrence of the transition types within the set of single cell trajectories over which the parameters are optimized.

4.8 Supplementary Figures

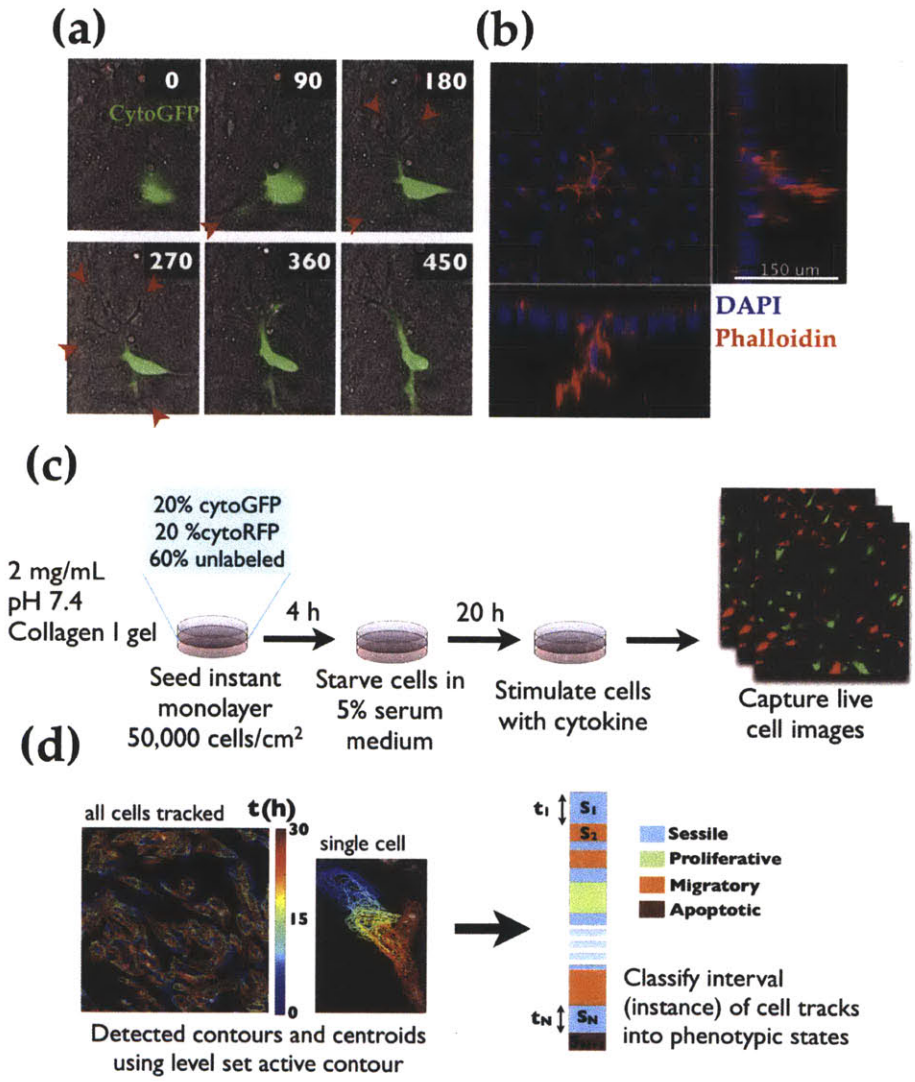

Figure 4-1: Angiogenic human microvascular endothelial cells (hMVECs) cultured on Collagen type I gel is capable of initiating angiogenic sprout. (a) Angiogenic protrusions of hMVECs in the collagen gel observed as shadow (red arrowheads) in phase contrast timelapse images. (b) Phalloidin staining of actin cytoskeleton showing an angiogenic sprout tip invasion over the distance of 150 μm into the collagen gel as observed in the confocal images. (c) Experimental setup for live cell imaging experiments. First, a mixture of GFP-labeled, RFP-labeled, and unlabeled hMVECs were seeded at an optimized seeding density (50,000 cells/cm2) to yield a confluent monolayer after 24 hours of seeding (instant monolayer density). Cells are starved for 20 hrs under 5% fetal bovine serum (FBS) supplemented cytokine-free base medium, then stimulated with angiogenic/angiostatic cytokines. After cytokine stimulation, cells are imaged over 24 - 30 hour period. (d) Illustration of the data analysis. From the fluorescent images, cell contours and centroids at each time point were detected by a level set active contour algorithm. The detected cell contours and centroids trajectories were classified into different phenotypic instances types: sessile, proliferative, migration, and apoptotic.

Feature	Type	Definition
step size (d)	motility	centroid-to-centroid distance between subsequent time step
mean velocity autocorrelation function across N steps (μ_{VACF^N})	motility	Sample mean of dot products of N adjacent unit velocity vectors
variance velocity autocorrelation function across N time step ($\sigma^2_{\text{VACF}^N}$)	motility	Sample variance of dot products of N adjacent unit velocity vectors
cell size (A)	morphology	Area enclosed by cell contour
cell elongation (ℓ)	morphology	Ratio between cell major and minor axes
cell orientation (θ)	mixed	Dot product of unit instantaneous velocity vector and unit major axis

Table 1: Types and description of morphological and motility related features used in classifying instances of cell tracks into sessile vs. migratory states. Morphological features were computed based on the detected contour points of individual contour instance. Motility related features were computed based on the detected centroid across N intervals flanking the instance being feature computed. Step size is the one time step equivalent of cell speed and velocity autocorrelation function is the one time step equivalent of directional persistence.

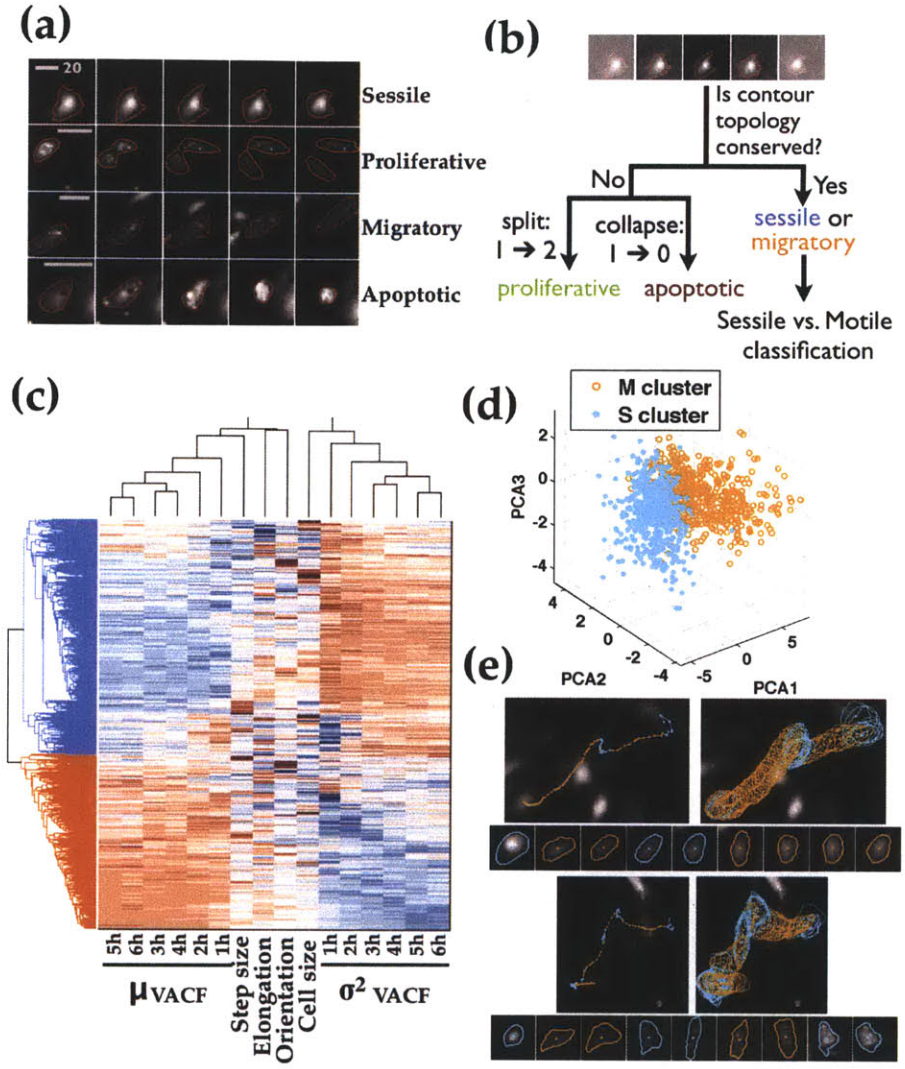

Figure 4-2: Timelapse imaging of hMVECs reveals four major phenotypes: proliferative, apoptotic, migratory, and sessile. (a) Example contours outlining hMVEC in sessile, proliferative, migratory, and apoptotic states as detected by level set active contour. Proliferative instances are characterized by contour splitting, while apoptotic instances by contour collapsing and disappearance. Scale bar is 20 ?m. (b) Semi-hierarchical scheme for state classification. Contour is first classified based on change in contour topology. If topology is conserved, they are further classified into sessile or migratory instances based on contour morphology, and centroid trajectory features. (c) Two clusters of topology-conversed, non-proliferative, non-apoptotic instances are identified by agglomerative clustering. The main discriminatory features between the two subsets are the mean and variance of velocity autocorrelation functions (VACFs) computed over 1 - 6 hour track intervals centered at the instance in which the feature is being computed. (d) Three component PCA projection of the motile vs. sessile instances as classified by an optimized ensemble of linear sessile vs. motile base classifiers (details in Supplementary text). (e) Examples of state-labeled contour and centroid trajectories (sessile in aqua, motile in orange). Contours labeled in orange correspond to the instances in which cells progress productively and persistently, consistent with motile state description. On the other hand, contours labeled in aqua correspond to instances of unproductive movement of cell centroid, consistent

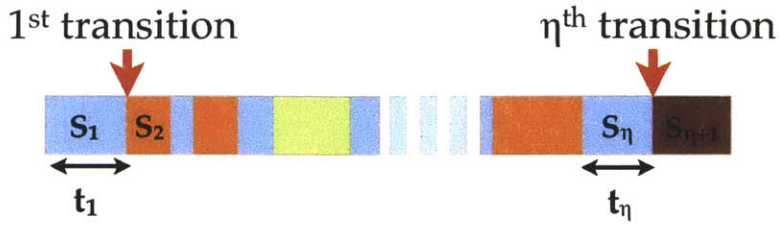

Equation 1

$$\ell(\mathcal{U}_t|s_o,\Lambda) = P_{s_o}\prod_{ss'\in\mathbb{H}}\left(\frac{\lambda_{ss'}}{\mu_s}\right)^{\eta_{ss'}}\exp\left(-\mu_s\sum_{h_{ss'}=1}^{\eta_{ss'}}\tau_{h_{ss'}}\right)$$

total number of ss' jumps

total dwell time in state s

Feature	Notation	Definition
ss' jump frequency (length normalized number of ss' jumps)	$f_{ss'}$	$\frac{1}{T}\frac{\eta_{ss'}}{\sum_{s'}\eta_{ss'}}$
total jump frequency (length normalized number of any jumps)	η^{tot}	$\frac{1}{T}\sum_s\sum_{s'}\eta_{ss'}$
Total dwell time in s	τ_s^{tot}	$\sum_{h_s}\tau_{h_s}$
mean dwell time in s	$\langle\tau_s\rangle$	$\frac{1}{\eta_s}\sum_{s'}\sum_{h_{ss'}}\tau_{h_{ss'}}$
variance dwell time in s	$\sigma^2_{\tau_s}$	$\sum_{h_{ss'}=1}^{\eta_{ss'}}(\tau_{h_{ss'}}-\langle\tau_s\rangle)^2$

Table 2: A hypothetical state trajectory with η state transitions. States are color-labeled. According to the continuous time Markov (CTM) model, the likelihood of a given the transition rate parameter set Λ given the observed state trajectory $\mathcal{U}$ is a product of the likelihoods of all individual transitions observed in the trajectory, and the marginal probability of the first state S_o (P_{S_o}). After an arithmetic manipulation, the likelihood can be written as in Equation 1. The likelihood expression contains two types of experimentally obtainable variables. The first is the total number of transitions of certain type ss' ($\eta_{ss'}$). The second set is total dwell time in a certain state s ($\sum_h t_h$). Since these variables partly determines the likelihood, they are used as features for classifying single state trajectories.

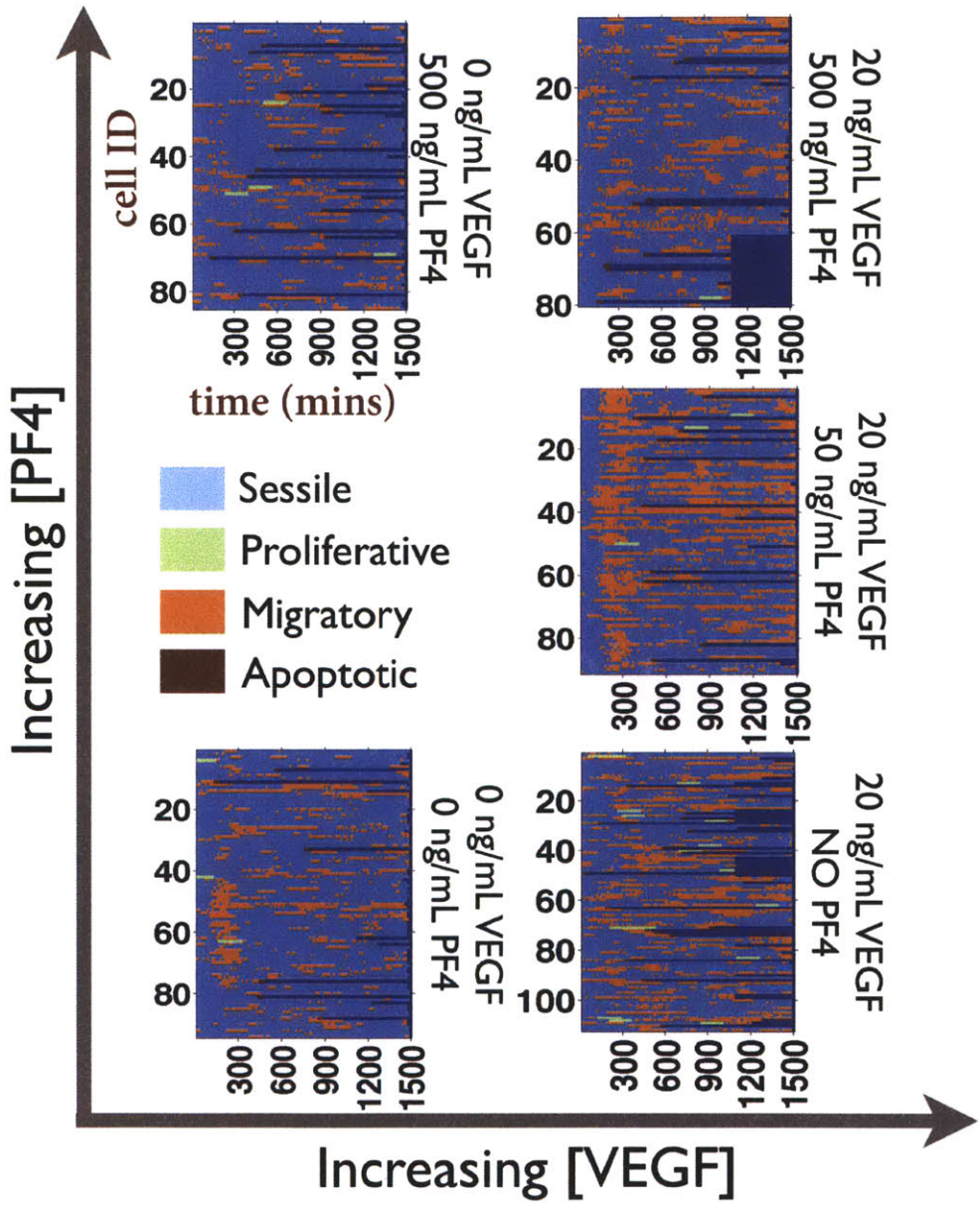

Figure 4-3: State labeled cell trajectories under different concentrations of counteracting angiogenic and angiostatic cytokines (VEGF and PF4 respectively). In the cell trajectory matrices, single cell state trajectories are plotted along rows.

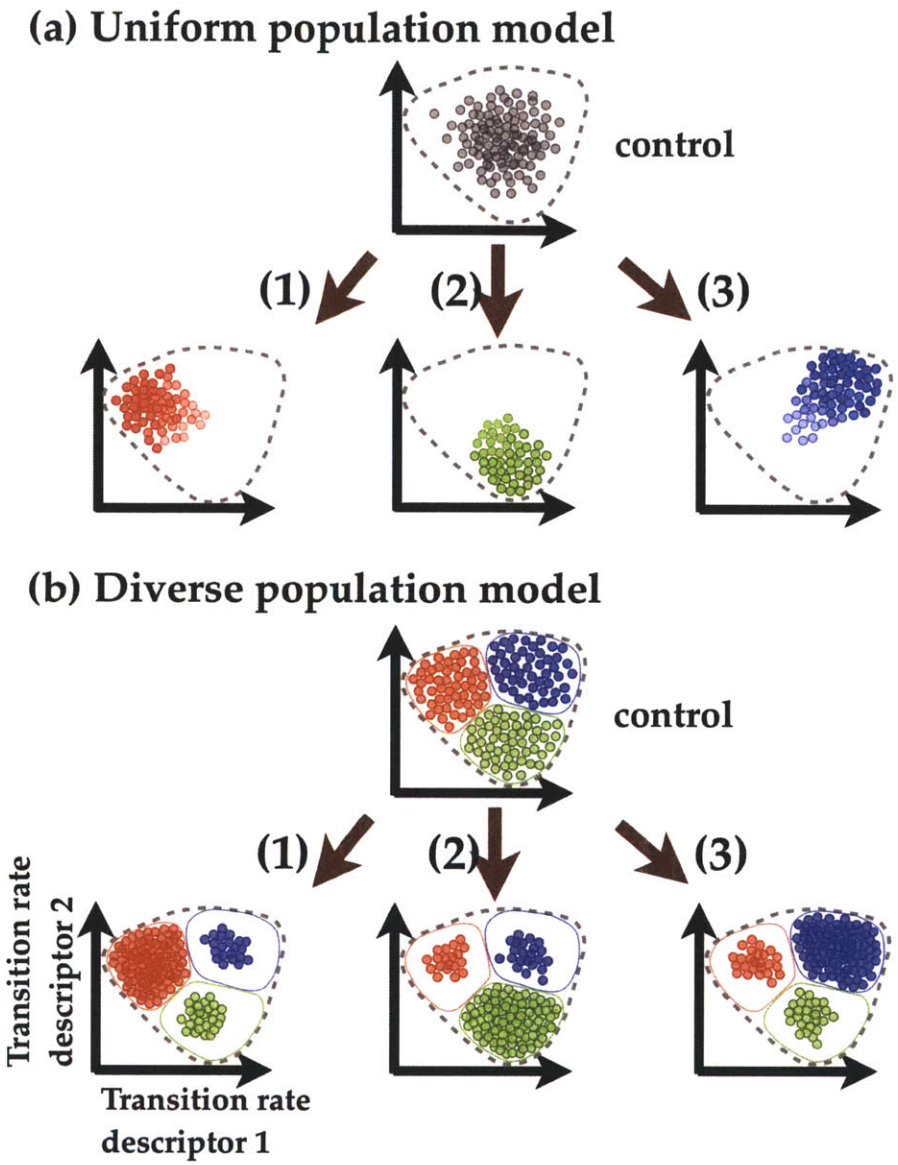

Figure 4-4: Conceptual models to account for the individual-cell phenotypic state transitions dynamics across an angiogenic population. (a) Uniform population model (UPM) posits that endothelial population is homogeneous in state transition dynamics and the population is unimodally distributed in transition rate parameter space (middle). Under the control condition, the population assumes a unimodal distribution in state transition rate parameters. Treatments with cytokines (shown as dark red arrows) cause individual cells to respond in a similar manner and the population distribution to shift unidirectionally (left, right and middle shown as results of three different stimulations). (b) Diverse population model (DPM) posits that endothelial population is heterogeneous in state transition dynamics. Under the control condition, the population consists of multiple subpopulations (clusters) characterized by different transition rate parameters. Treatments with cytokines cause changes in the fractions of cells within subpopulations without shifting subpopulations centers.

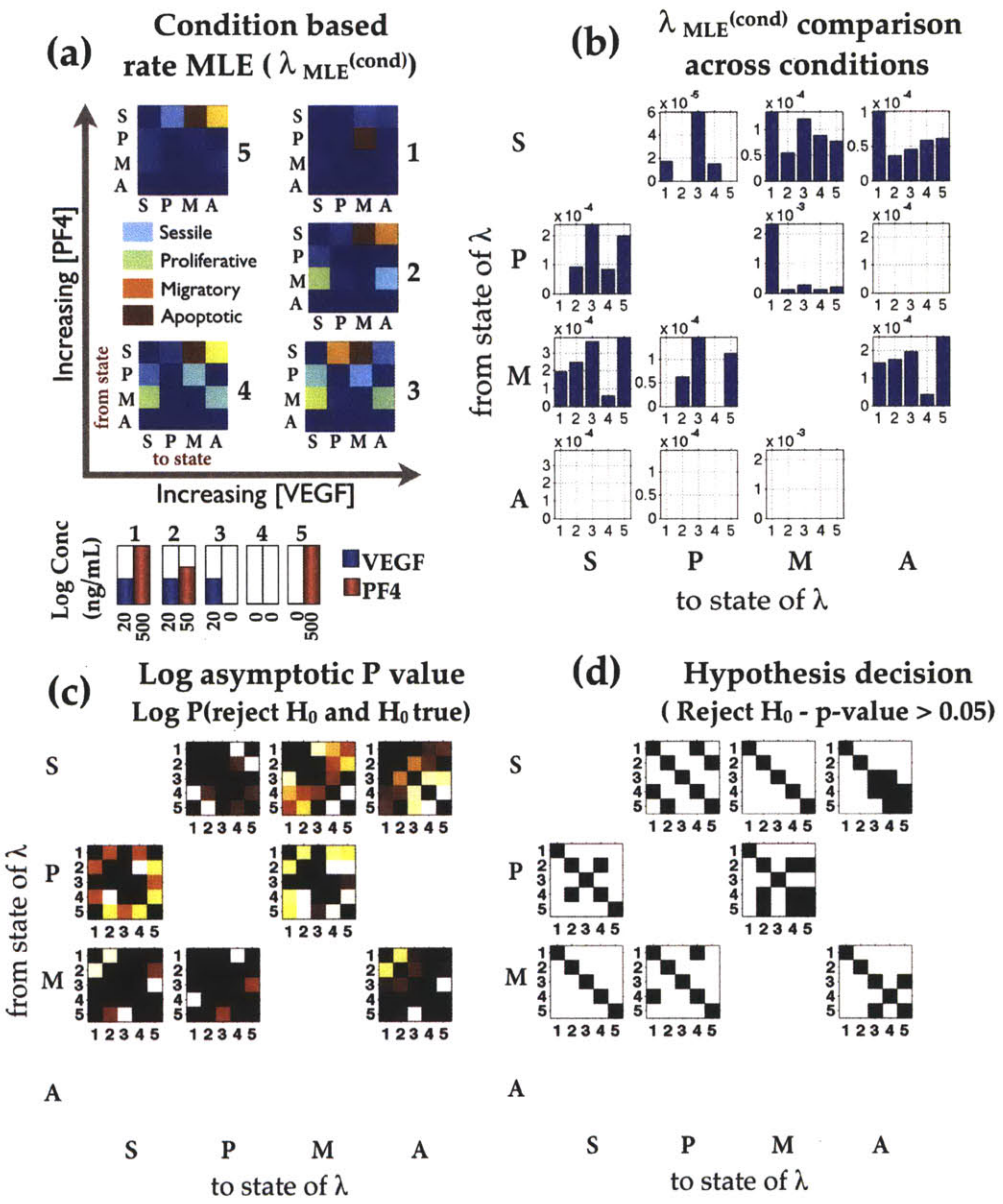

Figure 4-5: (a) Maximum likelihood estimates (MLEs) of transition rate matrices under different angiogenic and angiostatic cytokine treatment conditions. Under UPM, the condition base transition rate estimates ($\lambda^{(\text{cond})}$) were computed from the cell trajectories under each treatment condition separately. (b) Comparing $\lambda^{(\text{cond})}$ of each transition types across cytokine conditions. Each subplot presents rate MLEs of one transition types estimated from different cytokine conditions (labeled 1 - 5 and specified as in the condition indicator box (beneath Figure 4-5a)). The fourth bar in each subplot represents the no cytokine control condition. The effect of VEGF alone can be seen by comparing the 3$^{\text{rd}}$ to the 4$^{\text{th}}$ bars; the effect of PF4 alone: 5$^{\text{th}}$ to 4$^{\text{th}}$ bars; and the dosage effect of PF4 in the presence of VEGF: 3$^{\text{rd}}$, 2$^{\text{nd}}$, then 1$^{\text{st}}$ bars. Subplots are organized by the initial state of transition (row block) and the final state of transition (column block). (c and d) Statistical comparisons of the distributions of $\lambda^{(\text{cond})}$. Pairwise Komolgorov-Smirnov test (with Bonferroni correction) results indicate that in most cases, the cytokine-elicited changes are statistical significant. (c) Log asymptotic p-value of the pairwise comparisons under the null hypothesis that two distributions of $\lambda^{(\text{cond})}$ being compared are the same. (d) The hypothesis decision

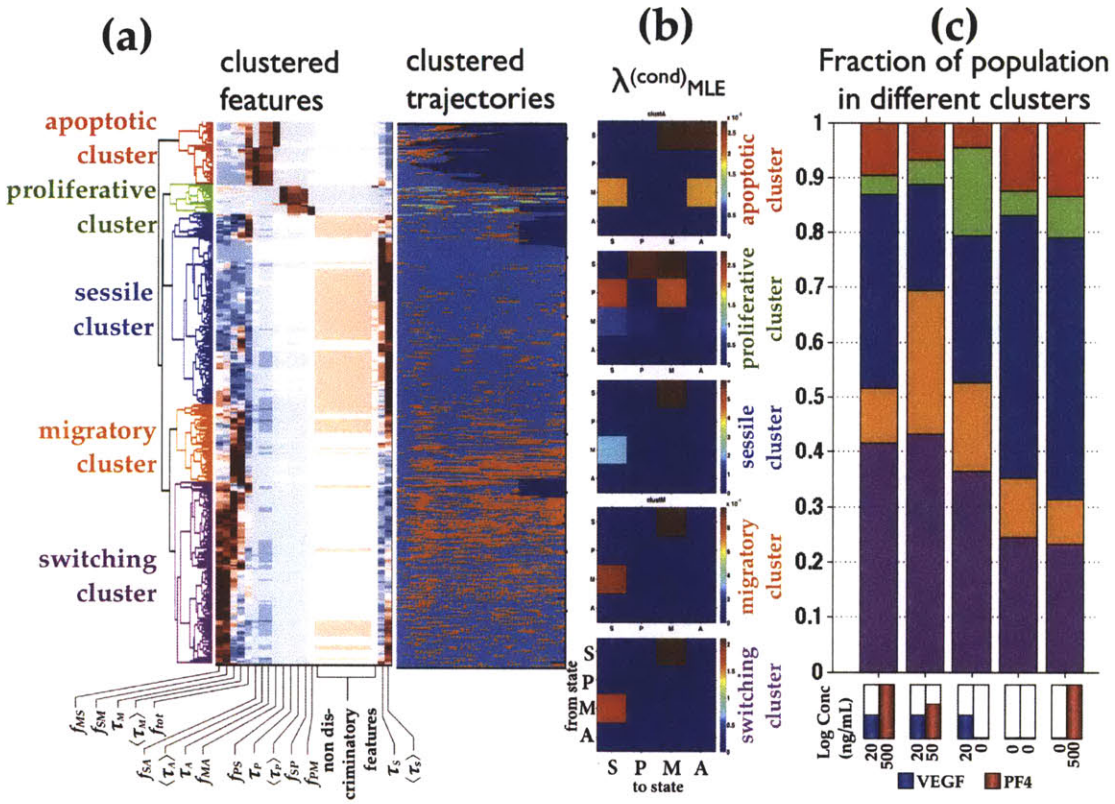

Figure 4-6: Hierarchical clustering of cell trajectories in all cytokine conditions reveals 3-5 identifiable clusters. (a) Dendrogram of the clustereHierarchical clustering of all cell trajectories in all cytokine conditions reveals 3-5 identifiable clusters. Hierarchical clustering was performed based on the trajectory features described in Table 2. (a) Dendrogram of the clustered features (left) and the corresponding clustered single cell trajectories (right). Clusters color labels are consistent from (a - c). (b) The corresponding transition rate MLEs computed from the single cell trajectories in each cluster separately $\lambda^{(\text{clust})}$. The transition rates matrices in sessile, migratory and switching clusters are qualitatively similar. Under DPM, the effect of cytokine treatment can described as changes in the fraction of cells adopting different dynamic phenotypic transition patterns (also referred to as cluster weights). The bar graph in (c) presents the fraction of cells in the population that adopts the five different state transition patterns identified by hierarchical clustering. The analysis consistent with DPM framework reveals that VEGF and PF4 directionally shifts the cluster weights (see text for details).

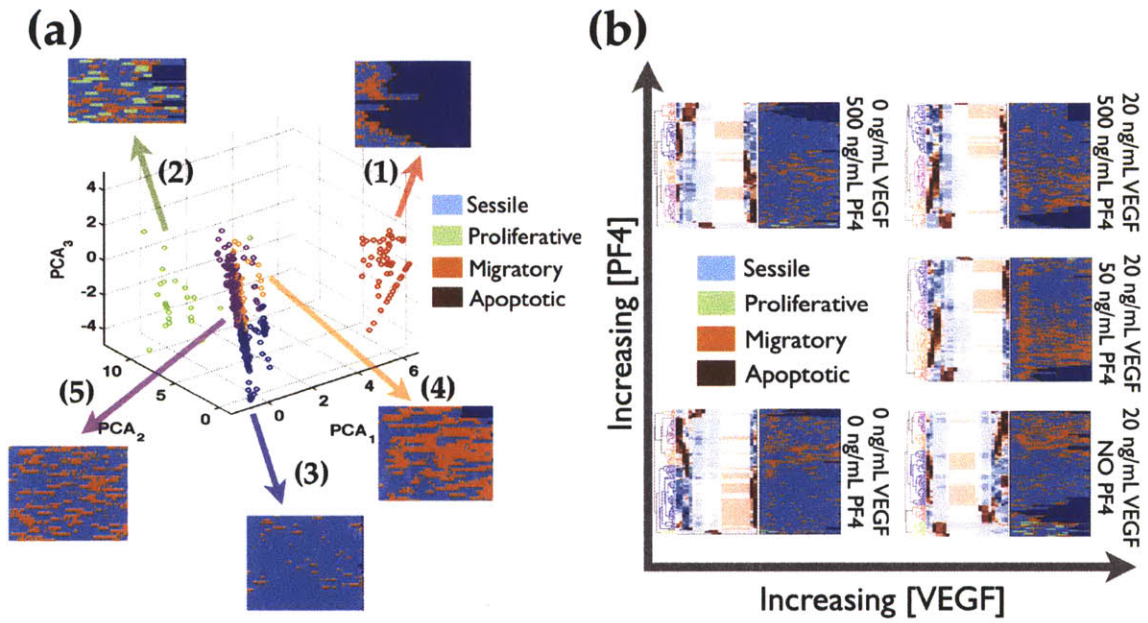

Figure 4-7: A three component principle component projections of the cell trajectories shows the separation of the endothelial subpopulations. The apoptotic and proliferative clusters (1 and 2) are well separated in state transition dynamics from each other and from the sessile, migratory, and switching clusters. Sessile, migratory and switching clusters (3, 4, 5) consist of cells that transition between sessile vs. motile states and are only differentiated by the frequencies of transition and the dwell times within the sessile vs. motile states. (b) Hierarchical clustering of cell trajectories in each cytokine condition exhibits similar cluster pattern with 3 - 5 identifiable clusters within each condition. Shown in each subfigures are clustered features with dendrogram(left) and clustered state labeled trajectories (right). The clustering pattern across different angiogenic/angiostatic cytokine combinations is consistent with the diverse population model (DPM).

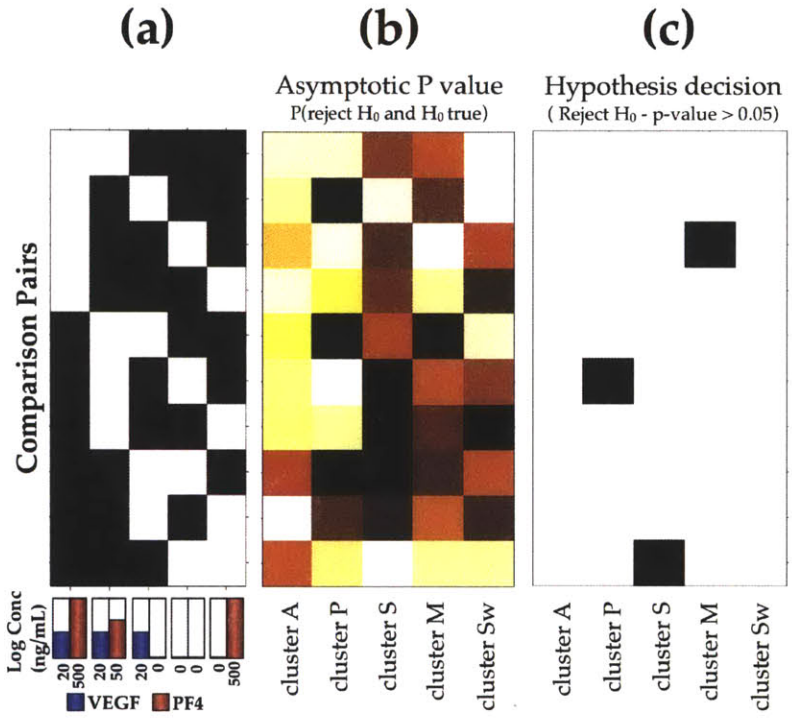

Figure 4-8: Statistical pairwise comparisons of the cluster weights across different cytokine conditions show that most of the cytokine elicited difference in the cluster weights are statistically significant. (d) Indicator matrix specifying the pairwise comparison. For example, the first row of (d) are true (white) for the first two conditions, indicating that the conditions being compared are conditions 1 and 2 (20 ng/mL VEGF with 500 ng/mL PF4 and 20 ng/mL VEGF with 50 ng/mL PF4, respectively). (e) Log of the asymptotic p-value (probability of mistakenly rejecting the null hypothesis). (f). The hypothesis decision based on the p-values indicating that most of the cytokine elicited changes are statistically significant.

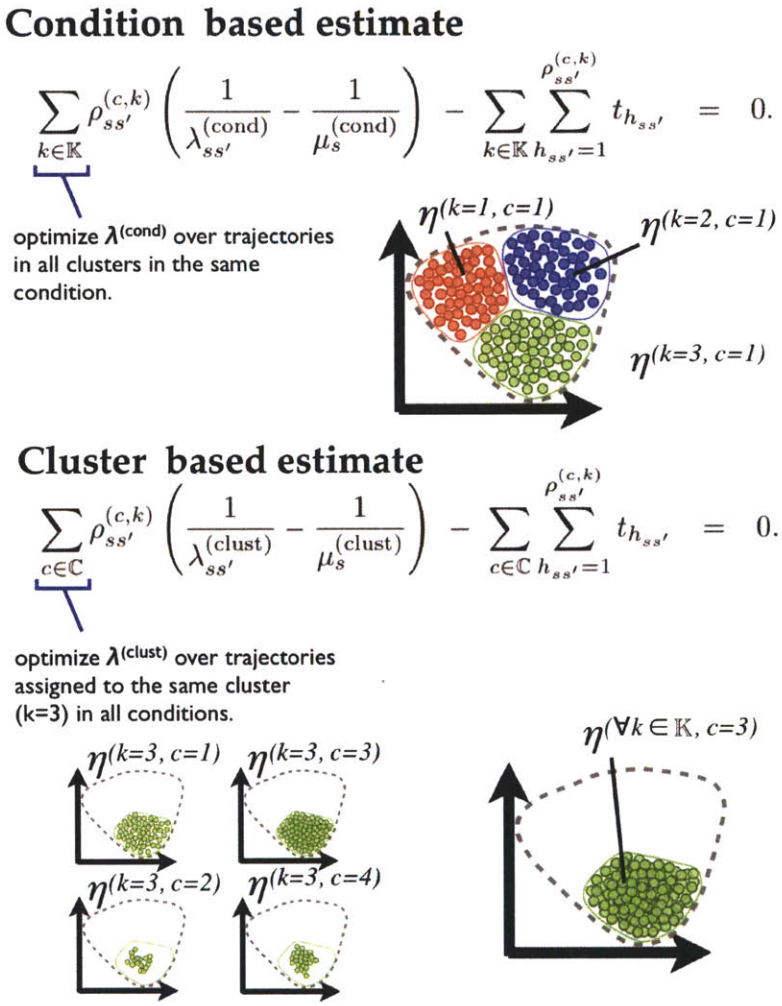

Figure 4-9: Condition based and cluster based estimates are computed over different sets of single cell trajectories. Condition based estimates are optimized over single cell trajectories taken from the same cytokine conditions, while cluster based estimates are optimized over trajectories taken from the same cluster.

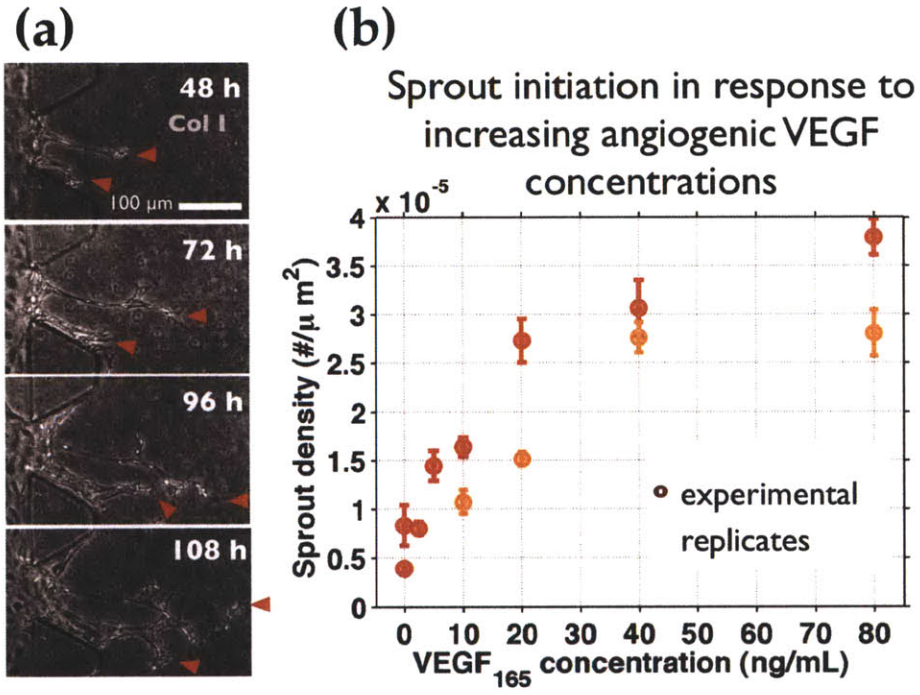

Supplementary Figure 1: Density of angiogenic sprout initiation (number of sprout per unit area of gel interface) is modulated by angiogenic factor stimulation and does not significantly change beyond 48 hrs of growth factor stimulation. (a)Long term angiogenic sprout extension without changes in sprout density over 5 days of growth factor stimulation. (b). Sprout density measured at 72 hours after stimulation with increasing concentration of $VEGF_{165}$.

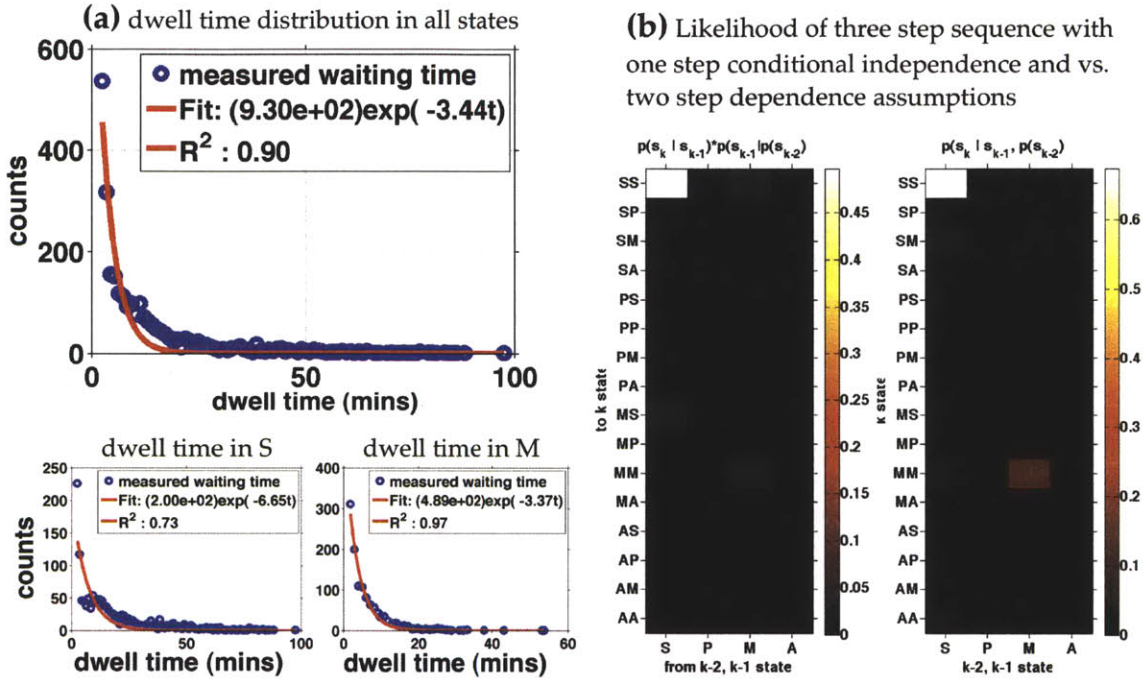

Supplementary Figure 2: State trajectory can be well approximated by the CTMC. (a) State trajectory waiting time distribution fits well to exponential distribution. (a). The dwell time distribution of in all states (S, P, M, A) can be well described by an exponential distribution with the coefficient of determination (R^s) of 0.90. (b) The distributions of dwell time in state S and M fit well to exponential distribution with R^2 of 0.73 and 0.97 respectively. Due to insufficient number of proliferative and apoptotic instances, the dwell time distribution in P and A states do not fit well to most well known statistical distributions. (b) Comparison of likelihood distributions under the one step condition independence assumption ()The state trajectory follow the conditional independence assumption (*left*) and no conditional independence assumption (*right*). Lack of significant difference between the two distribution indicates that the single cell trajectories follows CTM's conditional independence assumption.

Chapter 5

Perspectives on Future Work

Angiogenesis is the emergent behavior of a collective of endothelial and mural cells interacting with each other and with the extracellular matrix to produce vascular growth. This coordinated behavior results from a multitude of intracellular and extracellular signaling events, mechanical interactions, and mechanotransduction. These intricate subcellular processes lead to individual phenotypic cell decisions (such as whether to quiesce, migrate, proliferate, or apoptose) and to directed cell migration, which combine to create coordinated angiogenic growth. A tissue level manifestation of such cell decision process is the modulation of angiogenic sprouting in response to inflammatory angiogenesis presented in Chapter 2.

Computational approaches to model angiogenic process often require a large number of model parameters. Among these, the parameters describing cellular behaviors are the most difficult to infer from experimental data. Through the appreciation of such technical difficulty, the methods of inferring single cell decision parameters from aggregate headcount data in Chapter 3 and from full panel single cell trajectories in Chapter 4 were designed and implemented. In the case of aggregate data, the method was designed to be compatible with single cell markers of cellular states by quantitative flow cytometry. The limitations of the aggregate headcount parameter estimation method (especially in that the model relies on prior knowledge of how the number of cell in the population changes over time) inspired the development

of the live cell microscopy based method for full panel data collection in Chapter 4. From the live cell microscopic images, the full panel data collection method was investigated resulting in an optimized and refined contour tracking and automated state annotation. The contributions of this thesis to the field of single cell decision in endothelial cell is discussed below:

5.1 Summary

In Chapter 2, I demonstrated a physiologically relevant example of the tissue level changes in sprouting angiogenesis plausibly arising from changes in single cell decision. The physiological concentrations of opposing inflammatory cytokines VEGF and PF4 cause the tissue level changes including the dose dependent increase in sprout density, length, and diameter and cord dissociation in response to VEGF and the reversed changes in response to addition of PF4. VEGF and PF4 treatment also cause other dose dependent changes including VE-cadherin band thinning and cell shape. To this end, I hypothesize two potential mechanisms of how PF4 may interfere with VEGF-mediated sprouting angiogenesis and methods to test these hypotheses.

In Chapter 3, I discussed the development of algorithms for inferring single cell decision parameters from aggregate measurements of proliferation and apoptotic markers. More specifically, I derived the formal expressions for the maximum likelihood estimates (MLEs) and Bayesian inference (BI) of the single cell decision parameters based on the flow cytometry measurements. The parameter inference methods are applicable to the cases when the changes in number of cells over time is known.

To address the limitations of the aggregate data, I developed an experimental method to acquire a full panel single cell trajectories of endothelial cell population undergoing angiogenesis via live cell microscopy. Refinement of the method leads to the development of contour tracking and automated state annotation. The single

cell decisions in this dataset can be well model by a continuous time Markov chain (CTMC) as the single cell trajectories satisfy the exponential waiting time and conditional independence requirements. Based on CTMC, I formulated the inference algorithms for computing the maximum likelihood estimates of single cell state transition parameters, a key set of parameters determining cell behavior in the hybrid agent based model of sprouting angiogenesis developed in the Kamm lab.

This thesis offers an important stepping stone toward a more realistic integrative effort of modeling angiogenesis. The works described in this thesis suggest multiple improvements for the future directions in single cell decision and angiogenesis research, some of which are discussed below.

5.1.1 Lesson in algorithm design

The choice of algorithms, in this case, parameter inference methodology should be dictated by both the experimental methods and choice of single cell model in angiogenesis simulation. For the work in this thesis, we realize an experimental method and corresponding parameter inference algorithm is consistent with the continuous time Markov model. This parameter inference is amenable to direct application to the hybrid-agent based simulation developed in the Kamm lab.

The algorithm design based on these criteria is advantageous in many ways. First, given a consistent definitions of *phenotypic states* in the model and experiment, the cellular behavior in each *phenotypic state* in the simulations can be trained to represent the experimentally observed cell behaviors. For example, in experiment, the proliferative state is characterized by mother's cell contour duplication followed by antipodal movements of the daughther cell contours. This observation can be used to define proliferative cells' behavior in the simulation.

Given the consistent state definitions, the inferred state transition probabilities can be used directly in the agent based simulation. As such, experimental results specifi-

cally indicate which aspect of model assumption is not consistent with the model, thus providing specific suggestions of which model assumptions is inaccurate. In Chapter 4, we show that a population of ECs consists of subpopulations that adopt distinct transition dynamics and these dynamics persist across different cytokine conditions. These findings refute our original assumption that model parameters are unimodal and that cytokines directionally affect phenotypic transition parameters. These findings provide specific suggestion that the agent based simulations should be initialized as a mixture population of distinct phenotypic transition dynamics drawn from the experimentally observed mixture distribution.

5.2 Future outlook

The collaborative effort within the EFRI grant, of which this thesis is an integral part, has been to develop quantitatively predictive models at multiple granularities ranging cellular phenotypic response to signaling events, sprouting behaviors vs. phenotypic distribution, and geometric (diameter) response to sprouting elongation rate, among others. Development of a comprehensive modeling framework will be neither top-down nor bottom-up, but will equally integrate individual models from multiple scales, ranging from single cell signaling level to the level of multicellular sprouts. Models from each scale should be designed and tuned based on input-output data available for that scale. The behavior of higher scale models can be both interpreted in terms of the constituent lower scale models and validated by the corresponding input/output data. The validation of higher level model by the appropriate input/output data should provide constraints on the behavior of the lower level constituents and help address the potential mechanisms of the emerging patterns at least from a lower level model to the subsequent higher level behavior.

This thesis offers an important link between the tissue level studies of angiogenesis and the computational modeling. Angiogenesis modulators, be it cytokines,

small molecular inhibitors or biomechanical forces and fields take effect at the cellular level through receptor-ligand binding and activations of specific molecules on the cell membrane or inside the cells. Angiogenesis modulator-elicited signaling leads to *'emerging'* changes at multicellular scale in angiogenesis. In the past decades, the measurements of angiogenic modulators' effects have been performed across the entire cell population in terms of signaling protein phosphorylation and transcriptional changes. This is partly due to the ease of population-wide measurement over single cell measurements. We observe from tissue level response in angiogenesis that cell population is diverse. By following individual cells undergoing angiogenesis, we come across another manifestation of population heterogeneity in angiogenic population. By correlating the signaling measurements to phenotypic decision parameters instead and utilizing the agent based simulation to produce an expected tissue level result, the work in thesis provides a way of understanding the effects of angiogenesis modulators that respect the heterogeneity of angiogenic cell population. Several improvements can be made to enhance our understanding of angiogenesis. A few suggestions are discussed in below.

5.2.1 Quantitative correlation analysis of signaling to phenotypic decision

Given the availability of the signaling dataset and phenotypic decision parameters, one can build an empirical model to infer a relationship between the signaling dataset and the phenotypic response set. In our collaborative research program, the signaling data is acquired by quantitative mass spectrometry and phospho-protein luminex assays. The advantage of these highly multiplex approach is that a large number of targets can be detected all at once, turning the assay into a target discovery tool. Since the measurements are taken from the collection of lysate from the entire cell population, the signaling results may be useful mainly to narrow down the potential phospho-protein targets the activation of which is important in regulating the phenotypic

transition.

5.2.2 Measuring single cell intracellular signaling by live cell microscopy

The most optimal way to infer the influence of intracellular signaling on single cell decision is to acquire the single cell dynamics of signaling during the cell decision process. Signaling data in single cell along with morphology based phenotypic state identification allows inference of causal and/or correlative relationship between molecular changes some of which might govern the dynamics of single cell decision. Notably, single cell signaling measurements are valuable especially in the case when the cell population is heterogeneous.

In recent years, novel fluorescent resonant energy transfer (FRET) probes have been developed for microscopically detecting kinase[82, 7, 75] and GTPase [8] activations during signal transduction events. Real time live cell imaging of cells expressing these probes allows for simultaneous detection of selected signaling targets and phenotypic cell state. Since only a few differentially fluorescently labeled targets may be imaged simultaneously, a crucial question for performing such experiments is: what are the appropriate signaling targets governing the single cell decisions? To appropriately draw the causal relationship from the signaling and phenotypic state detection, one also need to ask what is the lag times between the signaling events and the influence it has on single cell decisions? To answer these questions, dedicated experiments may be for each of the selected signaling targets. To determine the *'appropriate'* signaling targets, one may start with a collection drawn from existing signaling databases of known signaling targets downstream of a signaling cue (growth factor) or associated with the specific cellular phenotypes or both. Multiplex population average signaling measurements (using phosphoproteomic techniques) can to be used to narrow down the list of potential targets. After then appropriate probes can be developed and tested for single cell imaging. To determine the lag time for

each signaling target, unstimulated (serum starved) single cell expressing the FRET probe can be imaged from prior to the signaling cue (stimulant) is added to after the phenotypic transition is detected.

5.2.3 Recording spatial information of decision making endothelial cells

The parameter estimation methods presented in this thesis assume that individual cells make *'independent'* decision, i.e., the state choice and the waiting time before a transition of one cell does not influence those of other cells in the population and *vice versa*. For the experiments reported in Chapter 4, endothelial cells are seeded as mixture of fluorescent (trackable) cells in the background of non-fluorescent cells. As such, the *'independent'* agent assumption may apply among the *'tracked'* cells in that dataset. However, there is no evidence against the possibility that neighboring cells surrounding a *'tracked'* cells influence the phenotypic state transitions. To determine whether there is such influence, one need to record the phenotypic state of individual cells and their spatial relationship (whether tracked cells are nearest neighbors at each time step) and how their phenotypic decisions are correlated.

5.2.4 Distinguishing tip and stalk cells and obtaining separate single cell tracking datasets

The parameter inference method framework can be applied to a wide range of problem involving single cell decision. However, a major limitation of this thesis work is that the collected single cell tracking dataset does not address how the *'tracked'* cells' phenotypic transitions maps to the tip vs. stalk states at the current or future time points. As such, one can argue that the quantitative result drawn from the current dataset does not directly enhance our understanding of sprouting angiogenesis.

To determine tip vs. stalk cell state, cells may be seeded in a 3D microfluidic sprouting assay, treated with angiogenesis modulating cytokines and imaged over the

period of sprout formation (at least 24 hours) by a confocal microscopy. To enhance the tip vs. stalk cell state identification, a tip vs. stalk cell enriched protein-fluorescent proteins (such as Delta-like 4 (DLL4), VEGFR3, and endothelial specific molecule-1 (ESM-1) [48, 102, 32, 100]) may be fused to flourescent protein and expressed in endothelial cells. While this approach is viable, acquiring sufficient number of cell tracks to build a dataset is technically challenging for two reasons. First, with the current 3D microfluidic design, the 3D confocal imaging of the device takes much longer scan time per region than 2D fluorescent imaging. Thus, the imaging throughput in 3D confocal based tracking might be significantly lower than 2D tracking. Second, small change in medium volume in microfluidic devices can result in large changes in cytokine concentration. Since microfluidic devices are designed to contain submilliliter volume, when subjected to live cell imaging in large environmental chamber over extended period of time, brief period of subsaturated vapor pressure causes evaporation of medium within the device that can result in significant change in cytokine concentrations.

5.2.5 Mapping stalk vs. tip state by modeling stalk-to-tip cell transition

An alternative method to map the phenotypic transition results to stalk vs. tip state of the cell are to acquire live cell imaging data of stalk and tip cell separately using different imaging setup. Four-dimensional tip cell images can be acquired after the tip cell selection and sprout tip invasion already begins, thereby reducing the number of imaging time and potential imaging volumes. On the other hand, by assuming that the stalk cell undergoes similar phenotypic decision as endothelial cells on Collagen gel, stalk cell images can be acquired using the on-gel setup. To link the tip to stalk cell state, one can model the tip-to-stalk transition as a stochastic process. Assuming that the transition is irreversible, then the transition may be well approximated by the Poisson arrival process. Poisson process can be described as a stochastic counting process in which the interval arrival times (the time between each pair of

consecutive events) follow an exponential distribution (memoryless property) with a rate parameter λ and each of these inter-arrival times is assumed to be independent of other inter-arrival times (independence property). The schematic of this alternative method of mapping tip and stalk cell state to phenotypic transition is shown in Figure 5-1.

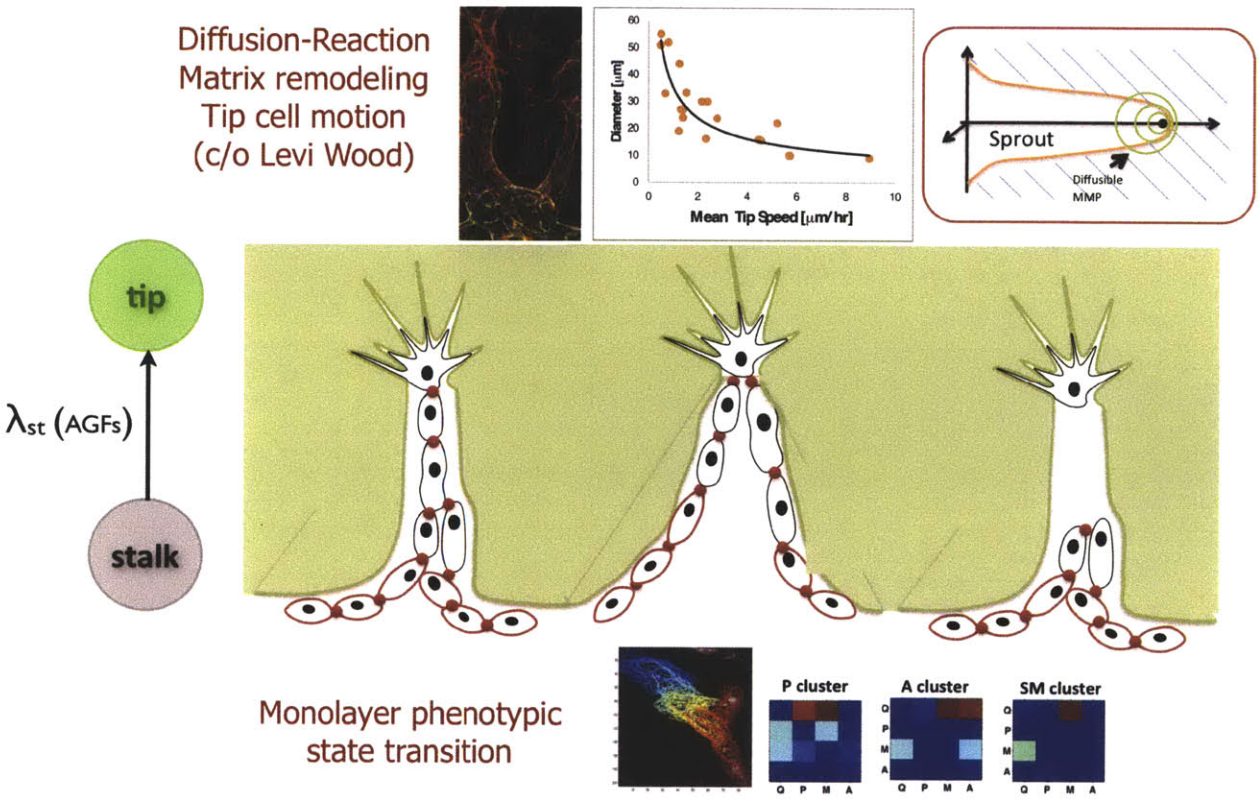

Figure 5-1: A schematic diagram of a method to map tip vs. stalk state of the cells to phenotypic transitions. Based on this method, tip and stalk cells are tracked separately after the stalk-to-transition has occurred. Since the tip and the stalk cells do not need to be imaged simultaneously, they can be tracked using appropriate imaging modalities that not only allows the acquisition of phenotypic transitions information, but also amenable to high throughput imaging. In this case, the tip cell can be imaged in 4D in microfludic devices and the stalk cells can be imaged using a on-gel invasion assay in which high throughput imaging can be performed. Stalk-to-tip transition can be modeled as a Poisson process described by a stalk-to-tip transition parameter (λ). This parameter can be inferred from the end point measurement of tip cell density in microfluidic device and on-gel sprouting assays.

Appendix A

Contour tracking methods

Level set methods have been widely used in image processing and computer vision. In this thesis the contour track methods are used in detecting the VECadherin bands in Chapter 2 and in contour tracking of live cell microscopy data in Chapter 4. Chan-vese algorithm is a region-based level set active contour algorithm for segmentation of static images.

A.1 Image preprocessing and time-series tracking

In contour tracking of the live cell images, the raw images are converted to from 16-bit to 8-bit to enhance the processing speed, then minimally enhanced to even out the cell-to-cell variations in brightness.

A.2 Contour initialization

The algorithm starts with the contour initialization the first image in the time-series is initialized in two ways.

- Initialization using intensity of the image
- Initialization using non-informative mask

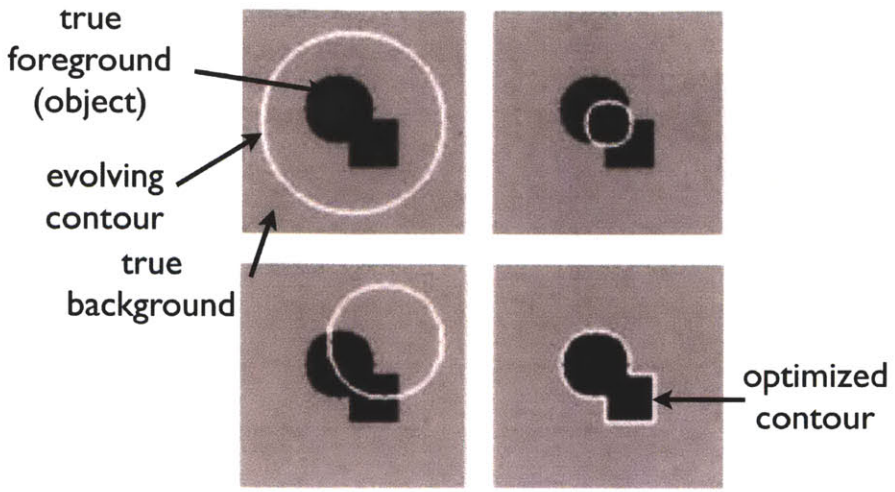

Figure A-1: Schematic drawing of Chan-Vese two phase active contour algorithm.

In most cases, the two methods of contour initialization yields reasonably good agreement (determined based on the square difference in the contour point coordinates). In rare case when the two methods do not yield similar contours, the image is enhanced and the contour is initialized using the intensity thresholded mask of the enhanced image.

For subsequent images, the detected contour of the immediate prior image is use to initialize contour in the contour finding routine. Given that in most of the time series images cells do not drastically change shape and size over one imaging interval, the detected contour from the prior image often serves as an appropriate initial contour.

A.3 Contour objective function and bias

In the traditional naive active contour algorithm, the objective function is defined by the gradient in image intensity alone. For single cell tracking application, however, the active contour's performance can be significantly improved by using the gradient in intensity and the detected contour of the neighboring images in the time series to bias the contour's objective function.

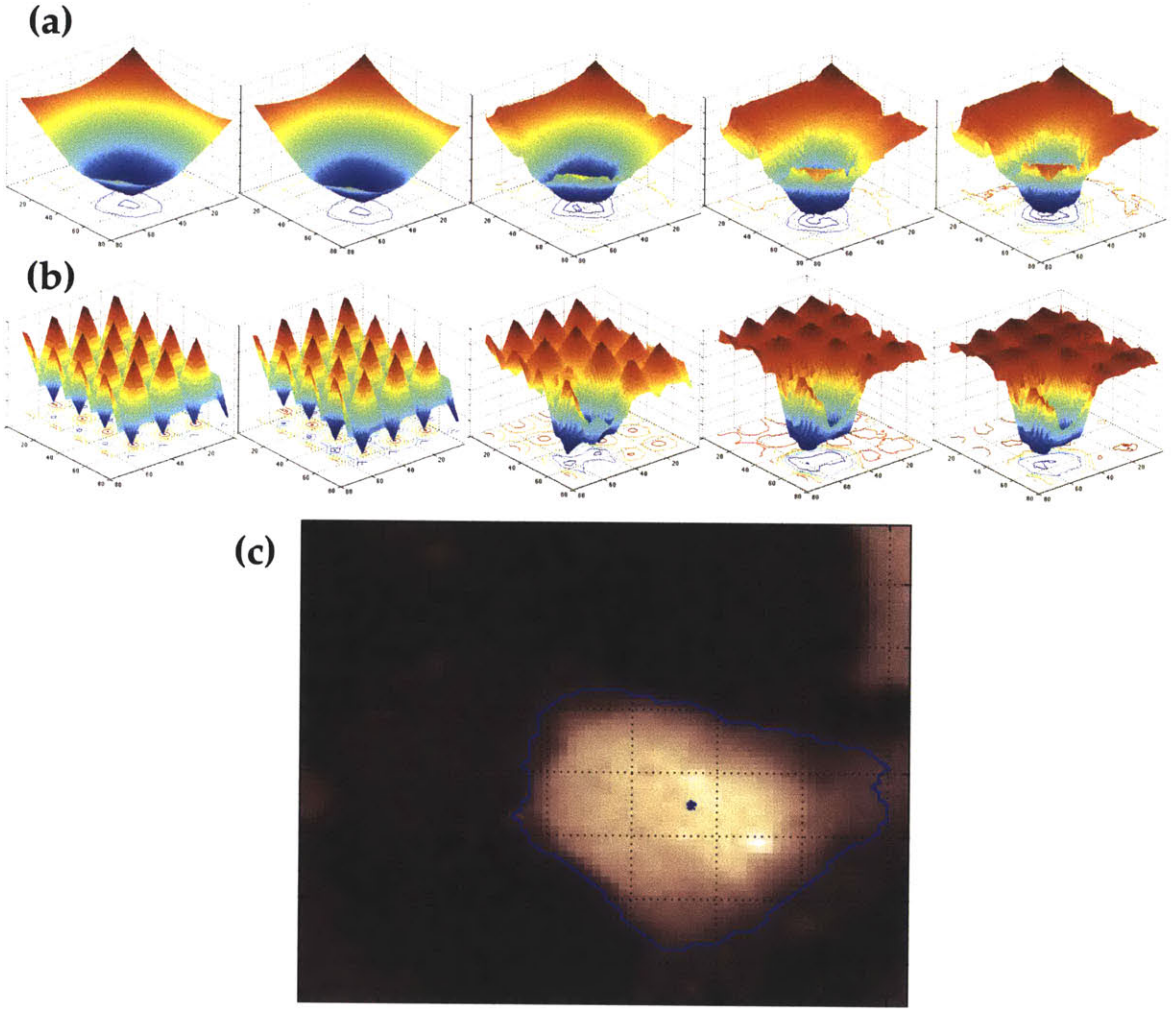

Figure A-2: Convergence of contour finding algorithms using the two methods of contour initialization. Evolution of the level set surfaces during the runs of level set based contour finding algorithms (a) using the intensity of the image to initialize the contour and (b) using randomly initialized contour.

Appendix B

Microfluidic device protocol

B.1 High throughput microfluidic device (HTD) preparation

Material

- PDMS Body liquid (10 parts)
- PDMS curing agent (1 part)
- Negative pattern wafer
- Microscope slides (1mm thick)

Procedure

PDMS Mixture Preparation

1. Pour body liquid in a plastic cup while measuring its weight (Make sure to cover the balance with tissue)
2. Reset scale, pour curing agent while measuring its weight
3. Stir the mixture

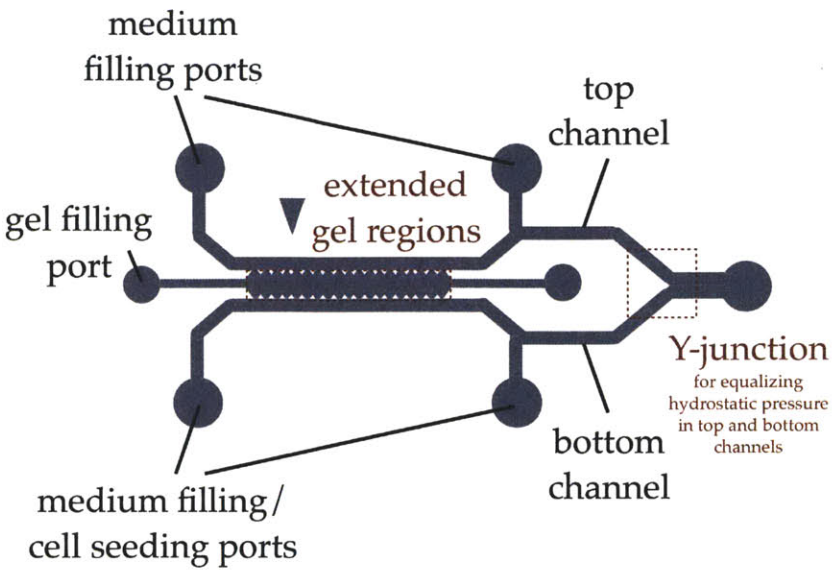

Figure B-1: Schematic drawing of the high throughput microfluidic [?].

4. Remove the bubbles in the vacuum chamber

5. Turn on vacuum and close the valve for sustaining vacuum (Make sure to cover the chamber with tissue)

6. Degas for 20 minutes

PDMS Pouring

1. Blow the wafers with air, clear of all debris

2. Pour the PDMS onto the wafers. Make sure there is enough PDMS to completely fill the hole cut in the old PDMS and does not form a meniscus. Note that any devices that are not perfectly flat on top cannot be used with a syringe pump.

3. Let PDMS on wafer stand for 15 - 30 minutes, then blow air bubbles that have risen to the surface and put in oven. Do NOT degas wafer. This has lead to cracking and we only have the one.

PDMS Baking

1. Bake the poured wafers for 4-8 hours at 80°C (recommended: 24hours to cross-link most of PDMS monomers)

2. Detach by cutting with razor (carefully and slowly peel it off, starting from the edges and going in the circumferential direction, in order to avoid tearing posts apart)

PDMS-Device punching

1. Cut devices apart using a razor and the outline on the mask. Punch 4 mm holes in the cell seeding and reservoir ports, a 2 mm hole in the outlet port, and use the syringe to punch the gel filling ports.

2. Clean devices with transparent tape. Its better to punch the devices off of the paper covered acrylic because the paper makes the devices very dirty.

3. Put devices in beaker with DI water, autoclave (wet / dry, 20 / 10 minutes)

4. Remove devices from beaker and place devices in empty pipette tip box, up to 6 per box.

5. Autoclave again in box (switch setting to dry)

6. Dry in oven overnight at 80°C.

PDMS Device Bonding and PDL coating

1. Plasma treatment

2. Clean area and all tools with ethanol

3. Place one device and one coverslip per platform, up to 3 platforms

4. Close the door and valve, confirm seal, and turn on vacuum (*"Pump* switch) for 20 seconds.

5. **1 minute and 40 second plasma treatment:** Turn *"Power* switch on, turn radiation dial to low, medium, then high. After observing a purple glow, slowly open the valve (*fractions of a turn!*) until the glow becomes bright.

6. Bring the devices and glass into contact with tweezers. Apply firm pressure with your fingers from one side to the other, avoiding air gaps between the coverslip and the device. PDL coating

7. Fill the devices with PDL (100-150 μL/device)

8. Wash twice with water after 24 hours. Make sure that all regions are washed, in order to avoid heterogeneous surface coating. If you get bubbles, try to remove them by using the pipette applying suction.

B.2 ECM injection and cell seeding

Material

- PDL-coated microfluidic devices
- Collagen Gel
- Complete Medium

Procedure

1. After PDL coating/drying, let the devices cool down for 30 minutes-1 hour at room temperature.

2. Prepare collagen gel.

3. Draw 30μL of gel with the 200μL pipetter. Fill device from gel filling port. Fill gel most of the way from one port, but not all the way to the other gel filling port. Then, fill from the other port until gel interfaces merge. This will leave an inconsistent gel interface, but we do not have an option at this point.

4. Place each gel-filled device with the PDMS side facing up in the humidity box after it has been filled to avoid dryout.

5. Leave all devices for 1 hour in the incubator (in the humidity box) for the gel to polymerize.

6. Fill channels with medium from reservoir ports (50-100μL). Gently fill medium until the channels have been filled to the cell seeding filling ports. Do NOT fill all the way to the outlet port. Instead, be sure to leave air at the channel intersection and in the outlet port. Place a droplet of medium over the outlet port to trap the air inside. Place devices in incubator. They will be ready for cell seeding in 24hours.

Cell Seeding

1. Gently aspirate medium from all reservoirs and cell seeding ports all the way to the glass. Make sure that the suction tip is away from the channel, so that the channel is not dried out.

2. Add 20 μL of medium to the reservoir and cell seeding ports on the top channel.(This reduces the interstitial flow rate so that not too many cells are bunched up on the gel.)

3. Seed 40 μL of a 2×10^6 cells/mL cell suspension into the bottom channel.

4. Let cells adhere by placing devices in the incubator for 1.5 - 2 hours and then gently aspirate medium from all reservoirs and cell seeding ports.

5. Place large droplets of medium on the reservoir ports. Return devices to incubator.

6. Maintain devices with complete medium for 24 hours. After 24 hours, apply condition medium.

B.3 Immunofluorescent protocol for *in situ* staining and imaging

Material

- Microfluidic devices to be stained
- Fixative: 4% paraformaldehyde (PFA)
- Permeabilizing agent: 0.1% Triton-X/PBS
- Blocking buffer: 5% bovine serum albumin (BSA), 3% goat serum (gS) in PBS
- Wash buffer: 0.5% BSA in PBS
- Primary and secondary antibodies
- Counter stains: DAPI and Phalloidin

Sample Preparation and Fixation (20 minutes):

1. Wash live sample with sterile 1xPBS.
2. Fix sample by adding 4% PFA.
3. Incubate 15 minutes at room temperature (RT).
4. Wash with 1xPBS.
5. Fixed samples can be kept in PBS at 4°C for an extended period of time.

Staining: Day 1

Reagent preparation

1. Prepare blocking buffer(BB) and wash buffer(WB). Blocking buffer and wash buffer can be prepared ahead of time and keep at 4°C for one week.

2. Solubilize cells (10 mins)

3. Permeabiize sample by adding 0.1 % Triton-X

4. Incubate 10 minutes at RT

Blocking ($\geq$ 1 hour)

1. Prepare blocking solution: 5% BSA/PBS + 3% goat serum.

2. Add 300 μL of blocking buffer to each device.

3. Let incubate at least 1 hour at RT

Primary antibody staining (overnight)

1. Prepare primary antibody solution by diluting in Wash buffer (0.5% BSA/PBS).

2. Add 300 μL primary antibody solution per device.

3. Incubate devices overnight at 4°C in humidified dishes.

Staining: Day 2

Secondary Ab staining (> 2 hr)

1. Prepare secondary Ab, diluted in WB.

2. Wash 5 times with WB. Incubate 5 minutes each time.

3. Add secondary Ab solution.

4. Incubate at RT > 2 hours.

Counter staining (1 hour)

1. Prepare counter staining solution (DAPI + Phalloidin)

2. Wash 3 times with Wash buffer. Incubate 5 minutes each time.

3. Add counter stain solution.

4. Incubate over night at 4°C or 30 - 60 minutes at RT.

5. Wash 3 times with Wash buffer. Incubate 5 minutes each time.

6. Rinse 2 times with PBS.

Sample Storage:

If not imaged immediately, samples should be kept in PBS and store at 4°C and protect from light. Stained samples should not be kept longer than 3 weeks.

Bibliography

[1] J Abonyi and B Balasko. Fuzzy clustering and data analysis toolbox, 2006. (document), 3-2

[2] Sabu Abraham, Margaret Yeo, Mercedes Montero-Balaguer, Hugh Paterson, Elisabetta Dejana, Christopher J Marshall, and Georgia Mavria. VE-Cadherin-mediated cell-cell interaction suppresses sprouting via signaling to MLC2 phosphorylation. *Current biology : CB*, 19(8):668–674, April 2009. 2.4.3

[3] Murat Acar, Jerome T Mettetal, and Alexander van Oudenaarden. Stochastic switching as a survival strategy in fluctuating environments. *Nature genetics*, 40(4):471–475, April 2008. 3.2.1

[4] Ralf H Adams and Kari Alitalo. Molecular regulation of angiogenesis and lymphangiogenesis. *Nature Reviews Molecular Cell Biology*, 8(6):464–478, June 2007. 1

[5] S Amari. Methods of information geometry, 2007. 2

[6] A R Anderson and M A Chaplain. Continuous and discrete mathematical models of tumor-induced angiogenesis. *Bulletin of Mathematical Biology*, 60(5):857–899, September 1998. 1.3

[7] Kazuhiro Aoki, Etsuko Kiyokawa, Takeshi Nakamura, and Michiyuki Matsuda. Visualization of growth signal transduction cascades in living cells with genetically encoded probes based on Förster resonance energy transfer. *Philosophical transactions of the Royal Society of London. Series B, Biological sciences*, 363(1500):2143–2151, June 2008. 5.2.2

[8] Kazuhiro Aoki and Michiyuki Matsuda. Visualization of small GTPase activity with fluorescence resonance energy transfer-based biosensors. *Nature Protocols*, 4(11):1623–1631, 2009. 5.2.2

[9] A APLIN, E FOGEL, P ZORZI, and R NICOSIA. Chapter 7 The Aortic Ring Model of Angiogenesis. *Methods in Enzymology*, 443:119–136, 2008. (document), 1.2.1, 1-1

[10] Irina Arnaoutova and Hynda K Kleinman. In vitro angiogenesis: endothelial cell tube formation on gelled basement membrane extract. *Nature Protocols*, 5(4):628–635, March 2010. 1.2.1

[11] J Asai, H Takenaka, KF Kusano, and M Ii. Topical Sonic Hedgehog Gene Therapy Accelerates Wound Healing in Diabetes by Enhancing Endothelial Progenitor Cell–Mediated Microvascular Remodeling. *Circulation*, 2006. 2.2.1

[12] Rebecca G Bagley, Jennifer Walter-Yohrling, Xiaohong Cao, William Weber, Betsy Simons, Brian P Cook, Scott D Chartrand, Clarence Wang, Stephen L Madden, and Beverly A Teicher. Endothelial precursor cells as a model of tumor endothelium: characterization and comparison with mature endothelial cells. *Cancer Research*, 63(18):5866–5873, September 2003. 1.2.1

[13] Nathalie Q Balaban, Jack Merrin, Remy Chait, Lukasz Kowalik, and Stanislas Leibler. Bacterial persistence as a phenotypic switch. *Science*, 305(5690):1622–1625, September 2004. 3.2.1

[14] Stephan Barrientos, Olivera Stojadinovic, Michael S Golinko, Harold Brem, and Marjana Tomic-Canic. PERSPECTIVE ARTICLE: Growth factors and cytokines in wound healing. *Wound Repair and Regeneration*, 16(5):585–601, September 2008. 2.2.1

[15] Kayla J Bayless, Hyeong-Il Kwak, and Shih-Chi Su. Investigating endothelial invasion and sprouting behavior in three-dimensional collagen matrices. *Nature Protocols*, 4(12):1888–1898, December 2009. (document), 1.2.1, 1-4, 4.3.1

[16] R Benelli. In vitro models of angiogenesis: ... [Int J Biol Markers. 1999 Oct-Dec] - PubMed - NCBI. *The International journal of biological markers*, 1999. 1.2.1

[17] Katie Bentley, Holger Gerhardt, and Paul A Bates. Agent-based simulation of notch-mediated tip cell selection in angiogenic sprout initialisation. *Journal of Theoretical Biology*, 250(1):25–36, January 2008. 1.4

[18] Katie Bentley, Giovanni Mariggi, Holger Gerhardt, and Paul A Bates. Tipping the balance: robustness of tip cell selection, migration and fusion in angiogenesis. *PLoS Computational Biology*, 5(10):e1000549, October 2009. 1.4

[19] Gabriele Bergers and Laura E Benjamin. Angiogenesis: Tumorigenesis and the angiogenic switch. *NATURE REVIEWS CANCER*, 3(6):401–410, June 2003. 4.3.1

[20] Ludwik K Branski, Gerd G Gauglitz, David N Herndon, and Marc G Jeschke. A review of gene and stem cell therapy in cutaneous wound healing. *Burns : journal of the International Society for Burn Injuries*, 35(2):171–180, March 2009. 2.1, 2.2.1

[21] Peter Carmeliet. Angiogenesis in life, disease and medicine. *Nature Cell Biology*, 438(7070):932–936, December 2005. 1, 4.3.1

[22] Peter Carmeliet and Rakesh K Jain. Molecular mechanisms and clinical applications of angiogenesis. *Nature*, 473(7347):298–307, May 2011. 1

[23] M Chatterjee, Z Huang, W Zhang, L Jiang, K Hultenby, L Zhu, H Hu, G P Nilsson, and N Li. Distinct platelet packaging, release, and surface expression of proangiogenic and antiangiogenic factors on different platelet stimuli. *Blood*, 117(14):3907–3911, April 2011. 2.2.2, 2.5, 4.3.4

[24] C H Cho. COMP-angiopoietin-1 promotes wound healing through enhanced angiogenesis, lymphangiogenesis, and blood flow in a diabetic mouse model. *Proceedings of the National Academy of Sciences*, 103(13):4946–4951, March 2006. 2.2.1

[25] Bong Geun Chung and Jaebum Choo. Microfluidic gradient platforms for controlling cellular behavior. *Electrophoresis*, 31(18):3014–3027, September 2010. 1.2.1

[26] S Chung, R Sudo, and V Vickerman. SpringerLink - Annals of Biomedical Engineering, Volume 38, Number 3. *Annals of biomedical ...*, 2010. 2.3.3

[27] Seok Chung, Ryo Sudo, Peter J Mack, Chen-Rei Wan, Vernella Vickerman, and Roger D Kamm. Cell migration into scaffolds under co-culture conditions in a microfluidic platform. *Lab on a Chip*, 9(2):269–275, 2009. (document), 1.2.1, 1-6

[28] Seok Chung, Ryo Sudo, Ioannis K Zervantonakis, Tharathorn Rimchala, and Roger D Kamm. Surface-Treatment-Induced Three-Dimensional Capillary Morphogenesis in a Microfluidic Platform. *Advanced Materials*, 21(47):4863–4867, August 2009. (document), 1.2.1, 2-2, 2.3.3

[29] Judith A Coppinger, Gerard Cagney, Sinead Toomey, Thomas Kislinger, Orina Belton, James P McRedmond, Dolores J Cahill, Andrew Emili, Desmond J Fitzgerald, and Patricia B Maguire. Characterization of the proteins released from activated platelets leads to localization of novel platelet proteins in human atherosclerotic lesions. *Blood*, 103(6):2096–2104, March 2004. 2.2.1

[30] Anusuya Das, Douglas Lauffenburger, Harry Asada, and Roger D Kamm. A hybrid continuum-discrete modelling approach to predict and control angiogenesis: analysis of combinatorial growth factor and matrix effects on vessel-sprouting morphology. *Philosophical transactions. Series A, Mathematical, physical, and engineering sciences*, 368(1921):2937–2960, June 2010. 1.3, 1.4, 4.4.1

[31] Dipak Datta, Pallavi Banerjee, Martin Gasser, Ana Maria Waaga-Gasser, and Soumitro Pal. CXCR3-B can mediate growth-inhibitory signals in human renal cancer cells by down-regulating the expression of heme oxygenase-1. *Journal of Biological Chemistry*, 285(47):36842–36848, November 2010. 2.4.4

[32] Raquel del Toro, Claudia Prahst, Thomas Mathivet, Geraldine Siegfried, Joshua S Kaminker, Bruno Larrivee, Christiane Bréant, Antonio Duarte,

Nobuyuki Takakura, Akiyoshi Fukamizu, Josef Penninger, and Anne Eichmann. Identification and functional analysis of endothelial tip cell-enriched genes. *Blood*, 116(19):4025–4033, November 2010. 5.2.4

[33] M Dobryansky, RD Galiano, and KA Bhatt. Topical vascular endothelial growth factor reverses delayed wound healing secondary to angiogenesis inhibitor administration - Michaels - 2005 - Wound Repair and Regeneration - Wiley Online Library. *Wound repair and ...*, 2005. 2.2.1

[34] MB Elowitz, MG Surette, and PE Wolf. Protein Mobility in the Cytoplasm ofEscherichia coli. *Journal of ...*, 1999. 1.3

[35] N Ferrara. Vascular endothelial growth factor: basic science and clinical progress. *Endocrine reviews*, 2004. 2.2.2

[36] N Ferrara, K HOUCK, and LYN Jakeman. Molecular and biological properties of the vascular endothelial growth factor family of proteins. *Endocrine ...*, 1992. 2.2.2

[37] J Folkman and CC Haudenschild. Long-term culture of capillary endothelial cells. In *Proceedings of the ...*, 1979. 4.4

[38] Judah Folkman. Angiogenesis: an organizing principle for drug discovery? *Nature reviews. Drug discovery*, 6(4):273–286, April 2007. 1

[39] P.S. Frenette and D.D. Wagner. Adhesion molecules. *New England Journal of Medicine*, 334(23):1526–1529, 1996. (document), 2-1

[40] Mitsuko Furuya, Tomona Yoneyama, Etsuko Miyagi, Reiko Tanaka, Kiyotaka Nagahama, Yohei Miyagi, Yoji Nagashima, Fumiki Hirahara, Yoshiaki Inayama, and Ichiro Aoki. Differential expression patterns of CXCR3 variants and corresponding CXC chemokines in clear cell ovarian cancers and endometriosis. *Gynecologic oncology*, 122(3):648–655, September 2011. 2.4.4

[41] H P Gerber, V Dixit, and N Ferrara. Vascular endothelial growth factor induces expression of the antiapoptotic proteins Bcl-2 and A1 in vascular endothelial cells. *The Journal of biological chemistry*, 273(21):13313–13316, May 1998. 2.2.2

[42] Holger Gerhardt, Matthew Golding, Marcus Fruttiger, Christiana Ruhrberg, Andrea Lundkvist, Alexandra Abramsson, Michael Jeltsch, Christopher Mitchell, Kari Alitalo, David Shima, and Christer Betsholtz. VEGF guides angiogenic sprouting utilizing endothelial tip cell filopodia. *The Journal of Cell Biology*, 161(6):1163–1177, June 2003. (document), 1, 1.2.1, 1-2

[43] James Glazier and François Graner. Simulation of the differential adhesion driven rearrangement of biological cells. *Physical Review E*, 47(3):2128–2154, March 1993. 1.3

[44] DS Grant, JL Kinsella, and MC Kibbey. Matrigel induces thymosin beta 4 gene in differentiating endothelial cells. *Journal of cell ...*, 1995. 1.2.1

[45] AD Grove, VV Prabhu, BL Young, and FC Lee. Both Protein Activation and Gene Expression Are Involved in Early Vascular Tube Formation in Vitro. *Clinical cancer ...*, 2002. 1.2.1

[46] Wei Gu, Xiaoyue Zhu, Nobuyuki Futai, Brenda S Cho, and Shuichi Takayama. Computerized microfluidic cell culture using elastomeric channels and Braille displays. *Proceedings of the National Academy of Sciences of the United States of America*, 101(45):15861–15866, November 2004. 1.2.1

[47] Geoffrey C Gurtner, Sabine Werner, Yann Barrandon, and Michael T Longaker. Wound repair and regeneration. *Nature*, 453(7193):314–321, May 2008. 2.1, 2.2.1

[48] Mats Hellström, Li-Kun Phng, Jennifer J Hofmann, Elisabet Wallgard, Leigh Coultas, Per Lindblom, Jackelyn Alva, Ann-Katrin Nilsson, Linda Karlsson, Nicholas Gaiano, Keejung Yoon, Janet Rossant, M Luisa Iruela-Arispe, Mattias Kalén, Holger Gerhardt, and Christer Betsholtz. Dll4 signalling through Notch1 regulates formation of tip cells during angiogenesis. *Nature*, 445(7129):776–780, February 2007. 5.2.4

[49] Cosmina S Hogea, Bruce T Murray, and James A Sethian. Simulating complex tumor dynamics from avascular to vascular growth using a general level-set method. *Journal of mathematical biology*, 53(1):86–134, July 2006. 1.3

[50] H Hutchings. Extracellular matrix-bound vascular endothelial growth factor promotes endothelial cell adhesion, migration, and survival through integrin ligation. *The FASEB Journal*, June 2003. 4.3.4

[51] J E Italiano, J L Richardson, S Patel-Hett, E Battinelli, A Zaslavsky, S Short, S Ryeom, J Folkman, and G L Klement. Angiogenesis is regulated by a novel mechanism: pro- and antiangiogenic proteins are organized into separate platelet granules and differentially released. *Blood*, 111(3):1227–1233, October 2007. 2.5, 4.3.4

[52] Lars Jakobsson, Claudio A Franco, Katie Bentley, Russell T Collins, Bas Ponsioen, Irene M Aspalter, Ian Rosewell, Marta Busse, Gavin Thurston, Alexander Medvinsky, Stefan Schulte-Merker, and Holger Gerhardt. Endothelial cells dynamically compete for the tip cell position during angiogenic sprouting. *Nature Cell Biology*, 12(10):943–953, October 2010. 1.4

[53] Gi Seok Jeong, Sewoon Han, Yoojin Shin, Gu Han Kwon, Roger D Kamm, Sang-Hoon Lee, and Seok Chung. Sprouting Angiogenesis under a Chemical Gradient Regulated by Interactions with an Endothelial Monolayer in a Microfluidic Platform. *Analytical Chemistry*, 83(22):8454–8459, November 2011. 1.2.1

[54] Jeffrey Kamykowski, Peter Carlton, Siddharth Sehgal, and Brian Storrie. Quantitative immunofluorescence mapping reveals little functional coclustering of proteins within platelet -granules. *Blood*, 118(5):1370–1373, August 2011. 2.5

[55] Brigitte Kasper and Frank Petersen. Molecular pathways of platelet factor 4/CXCL4 signaling. *European Journal of Cell Biology*, 90(6-7):521–526, February 2011. 4.3.4

[56] Cheen Peen Khoo, Kingsley Micklem, and Suzanne M Watt. A comparison of methods for quantifying angiogenesis in the Matrigel assay in vitro. *Tissue engineering. Part C, Methods*, 17(9):895–906, September 2011. (document), 1-3

[57] F Kiefer. The role of chemokines and their receptors in angiogenesis. *Cellular and molecular life sciences*, 2011. 2.4.4

[58] Mohit Kumar, Mario S Mommer, and Victor Sourjik. Mobility of cytoplasmic, membrane, and DNA-binding proteins in Escherichia coli. *Biophysical Journal*, 98(4):552–559, February 2010. 1.3

[59] Daniel R Larson, Daniel Zenklusen, Bin Wu, Jeffrey A Chao, and Robert H Singer. Real-time observation of transcription initiation and elongation on an endogenous yeast gene. *Science*, 332(6028):475–478, April 2011. 1.3

[60] L Lasagni, M Francalanci, F Annunziato, E Lazzeri, S Giannini, L Cosmi, C Sagrinati, B Mazzinghi, C Orlando, E Maggi, F Marra, S Romagnani, M Serio, and P Romagnani. An Alternatively Spliced Variant of CXCR3 Mediates the Inhibition of Endothelial Cell Growth Induced by IP-10, Mig, and I-TAC, and Acts as Functional Receptor for Platelet Factor 4. *Journal of Experimental Medicine*, 197(11):1537–1549, June 2003. 2.4.4, 4.3.4

[61] S Lee, TT Chen, CL Barber, and MC Jordan. Autocrine VEGF signaling is required for vascular homeostasis. *Cell*, 2007. 2.2.2

[62] Eric Libby and Paul B Rainey. Exclusion rules, bottlenecks and the evolution of stochastic phenotype switching. *Proceedings. Biological sciences / The Royal Society*, 278(1724):3574–3583, December 2011. 3.2.1

[63] Edison T Liu and Douglas A Lauffenburger. *Systems biomedicine*. Academic Press, August 2009. 1.3

[64] Gang Liu, Amina A Qutub, Prakash Vempati, Feilim Mac Gabhann, and Aleksander S Popel. Module-based multiscale simulation of angiogenesis in skeletal muscle. *Theoretical biology & medical modelling*, 8:6, 2011. 1.3

[65] Jason W Locasale. Signal duration and the time scale dependence of signal integration in biochemical pathways. *BMC Systems Biology*, 2:108, 2008. 1.3

[66] R Losick and C Desplan. Stochasticity and Cell Fate. *Science*, 320(5872):65–68, April 2008. 3.2.1

[67] A D Luster. The IP-10 chemokine binds to a specific cell surface heparan sulfate site shared with platelet factor 4 and inhibits endothelial cell proliferation. *Journal of Experimental Medicine*, 182(1):219–231, July 1995. 2.4.4

[68] Li Ma, Rafael Perini, Webb McKnight, Michael Dicay, Andre Klein, Morley D Hollenberg, and John L Wallace. Proteinase-activated receptors 1 and 4 counter-regulate endostatin and VEGF release from human platelets. *Proceedings of the National Academy of Sciences of the United States of America*, 102(1):216–220, January 2005. 2.5

[69] T E Maione, G S Gray, A J Hunt, and R J Sharpe. Inhibition of tumor growth in mice by an analogue of platelet factor 4 that lacks affinity for heparin and retains potent angiostatic activity. *Cancer Research*, 51(8):2077–2083, April 1991. 2.4.4

[70] Véronique Masson, Laetitia Devy, Christine Grignet-Debrus, Sarah Bernt, Khalid Bajou, Silvia Blacher, Guy Roland, Yawen Chang, Timothy Fong, Peter Carmeliet, Jean-Michel Foidart, and Agnès Noël. Mouse aortic ring assay: A new approach of the molecular genetics of angiogenesis. *Biological Procedures Online*, 4(1):24–31, June 2002. 1.2.1

[71] RMH Merks, SA Newman, and JA Glazier. Cell-oriented modeling of In Vitro capillary development. In *Cellular Automata, Proceedings*, pages 425–434. Indiana Univ, Dept Phys, Biocomplex Inst, Bloomington, IN 47405 USA, 2004. 1.3

[72] Joseph Michaels, Michael Dobryansky, Robert D Galiano, Kirit A Bhatt, Russell Ashinoff, Daniel J Ceradini, and Geoffrey C Gurtner. Topical vascular endothelial growth factor reverses delayed wound healing secondary to angiogenesis inhibitor administration. *Wound Repair and Regeneration*, 13(5):506–512, September 2005. 2.2.1

[73] M Mitsi, K Forsten-Williams, M Gopalakrishnan, and M A Nugent. A Catalytic Role of Heparin within the Extracellular Matrix. *Journal of Biological Chemistry*, 283(50):34796–34807, October 2008. 2.4.4

[74] Maria Mitsi, Zhenning Hong, Catherine E Costello, and Matthew A Nugent. Heparin-Mediated Conformational Changes in Fibronectin Expose Vascular Endothelial Growth Factor Binding Sites . *Biochemistry*, 45(34):10319–10328, August 2006. 2.4.4

[75] Atsushi Miyawaki. Development of probes for cellular functions using fluorescent proteins and fluorescence resonance energy transfer. *Annual review of biochemistry*, 80:357–373, June 2011. 5.2.2

[76] N Mukai, T Akahori, M Komaki, and Q Li. ScienceDirect - Experimental Cell Research : A comparison of the tube forming potentials of early and late endothelial progenitor cells. *Experimental cell ...*, 2008. 1.2.1

[77] M NAKATSU and C HUGHES. Chapter 4 An Optimized ThreeDimensional In Vitro Model for the Analysis of Angiogenesis. *Methods in Enzymology*, 443:65–82, 2008. (document), 1-5

[78] Martin N Nakatsu, Richard C A Sainson, Jason N Aoto, Kevin L Taylor, Mark Aitkenhead, Sofía Pérez-del Pulgar, Philip M Carpenter, and Christopher C W Hughes. Angiogenic sprouting and capillary lumen formation modeled by human umbilical vein endothelial cells (HUVEC) in fibrin gels: the role of fibroblasts and Angiopoietin-1. *Microvascular research*, 66(2):102–112, September 2003. (document), 1.2.1, 1-5

[79] V Nehls and D Drenckhahn. A novel, microcarrier-based in vitro assay for rapid and reliable quantification of three-dimensional cell migration and angiogenesis. *Microvascular research*, 50(3):311–322, November 1995. 1.2.1

[80] R F Nicosia and A Ottinetti. Growth of microvessels in serum-free matrix culture of rat aorta. A quantitative assay of angiogenesis in vitro. *Laboratory investigation; a journal of technical methods and pathology*, 63(1):115–122, July 1990. 1.2.1

[81] James R Norris. *Markov chains*. Cambridge Univ Pr, July 1998. 4.3.3

[82] Mingxing Ouyang, Jie Sun, Shu Chien, and Yingxiao Wang. Determination of hierarchical relationship of Src and Rac at subcellular locations with FRET biosensors. *Proceedings of the National Academy of Sciences*, 105(38):14353–14358, September 2008. 5.2.2

[83] Shayn M Peirce. Computational and Mathematical Modeling of Angiogenesis. *Microcirculation*, 15(8):739–751, January 2008. 1, 1.3

[84] Luis L oacute pez Maury, Samuel Marguerat, and J uuml rg B auml hler. Tuning gene expression to changing environments: from rapid responses to evolutionary adaptation. *Nature Reviews Genetics*, 9(8):583–593, August 2008. 3.2.1

[85] Michael Potente, Holger Gerhardt, and Peter Carmeliet. Basic and Therapeutic Aspects of Angiogenesis. *Cell*, 146(6):873–887, September 2011. 1

[86] S Ramanathan and J R Broach. Do cells think? *Cellular and molecular life sciences*, 64(14):1801–1804, May 2007. 3.2.1

[87] G Rätsch, S Mika, and B Schölkopf. Constructing boosting algorithms from SVMs: an application to one-class classification. *IEEE Transactions on ...*, 2002. 4.3.2, 4.5.4

[88] JJ Rissanen. Fisher information and stochastic complexity. *Information Theory*, 1996. 2

[89] P Romagnani, F Annunziato, L Lasagni, E Lazzeri, C Beltrame, M Francalanci, M Uguccioni, G Galli, L Cosmi, L Maurenzig, M Baggiolini, E Maggi, S Romagnani, and M Serio. Cell cycle-dependent expression of CXC chemokine receptor 3 by endothelial cells mediates angiostatic activity. *The Journal of clinical investigation*, 107(1):53–63, January 2001. 2.5

[90] Anne Saaristo, Tuomas Tammela, Anniina Fārkkilā, Marika Kärkkäinen, Erkki Suominen, Seppo Yla-Herttuala, and Kari Alitalo. Vascular Endothelial Growth Factor-C Accelerates Diabetic Wound Healing. *The American Journal of Pathology*, 169(3):1080–1087, September 2006. 2.2.1

[91] R Salcedo, J H Resau, D Halverson, E A Hudson, M Dambach, D Powell, K Wasserman, and J J Oppenheim. Differential expression and responsiveness of chemokine receptors (CXCR1-3) by human microvascular endothelial cells and umbilical vein endothelial cells. *The FASEB journal : official publication of the Federation of American Societies for Experimental Biology*, 14(13):2055–2064, October 2000. 2.5

[92] Suphansa Sawamiphak, Mathias Ritter, and Amparo Acker-Palmer. Preparation of retinal explant cultures to study ex vivo tip endothelial cell responses. *Nature Protocols*, 5(10):1659–1665, September 2010. 1.2.1

[93] RE Schapire. Improved boosting algorithms using confidence-rated predictions. *Machine learning*, 1999. 4.3.2, 4.5.4

[94] A Shamloo. Matrix density mediates polarization and lumen formation of endothelial sprouts in VEGF gradients. *Lab on a Chip*, 2010. 1.2.1

[95] Yoojin Shin, Jessie S Jeon, Sewoon Han, Gi-Seok Jung, Sehyun Shin, Sang-Hoon Lee, Ryo Sudo, Roger D Kamm, and Seok Chung. In vitro 3D collective sprouting angiogenesis under orchestrated ANG-1 and VEGF gradients. *Lab on a Chip*, 11(13):2175–2181, 2011. 1.2.1

[96] Jonathan W Song, Stephen P Cavnar, Ann C Walker, Kathryn E Luker, Mudit Gupta, Yi-Chung Tung, Gary D Luker, and Shuichi Takayama. Microfluidic endothelium for studying the intravascular adhesion of metastatic breast cancer cells. *PLoS ONE*, 4(6):e5756, 2009. 1.2.1

[97] Sabrina L Spencer, Suzanne Gaudet, John G Albeck, John M Burke, and Peter K Sorger. Non-genetic origins of cell-to-cell variability in TRAIL-induced apoptosis. *Nature*, 459(7245):428–432, April 2009. 4.4

[98] C L Stokes, D A Lauffenburger, and S K Williams. Migration of individual microvessel endothelial cells: stochastic model and parameter measurement. *Journal of Cell Science*, 99 (Pt 2):419–430, June 1991. 1.3

[99] CL STOKES and DA LAUFFENBURGER. Analysis of the Roles of Microvessel Endothelial-Cell Random Motility and Chemotaxis in Angiogenesis. *Journal of Theoretical Biology*, 152(3):377–403, 1991. 1.3

[100] Geraldine A Strasser, Joshua S Kaminker, and Marc Tessier-Lavigne. Microarray analysis of retinal endothelial tip cells identifies CXCR4 as a mediator of tip cell morphology and branching. *Blood*, 115(24):5102–5110, June 2010. 5.2.4

[101] S Struyf. Platelets Release CXCL4L1, a Nonallelic Variant of the Chemokine Platelet Factor-4/CXCL4 and Potent Inhibitor of Angiogenesis. *Circulation Research*, 95(9):855–857, October 2004. 4.3.4

[102] S Suchting, C Freitas, and F Le Noble. The Notch ligand Delta-like 4 negatively regulates endothelial tip cell formation and vessel branching. In *Proceedings of the ...*, 2007. 5.2.4

[103] R Sudo, S Chung, I K Zervantonakis, V Vickerman, Y Toshimitsu, L G Griffith, and R D Kamm. Transport-mediated angiogenesis in 3D epithelial coculture. *The FASEB Journal*, 23(7):2155–2164, June 2009. 1.2.1

[104] Eric Sulpice, Jean-Olivier Contreres, Julie Lacour, Marijke Bryckaert, and Gerard Tobelem. Platelet factor 4 disrupts the intracellular signalling cascade induced by vascular endothelial growth factor by both KDR dependent and independent mechanisms. *European Journal of Biochemistry*, 271(16):3310–3318, July 2004. 4.3.4

[105] R Swaminathan, C P Hoang, and A S Verkman. Photobleaching recovery and anisotropy decay of green fluorescent protein GFP-S65T in solution and cells: cytoplasmic viscosity probed by green fluorescent protein translational and rotational diffusion. *Biophysical Journal*, 72(4):1900–1907, April 1997. 1.3

[106] Toshihide Tanaka, Yoshinobu Manome, Patrick Wen, Donald W Kufe, and Howard A Fine. Viral vector-mediated transduction of a modified platelet factor 4 cDNA inhibits angiogenesis and tumor growth. *Nature Medicine*, 3(4):437–442, April 1997. 2.4.4

[107] Marcia G Tonnesen, Xiaodong Feng, and Richard A F Clark. Angiogenesis in Wound Healing. *Journal of Investigative Dermatology Symposium Proceedings*, 5(1):40–46, December 2000. 2.1

[108] J Vandercappellen, S Liekens, A Bronckaers, S Noppen, I Ronsse, C Dillen, M Belleri, S Mitola, P Proost, M Presta, S Struyf, and J Van Damme. The COOH-Terminal Peptide of Platelet Factor-4 Variant (CXCL4L1/PF-4var47-70) Strongly Inhibits Angiogenesis and Suppresses B16 Melanoma Growth In vivo. *Molecular Cancer Research*, 8(3):322–334, March 2010. 4.3.4

[109] Jo Vandercappellen, Jo Van Damme, and Sofie Struyf. The role of the CXC chemokines platelet factor-4 (CXCL4/PF-4) and its variant (CXCL4L1/PF-4var) in inflammation, angiogenesis and cancer. *Cytokine and Growth Factor Reviews*, 22(1):1–18, February 2011. (document), 2.2.2, 2-1, 2.4.1

[110] LA Vese. A multiphase level set framework for image segmentation using the Mumford and Shah model. *International Journal of Computer Vision*, 2002. 4.3.1, 4.5.2

[111] L Wood, R Kamm, and H Asada. Stochastic modeling and identification of emergent behaviors of an Endothelial Cell population in angiogenic pattern formation. *The International Journal of Robotics Research*, 30(6):659–677, May 2011. 1.3, 4.2, 4.4.1

[112] Nahoko Yamamura, Ryo Sudo, Mariko Ikeda, and Kazuo Tanishita. Effects of the Mechanical Properties of Collagen Gel on the In VitroFormation of Microvessel Networks by Endothelial Cells. *Tissue Engineering*, 13(7):1443–1453, July 2007. (document), 1-4, 4.3.1

[113] Q Yan, R B Vernon, A E Hendrickson, and E H Sage. Primary culture and characterization of microvascular endothelial cells from Macaca monkey retina. *Investigative ophthalmology & visual science*, 37(11):2185–2194, October 1996. 4.4

[114] Sharon Yunger, Liat Rosenfeld, Yuval Garini, and Yaron Shav-Tal. Single-allele analysis of transcription kinetics in living mammalian cells. *Nature Methods*, 7(8):631–633, August 2010. 1.3

[115] Ioannis K Zervantonakis, Chandrasekhar R. Kothapalli, Seok Chung, Ryo Sudo, and Roger D Kamm. Microfluidic devices for studying heterotypic cell-cell interactions and tissue specimen cultures under controlled microenvironments. *Biomicrofluidics*, 5(1):–, 2011. 1.2.1

[116] W H Zhu, X Guo, S Villaschi, and R Francesco Nicosia. Regulation of vascular growth and regression by matrix metalloproteinases in the rat aorta model of angiogenesis. *Laboratory investigation; a journal of technical methods and pathology*, 80(4):545–555, April 2000. 1.2.1